Coherent Coulomb Excitation of Relativistic Nuclei in Aligned Crystal Targets[1]

V. R. Zoller

Institute of Theoretical and Experimental Physics, ul. Bol'shaya Cheremushkinskaya 25, Moscow 117218 Russia
e-mail: zoller@heron.itep.ru
Received January 3, 2002

We study coherent Coulomb excitation of ultrarelativistic nuclei passing through an aligned crystal target. We develop multiple-scattering description of this process, which consistently incorporates both the specific resonant properties of particle–crystal interactions and the shadowing effect typical of the diffractive scattering. We emphasize that the effect of quantum mechanical diffraction makes the physics of ultrarelativistic nuclear excitations cardinally different from the physics of nonrelativistic atomic excitations experimentally studied so far. It is found that, at small transverse momenta $q_\perp$, the shadowing effect drastically changes the dependence of coherent amplitudes on crystal thickness L from the widely discussed growth $\propto L$, typical of the Born approximation, to the inverse-thickness attenuation law. At relatively large $q_\perp$, no attenuation effect is found, but the coherency condition is shown to pose stringent constraint on the increase in the transition rate with growing L. © 2002 MAIK "Nauka/Interperiodica".

PACS numbers: 25.75.-q; 61.18.Bn

1. There were several proposals for experiments on coherent Coulomb excitation of relativistic nuclei in a crystal target [1–4]

$$A\gamma \longrightarrow A^*. \tag{1}$$

The central idea of [1–4] is that in a nucleus (ground state $|0\rangle$ and excited state $|1\rangle$) under periodic perturbation $V \sin \nu t$, with the frequency ν equal to the level splitting $\Delta E = E_1 - E_0$, quantum beats are developed with the oscillation frequency $\omega = \langle 1|V|0\rangle$. If the perturbation V is weak, then, for $\omega t \ll 1$, the $|0\rangle \longrightarrow |1\rangle$-transition probability $P(t)$ increases rapidly with time, $P(t) \propto \omega^2 t^2$. If one could subject nuclei to a high-frequency field, $\nu \simeq \Delta E$, the rates of transition would be enhanced substantially. A high monochromaticity is an evident condition for sustaining a fast increase in $P(t)$ over a large time scale. It was suggested in [1–4] that all of the above requirements are best met in a Coulomb interaction of a high-energy nucleus propagating in a crystal along the crystallographic axis. Here, the role of "time" is played by the crystal thickness L. For ultrarelativistic particles, ν is enhanced due to the Doppler shift $\nu' = \gamma\nu$, where γ is the Lorentz factor. It is the Lorentz factor which can boost ν to the range of hundreds of keV.

In [1–4], the Coulomb field of a crystal was calculated in the Weizsäker–Williams approximation and then applied to the calculation of the transition amplitude in the plane-wave Born approximation. It was claimed in [1, 2, 4] that the law $P(N) \propto N^2$ holds up to crystal thicknesses $N = L/a \sim 10^4 – 10^5$ (a stands for the

lattice spacing). However, in a consistent treatment of coherent $A \longrightarrow A^*$ transitions, one must include distortions due to Coulomb interactions in the initial state of nucleus A and Coulomb interactions in the final state of excited nucleus A^*.

In this paper, we show that, at small transverse momenta, the effect of these interactions (multiple diffractive scattering by atomic row) is reminiscent of the well-known Glauber–Gribov shadowing effect [5, 6] and entails attenuation of the coherent excitation amplitudes with increasing crystal thickness. The early discussion of shadowing in the total cross section of elastic high-energy particle–crystal scattering can be found in [7].

Here we emphasize that it is the diffraction phenomenon which makes the physics of ultrarelativistic nuclear excitations with $\gamma \sim 10$ basically different from the physics of coherent atomic excitation [8, 9], where typically $\gamma \ll 1$.

It should be noted, however, that in contrast to the high-energy hadronic scattering, which is described by the predominantly imaginary amplitudes, the shadowing in Coulomb scattering does not imply a simple "absorption," but implies a redistribution of scattered nuclear waves in the phase space. Therefore, the depletion of the domain of small $q_\perp$ means the enhancement of the large-$q_\perp$ region. At relatively large transverse momenta, no shadowing occurs, but the nuclear waves scattered by different atoms get out of tune easily. Here the structure factor of a crystal poses stringent constraint on the coherent excitation rate, which, at the pro-

---

[1] This article was submitted by the author in English.

jectile energies available, would not exhibit any sizable enhancement effect.

2. Consider small-angle Coulomb scattering of an ultrarelativistic nucleus (mass number A, charge Z_1, and four-momentum p) moving along the crystal axis. The projectile nucleus undergoes a correlated series of soft collisions, which give rise to diagonal ($A \longrightarrow A$, $A^* \longrightarrow A^*$) and off-diagonal ($A \longrightarrow A^*$, $A^* \longrightarrow A$) transitions. The interatomic distances, $a \sim 3$–5 Å, are large compared to the Thomas–Fermi screening radius $r \simeq 0.468 Z_2^{-1/2}$ Å, where Z_2 is the atomic number of the target atom and $\alpha = 1/137$. The amplitude $\langle u^2 \rangle^{1/2}$ of thermal vibrations of the lattice, as estimated from the Debye approximation, is $\langle u^2 \rangle^{1/2} \sim (0.05$–$0.1)$ Å for most of the commonly studied crystals at room temperature [10]. The relevant impact parameters, b, satisfy, as we will see, condition $b \ll a$. This implies that the amplitudes of scattering by different atomic strings parallel to a given crystallographic axis are incoherent.

In [3, 1, 2], the study of the electric dipole transition from the ground state $|J^\pi = 1/2^-\rangle$ of ^{19}F to its excited state $|1/2^+\rangle$ was proposed. Let us accept this proposal and consider the phenomenological matrix element for the transition $1/2^+ \longrightarrow 1/2^-$

$$\mathcal{M} = d\bar{u}(p')\gamma_5\sigma_{\mu\nu}u(p)q^\nu\varepsilon^\mu, \tag{2}$$

where both $u(p')$ and $u(p)$ are bispinors of initial and final states of the projectile nucleus. By definition, $\sigma_{\mu\nu} = \frac{1}{2}[\gamma_\mu, \gamma_\nu]$, d is the transition dipole moment, $p' = p + q$, $\mathbf{q} = (\mathbf{q}_\perp, \kappa)$, $\mathbf{q}_\perp = (q_\perp\cos\phi, q_\perp\sin\phi)$, and ε is the photon polarization vector. Then, after a series of standard high-energy approximations, one readily finds the helicity-flip Born amplitude $t_B(\mathbf{q}_\perp)$ of the transition $1/2^+ \longrightarrow 1/2^-$ in the nucleus–atom collision

$$t_B(\mathbf{q}_\perp) = \sqrt{\alpha}dZ_2\frac{q_\perp e^{i\phi}}{q_\perp^2 + \lambda^2}, \tag{3}$$

where $\lambda^2 = \mu^2 + \kappa^2$ and $\mu = r^{-1}$. Here κ is denoted by the longitudinal momentum transfer

$$\kappa = (2M\Delta E + q_\perp^2)/2p, \tag{4}$$

which determines the coherency length $l_c \sim \kappa^{-1}$. In Eq. (4), M is the mass of projectile-nucleus. The excitation energy is $\Delta E \simeq 110$ keV. Amplitudes are normalized such that

$$d\sigma/dq_\perp^2 = |t(\mathbf{q}_\perp)|^2. \tag{5}$$

The integral $\sigma_B = \int d\mathbf{q}_\perp^2 |t_B(\mathbf{q}_\perp)|^2$ diverges at large $q_\perp$ and must be regularized. The inverse amplitude of lattice thermal vibrations is the natural regulator.

The use of the impact parameter representation simplifies the summation of multiple Coulomb scattering diagrams. Then, in the eikonal approximation, the full nucleus–atom amplitude to all orders in $\alpha Z_1 Z_2$ reads

$$t(\mathbf{q}_\perp) = \sqrt{\alpha}dZ_2\lambda e^{i\phi}$$
$$\times \int b\,db\,J_1(q_\perp b)K_1(\lambda b)\exp[i\chi(b)], \tag{6}$$

where $J_1(x)$ and $K_{0,1}(x)$ are the Bessel functions, and the screened Coulomb phase-shift function is

$$\chi(b) = -\beta K_0(\mu b), \tag{7}$$

where $\beta = 2\alpha Z_1 Z_2$.

The only phenomenological parameter in Eq. (2) is the dipole moment of the $1/2^+ \longrightarrow 1/2^-$ transition, denoted by d; it can be determined from the width Γ of the 110-keV $^{19}F(1/2^-)$ level, which is $\Gamma = d^2\Delta E^3/\pi + \mathbb{O}(\Delta E/M)$. Then the measured lifetime $\tau = \Gamma^{-1} = (0.853 \pm 0.010) \times 10^{-9}$ s [11] yields $d \simeq 4.3 \times 10^{-8}$ keV^{-1}. Two important conclusions can be drawn immediately. First, because of a large value of τ, the decay of an excited state inside the target can safely be neglected. Second, due to the smallness of d, the excitation amplitude is much smaller than the elastic Coulomb amplitude for all $q_\perp$ up to $q_\perp \sim \sqrt{\alpha}Z_1/d$ and can be considered as a perturbation. Thus, the multichannel problem reduces to the one-channel problem.

Now, in the static lattice approximation, the evaluation of the total transition amplitude for a string of N identical atoms reads [12]

$$T(\mathbf{q}_\perp) = \sqrt{\alpha}dZ_2\lambda S(q_\perp)e^{i\phi}I(q_\perp), \tag{8}$$

where

$$I(q_\perp) = \int b\,db\,J_1(q_\perp b)K_1(\lambda b)\exp[-i\beta N K_0(\mu b)]. \tag{9}$$

In Eq. (8), $S(q_\perp)$ is the structure factor of the lattice

$$S(q_\perp) = \frac{\sin(\kappa Na/2)}{\sin(\kappa a/2)}, \tag{10}$$

and κ is given by Eq. (4).

Let us split integration over b in Eq. (9) into two domains: $\mu^{-1} \lesssim b \lesssim a$ and $0 < b < \mu^{-1}$. In the former domain, it would suffice to use the asymptotic form $K_{0,1}(x) \sim \exp(-x)$, which, upon a slight readjustment of screening parameters $\mu \longrightarrow \mu' = \mu\left(1 + \frac{1}{2}\log(2\xi/\pi)\right)$ and $\lambda \longrightarrow \lambda' = \mu\left(1 + \frac{1}{2}\log(2\xi/\pi)\right)$ with a relevant $b \sim \mu^{-1}\xi$, proves to be numerically very accurate. Hereafter, $\xi = \log(\beta N/\Delta)$ and $\Delta = \lambda/\mu = \sqrt{1 + \kappa^2/\mu^2}$. Then, the steepest descent from the saddle-point at

$$b_0 = \mu^{-1}(\xi + i\pi/2)$$

yields for $\xi^2 \ll \mu/\lambda$ and $q_\perp \lesssim \mu\xi^{-1}$

$$I(q_\perp) \simeq \frac{q_\perp}{\mu^3}\sqrt{\frac{2\pi}{\Delta}}e^{-\Delta}$$

$$\times \log^2\left(\frac{i\beta N}{\Delta}\right)\left(\frac{\Delta}{i\beta N}\right)^\Delta \propto \log^2 N\left(\frac{1}{N}\right)^\Delta. \quad (11)$$

Consequently, for small transverse momenta $q_\perp \gg \mu\xi^{-1}$, as soon as $\xi \gg 1$, which holds for all practical purposes, one has the attenuation of the coherent excitation amplitude.

For higher transverse momenta $q_\perp \gg \mu\xi^{-1}$, the use of the stationary phase approximation, with the above reservation about the substitution $\mu \longrightarrow \mu'$ and $\lambda \longrightarrow \lambda'$, yields

$$I(q_\perp) \simeq \frac{\sqrt{\eta}}{\mu q_\perp}\exp(-\Delta\eta)$$

$$\times \exp\left[-i\frac{q_\perp}{\mu}(\eta+1)\right] \propto \sqrt{\log N}\left(\frac{1}{N}\right)^\Delta, \quad (12)$$

where $\eta = \log(\mu\beta N/q_\perp) \gg 1$. As before, we find no enhancement but obtain the attenuation of the coherent transition amplitude. Indeed, let the projectile momentum satisfy the resonance condition [1–4]

$$M\Delta E/p = 2\pi n/a, \quad n = 0, 1, 2, \dots \quad (13)$$

In [1, 2, 4], a search for the coherent transitions in the W crystal was suggested for $n = 3$. This regime corresponds to $\gamma \simeq 10$ and $\Delta = \lambda/\mu \simeq \sqrt{1 + 4\pi^2 n^2/(a\mu)^2} \simeq 1.2$. A still higher n discussed in [1–4] would correspond to higher momentum transfers and to much stronger suppression of the coherent excitation amplitude.

Let us now consider the contribution to $I(q_\perp)$ from the second domain, $0 < b < \mu^{-1} \equiv r$. The region of small impact parameters is affected by the lattice thermal vibrations, which are known to suppress the coherent amplitude. Let us make use of the fact that for some commonly used crystals at room temperature the root-mean-square one-dimensional displacement u is such that $u \ll r$. For example, for the diamond lattice suggested as a target in [3] $u/r \simeq 0.16$ [10]. The integral on the right-hand side of Eq. (9) reads

$$I(q_\perp) = \int_0^r b\,db\,J_1(q_\perp b)K_1(\lambda b)$$

$$\times \exp[-i\beta N K_0(\mu b)] \simeq \frac{1}{\lambda q_\perp}\left(\frac{\mu}{q_\perp}\right)^{i\beta N}\int_0^{rq_\perp} dz\,J_1(z)z^{i\beta N}. \quad (14)$$

The contribution to $I(q_\perp)$, nonvanishing with increasing N, comes from $z \sim z_0 = \beta N$, where z_0 is the point of stationary phase. Hence, the requirement is $q_\perp \gg \mu\beta N$.

The width $\delta z \simeq \sqrt{\beta N}$ of the region, from which the major contribution comes to Eq. (14), is much smaller than the interval of integration in Eq. (14), which is $\Delta z \gg \beta N$. Then, for $\beta N \gg 1$ one has

$$I(q_\perp) \simeq \frac{1}{\lambda q_\perp}\exp\left[-i\beta N\log\frac{q_\perp}{2\mu} + 2i\varphi\right], \quad (15)$$

where

$$\exp[2i\varphi] = \frac{\Gamma(1 + i\beta N/2)}{\Gamma(1 - i\beta N/2)}. \quad (16)$$

Thus, for $q_\perp \gg \mu\beta N$ one finds no attenuation effect. However, at large $q_\perp$ the structure factor of crystal (10) enters the game. The resonance condition (13) implies fine tuning of phases of scattered waves. If $q_\perp$ becomes large, the phases get out of tune easily. At large projectile momentum p, the structure factor (10) allows variation of $q_\perp^2$ within a rather wide range which is, however, $\propto N^{-1}$. In the neighborhood of the resonance,

$$S(q_\perp) \simeq N[1 - B^2 q_\perp^4], \quad (17)$$

where $B = aN/4\sqrt{6}\,p$. Hence, the excitation cross section is $\sigma = \int dq_\perp^2 |T(\mathbf{q}_\perp)|^2$, which varies as

$$\sigma \propto N^2\log(N_c/N), \quad (18)$$

where

$$N_c \ll N_n = \left[\frac{4\sqrt{6}\,p_n}{a\mu^2\beta^2}\right]^{1/3} \quad (19)$$

and $p_n = aM\Delta E/2\pi n$. For example, for the W crystal, $N_3 \simeq 30$ and for the diamond target crystal one has $N_3 \simeq 300$. With certain reservations about the effect of lattice thermal vibrations, one can conclude that not only the $q_\perp$ dependence of the coherent transition amplitude differs dramatically from the early predictions [2, 3] but the effect of coherent enhancement is much weaker than that predicted in [1, 2, 4].

Note, that for $N \ll N_n$ one has

$$p/q_\perp^2 \gg L \quad (20)$$

and the straight-path approximation, which we rely upon in our analysis, holds true.

We conclude that, in quantitative analysis of high-energy particle–crystal interactions, due allowance must be made for the multiple scattering effects which dramatically change the pattern of the coherent Coulomb excitation, compared to widely used approaches based on the Born approximation.

REFERENCES

1. V. V. Okorokov and S. V. Proshin, Preprint No. ITEP-13-1980 (Inst. of Theoretical and Experimental Physics, Moscow, 1980).

2. Yu. L. Pivovarov, A. A. Shirokov, and S. A. Vorobev, Nucl. Phys. A **509**, 800 (1990); Yu. L. Pivovarov and A. A. Shirokov, Yad. Fiz. **37**, 1101 (1983) [Sov. J. Nucl. Phys. **37**, 653 (1983)].

3. R. Fusina and J. C. Kimball, Nucl. Instrum. Methods Phys. Res. B **33**, 77 (1988).

4. V. V. Okorokov, Yu. L. Pivovarov, A. A. Shirokov, and S. A. Vorobev, Proposal of Experiment on Coherent Excitation of Relativistic Nuclei in Crystals, ITEP-90-49, Fermilab Library.

5. R. J. Glauber, in *Lectures in Theoretical Physics*, Ed. by W. E. Brittin *et al.* (Interscience, New York, 1959), Vol. 1, p. 315.

6. V. N. Gribov, Zh. Éksp. Teor. Fiz. **56**, 892 (1969) [Sov. Phys. JETP **29**, 483 (1969)]; Zh. Éksp. Teor. Fiz. **57**, 1306 (1969) [Sov. Phys. JETP **30**, 709 (1970)].

7. N. P. Kalashnikov, E. A. Koptelov, and M. I. Ryazanov, Zh. Éksp. Teor. Fiz. **63**, 1107 (1972) [Sov. Phys. JETP **36**, 583 (1972)]; N. P. Kalashnikov and V. D. Mur, Yad. Fiz. **16**, 1117 (1972) [Sov. J. Nucl. Phys. **16**, 613 (1973)].

8. V. V. Okorokov, Pis'ma Zh. Éksp. Teor. Fiz. **2**, 175 (1965) [JETP Lett. **2**, 111 (1965)]; Yad. Fiz. **2**, 1009 (1965) [Sov. J. Nucl. Phys. **2**, 719 (1966)].

9. V. V. Okorokov, D. L. Tolchenkov, Yu. P. Cheblukov, *et al.*, Pis'ma Zh. Éksp. Teor. Fiz. **16**, 588 (1972) [JETP Lett. **16**, 415 (1972)]; Phys. Lett. A **43A**, 485 (1973); M. J. Gaillard, J. C. Poizat, J. Remillieux, and M. L. Gaillard, Phys. Lett. A **45A**, 306 (1973); H. G. Berry, D. S. Gemmel, R. E. Holland, *et al.*, Phys. Lett. A **49A**, 123 (1974); M. Mannami, H. Kudo, M. Matsushita, and K. Ishii, Phys. Lett. A **64A**, 136 (1978); S. Datz, C. M. Moak, O. H. Crawford, *et al.*, Phys. Rev. Lett. **40**, 843 (1978); C. M. Moak, S. Datz, O. H. Crawford, *et al.*, Phys. Rev. A **19**, 977 (1979); F. Fujimoto, Nucl. Instrum. Methods Phys. Res. B **40/41**, 165 (1989); Y. Iwata, K. Komaki, Y. Yamazaki, *et al.*, Nucl. Instrum. Methods **48**, 163 (1990).

10. D. S. Gemmel, Rev. Mod. Phys. **46**, 129 (1974).

11. F. Ajzenberg-Selove, Nucl. Phys. A **190**, 1 (1972).

12. V. R. Zoller, Pis'ma Zh. Éksp. Teor. Fiz. **64**, 743 (1996) [JETP Lett. **64**, 788 (1996)].

Entanglement of Atomic States upon Collective Radiative Decay

A. M. Basharov

Moscow Engineering Physics Institute (Technical University), Kashirskoe sh. 31, Moscow, 115409 Russia
e-mail: bash@online.ru
Received November 28, 2001; in final form, December 25, 2001

It is shown in the Markovian approximation that the relaxation of two atoms noninteracting with each other in the field of a common thermostat results in the entanglement of atomic states. With time, this entanglement either vanishes or takes a stationary value depending on the initial conditions. © 2002 MAIK "Nauka/Interperiodica".

PACS numbers: 03.65.Ud

In recent years, the problems of quantum information, quantum teleportation, theory of measurements, etc. [1, 2] have stimulated interest in so-called entangled quantum states, for which the wave function (density matrix) of a system of particles noninteracting with each other cannot be represented as the product of their individual wave functions (density matrices). The well-known Bell's states are an example of completely entangled states of a system of two two-level particles. An example of entangled photon states is provided by so-called squeezed light [3], which is used in experiments on teleportation of photon states. The formation of entangled atomic states was considered in recent studies [4–8], and works devoted to the use of entangled atomic states in optical effects are now emerging in increasing number [9–11]. The inverse process of destruction of the entangled atomic states is a part of decoherence [12] and often attributed to relaxation processes. In this work, it is demonstrated that the relaxation processes can lead not only to the decoherence but also to an inverse process of entanglement of atomic states, even if the atoms do not interact with each other (in contrast to [4–6]). The presence of a common thermostat is one of the basic conditions for entangling atomic states in radiative decay. A simple example of radiative decay of two noninteracting two-level atoms in the field of a common thermostat at zero temperature is considered in this work. In contrast to the well-known Dicke model and other models of collective atomic decay [13, 14], this process was described using a new model based on the Lindblad equations. This model accounts for the dynamics of both symmetric and antisymmetric (in particles) atomic states. The general solution was obtained for the equations of the model. The Peres–Horodecki criterion [15, 16], which is stronger than the Bell's inequalities, was used as a criterion for entanglement of atomic states. The eigenvalues of the two-particle atomic density matrix transposed according to Peres–Horodecki were calculated and the domain of parameters, where the atomic states resulting from the decay of nonentangled initial atomic wave functions become entangled, was found. It is worthy of note that, so far, by the entanglement of states in radiative decay was meant the entanglement of an atomic state with a state of thermostat particles (see, e.g., recent work [17]).

Let us consider a two-atomic system consisting of identical (not necessarily) two-level atoms in a common electromagnetic field and decompose the electric-field operator into the longitudinal and transverse components. The longitudinal component is responsible for the dipole–dipole interaction. The transverse component of an electromagnetic field is treated as a thermostat field:

$$\left\langle \Phi_0 \middle| b_\omega^+ b_\omega \middle| \Phi_0 \right\rangle = N(\omega)\delta(\omega - \omega'),$$

$$\left\langle \Phi_0 \middle| b_\omega b_\omega^+ \middle| \Phi_0 \right\rangle = (1 + N(\omega))\delta(\omega - \omega'),$$

$$\left\langle \Phi_0 \middle| b_\omega \middle| \Phi_0 \right\rangle = \left\langle \Phi_0 \middle| b_\omega^+ \middle| \Phi_0 \right\rangle = 0,$$

where b_ω^+ and b_ω are the photon creation and annihilation operators, $N(\omega)$ is the photon density at a frequency ω, and $|\Phi_0\rangle$ is the initial thermostat state. Under the assumption that the interaction with atoms has a Markovian character, the transverse electromagnetic field is described by the Wiener quantum process [18, 19]. Writing Ito's standard quantum stochastic equation, one obtains the following equation for the two-atomic density matrix $\mathcal{R}$ (two-particle operators are denoted by calligraphic letters):

$$\frac{d\mathcal{R}}{dt} = \frac{i}{\hbar}[\mathcal{R}, \mathcal{H}_{sys}] - \widehat{\Gamma}\mathcal{R}, \tag{1}$$

where

$$\mathcal{H}_{sys} = \frac{\hbar\omega_0}{2}(C_3 \otimes \widehat{1} + \widehat{1} \otimes C_3) + \mathcal{V}_{d-d}$$

is the Hamiltonian of the two-atomic system in the absence of other external fields and interactions. Here, ω_0 is the atomic transition frequency; $C_3 = |1\rangle\langle1| - |0\rangle\langle0|$; vectors $|0\rangle$ and $|1\rangle$ correspond to the lower and upper atomic states, respectively; $\mathcal{V}_{d-d}$ is the operator of dipole–dipole interaction between atoms; and $\widehat{\Gamma}\mathcal{R}$ is the relaxation operator. Since our goal is to clarify the role of a thermostat in the entanglement of atomic states, we will consider a model situation and ignore the dipole–dipole interaction. The thermostat is assumed to be at zero temperature and free of photons; i.e., $N(\omega) = 0$. In this case, $\mathcal{V}_{d-d} = 0$ and

$$\widehat{\Gamma}\mathcal{R} = \frac{\chi|d_{10}|^2}{2}(\mathcal{R}\mathcal{C}_+\mathcal{C}_- + \mathcal{C}_+\mathcal{C}_-\mathcal{R} - 2\mathcal{C}_-\mathcal{R}\mathcal{C}_+), \quad (2)$$

where d_{10} is the matrix element of atomic dipole moment, χ is the atom–thermostat coupling constant, and

$$\mathcal{C}_\pm = C_\pm \otimes \widehat{1} + e^{\mp i\theta}\widehat{1} \otimes C_\pm. \quad (3)$$

Here, $C_- = |0\rangle\langle1|$ and $C_+ = |1\rangle\langle0|$ are the annihilation and creation operators for the excited state of a two-level atom. In conjunction with the operator C_3, they provide the realization of the SU(2) algebra: $[C_+, C_-] = C_3$, $[C_3, C_\pm] = \pm2C_\pm$. The factor $e^{i\theta}$ accounts for the possible phase difference appearing in the electric field of the thermostat because of the different spatial position of atoms.

Note that form (2) of the relaxation operator is valid for all kinetic equations describing relaxation in the Markovian approximation, as was proved by Lindblad [20] under very general assumptions on the thermostat properties and the character of evolution of a dynamic system.

Let us introduce the following notation: $\mathcal{R}_{el} = \langle e|\mathcal{R}|l\rangle$, $|g\rangle = |0\rangle \otimes |0\rangle$, $|f\rangle = |1\rangle \otimes |0\rangle$, $|l\rangle = |0\rangle \otimes |1\rangle$, and $|e\rangle = |1\rangle \otimes |1\rangle$, where $|f\rangle$ is the state of the two-particle system, in which the first atom is excited and the second is in the ground state, and so on. In the matrix notation $\mathcal{R}_{ij}$, the subscript i spans the values 1, 2, 3, 4 or g, f, l, e. The one-particle density matrix of, e.g., the first atom, $\rho^{(f)}$, is determined as $\rho^f = Sp_l\mathcal{R}$, $\rho_{11}^f = \mathcal{R}_{ee} + \mathcal{R}_{ff}$, $\rho_{00}^f = \mathcal{R}_{ll} + \mathcal{R}_{gg}$, and $\rho_{10}^f = \mathcal{R}_{el} + \mathcal{R}_{fg}$.

It is evident that the nonzero matrix elements of the operator $\mathcal{C}_\pm$ are

$$\langle f|\mathcal{C}_+|g\rangle = \langle g|\mathcal{C}_-|f\rangle = 1,$$

$$\langle l|\mathcal{C}_+|g\rangle = \langle g|\mathcal{C}_-|l\rangle^* = e^{-i\theta},$$

$$\langle e|\mathcal{C}_+|f\rangle = \langle f|\mathcal{C}_-|e\rangle^* = e^{-i\theta},$$

$$\langle e|\mathcal{C}_+|l\rangle = \langle l|\mathcal{C}_-|e\rangle = 1.$$

Therefore, in the matrix form,

$$\mathcal{C}_+ = \begin{pmatrix} 0 & 0 & 0 & 0 \\ 1 & 0 & 0 & 0 \\ e^{-i\theta} & 0 & 0 & 0 \\ 0 & e^{-i\theta} & 1 & 0 \end{pmatrix},$$

$$\mathcal{C}_- = \begin{pmatrix} 0 & 1 & e^{i\theta} & 0 \\ 0 & 0 & 0 & e^{i\theta} \\ 0 & 0 & 0 & 1 \\ 0 & 0 & 0 & 0 \end{pmatrix}.$$

To find the stationary solution to Eqs. (1)–(3) note that the matrix elements of the operators between the entangled two-particle state $|a\rangle = \frac{1}{\sqrt{2}}(|f\rangle - e^{-i\theta}|l\rangle)$ and the state $|g\rangle$ or $|e\rangle$ are zero: $\langle e|\mathcal{C}_+|a\rangle = \langle g|\mathcal{C}_-|a\rangle = 0$. The vectors $|a\rangle$ and $|s\rangle = \frac{1}{\sqrt{2}}(|f\rangle + e^{-i\theta}|l\rangle)$, together with $|g\rangle$ and $|e\rangle$, form a new orthonormalized basis set for the states of the two-atomic system. In this basis, Eqs. (1) and (2) take the simplest form

$$\frac{d\mathcal{R}_{gg}}{d\tau} = 2\mathcal{R}_{ss}, \quad \frac{d\mathcal{R}_{ee}}{d\tau} = -2\mathcal{R}_{ee},$$

$$\frac{d\mathcal{R}_{ss}}{d\tau} = 2\mathcal{R}_{ee} - 2\mathcal{R}_{ss},$$

$$\frac{d\mathcal{R}_{aa}}{d\tau} = \frac{d\tilde{\mathcal{R}}_{ag}}{d\tau} = 0, \quad \frac{d\tilde{\mathcal{R}}_{ae}}{d\tau} = -\tilde{\mathcal{R}}_{ae}, \quad (4)$$

$$\frac{d\mathcal{R}_{sa}}{d\tau} = -\mathcal{R}_{sa}, \quad \frac{d\tilde{\mathcal{R}}_{sg}}{d\tau} = 2e^{i\theta}\tilde{\mathcal{R}}_{es} - \tilde{\mathcal{R}}_{sg},$$

$$\frac{d\tilde{\mathcal{R}}_{se}}{d\tau} = -2\tilde{\mathcal{R}}_{se}, \quad \frac{d\tilde{\mathcal{R}}_{eg}}{d\tau} = -\tilde{\mathcal{R}}_{eg},$$

where $\tau = \chi|d_{10}|^2 t$ is the dimensionless time and tilde denotes the slow [compared to $\exp(\pm i\omega_0 t)$] part of the density matrix, e.g., $\mathcal{R}_{sg} = \tilde{\mathcal{R}}_{sg}\exp(-i\omega_0 t)$, $\mathcal{R}_{eg} = \tilde{\mathcal{R}}_{eg}\exp(-2i\omega_0 t)$, and so on.

The general solution to Eqs. (4) has the form

$$\mathcal{R}_{ss} = (2\mathcal{R}_{ee}^{(0)}\tau + \mathcal{R}_{ss}^{(0)})e^{-2\tau}, \quad \mathcal{R}_{ee} = \mathcal{R}_{ee}^{(0)}e^{-2\tau},$$

$$\mathcal{R}_{aa} = \mathcal{R}_{aa}^{(0)},$$

$$\mathcal{R}_{gg} = 1 - \mathcal{R}_{aa}^{(0)} - \{\mathcal{R}_{ss}^{(0)} + \mathcal{R}_{ee}^{(0)}(1 + 2\tau)\}e^{-2\tau},$$

$$\tilde{\mathcal{R}}_{ag} = \tilde{\mathcal{R}}_{ag}^{(0)}, \quad \tilde{\mathcal{R}}_{ae} = \tilde{\mathcal{R}}_{ae}^{(0)}e^{-\tau}, \quad \mathcal{R}_{sa} = \mathcal{R}_{sa}^{(0)}e^{-\tau}, \tag{5}$$

$$\tilde{\mathcal{R}}_{se} = \tilde{\mathcal{R}}_{se}^{(0)}e^{-2\tau}, \quad \tilde{\mathcal{R}}_{eg} = \tilde{\mathcal{R}}_{eg}^{(0)}e^{-\tau},$$

$$\mathcal{R}_{sg} = \mathcal{R}_{sg}^{(0)}e^{-\tau} + 2e^{i\theta}\tilde{\mathcal{R}}_{es}^{(0)}(e^{-\tau} - e^{-2\tau}),$$

where the superscript (0) denotes the initial value of the density matrix. There is the obvious relationship

$$\mathcal{R}_{ff} = \frac{1}{2}\{\mathcal{R}_{ss} + \mathcal{R}_{aa} + \mathcal{R}_{as} + \mathcal{R}_{sa}\},$$

$$\mathcal{R}_{ll} = \frac{1}{2}\{\mathcal{R}_{ss} + \mathcal{R}_{aa} - \mathcal{R}_{as} - \mathcal{R}_{sa}\},$$

$$\tilde{\mathcal{R}}_{el} = \frac{1}{\sqrt{2}}e^{i\theta}\{\tilde{\mathcal{R}}_{es} - \tilde{\mathcal{R}}_{ea}\},$$

$$\tilde{\mathcal{R}}_{ef} = \frac{1}{\sqrt{2}}\{\tilde{\mathcal{R}}_{ea} + \tilde{\mathcal{R}}_{es}\}, \tag{6}$$

$$\tilde{\mathcal{R}}_{gl} = \frac{1}{\sqrt{2}}e^{i\theta}\{\tilde{\mathcal{R}}_{gs} - \tilde{\mathcal{R}}_{ga}\}, \quad \tilde{\mathcal{R}}_{gf} = \frac{1}{\sqrt{2}}\{\tilde{\mathcal{R}}_{ga} + \tilde{\mathcal{R}}_{gs}\},$$

$$\mathcal{R}_{fl} = \frac{1}{2}e^{i\theta}\{\tilde{\mathcal{R}}_{as} + \mathcal{R}_{ss} - \mathcal{R}_{aa} - \mathcal{R}_{sa}\}.$$

Expressions (5) and (6) give the general solution for the problem of radiative decay of two quiescent and noninteracting identical atoms situated in a common thermostat, whose effect on the atoms is described in the Markovian approximation. Let us consider the stationary solution to Eqs. (1) and (2). The nonzero elements of the two-particle density matrix have the form

$$\mathcal{R}_{gg}^{st} = 1 - \mathcal{R}_{aa}^{(0)}, \quad \mathcal{R}_{ff}^{(0)} = \mathcal{R}_{ll}^{st} = \frac{1}{2}\mathcal{R}_{aa}^{(0)},$$

$$\tilde{\mathcal{R}}_{gl}^{st} = -\frac{1}{\sqrt{2}}e^{i\theta}\tilde{\mathcal{R}}_{ga}^{(0)}, \quad \tilde{\mathcal{R}}_{gf}^{st} = \frac{1}{\sqrt{2}}\tilde{\mathcal{R}}_{ga}^{(0)}, \tag{7}$$

$$\mathcal{R}_{fl}^{st} = -\frac{1}{2}e^{i\theta}\mathcal{R}_{aa}^{(0)}.$$

To determine whether the stationary solution (7) is entangled, we will use the Peres–Horodecki criterion [15, 16]; the latter is as follows. Consider a two-particle density matrix transposed with respect to the indices of one of the atoms, e.g., of the second atom. This matrix will be referred to as the Peres–Horodecki matrix. The necessary condition for the density matrix to be factorable is that all its eigenvalues are positive. For the entangled states, at least one eigenvalue of this matrix is negative. For example, the negative eigenvalue is $-1/2$ for the entangled states $|s\rangle$ and $|a\rangle$. The negative eigenvalue of the Peres–Horodecki matrix can be treated as a characteristic of the entangled state. The

stationary Peres–Horodecki matrix has the form

$$\mathcal{R}^{P-Hst}$$

$$= \begin{pmatrix} 1 - \mathcal{R}_{aa}^{(0)} & \frac{1}{\sqrt{2}}\tilde{\mathcal{R}}_{ga}^{(0)} & -\frac{1}{\sqrt{2}}e^{-i\theta}\tilde{\mathcal{R}}_{ga}^{(0)*} & -\frac{1}{2}e^{-i\theta}\mathcal{R}_{aa}^{(0)} \\ \frac{1}{\sqrt{2}}\tilde{\mathcal{R}}_{ga}^{(0)*} & \frac{1}{2}\mathcal{R}_{aa}^{(0)} & 0 & 0 \\ -\frac{1}{\sqrt{2}}e^{i\theta}\tilde{\mathcal{R}}_{ga}^{(0)} & 0 & \frac{1}{2}\mathcal{R}_{aa}^{(0)} & 0 \\ -\frac{1}{2}e^{i\theta}\mathcal{R}_{aa}^{(0)} & 0 & 0 & 0 \end{pmatrix}.$$

Its eigenvalues are determined from the equations

$$\lambda_1 = \frac{1}{2}\mathcal{R}_{aa}^{(0)},$$

$$4\lambda\left\{\left(\lambda - \frac{1}{2}\mathcal{R}_{aa}^{(0)}\right)(1 - \mathcal{R}_{aa}^{(0)} - \lambda) + |\tilde{\mathcal{R}}_{ga}^{(0)}|^2\right\} \tag{8}$$

$$+ \left(\lambda - \frac{1}{2}\mathcal{R}_{aa}^{(0)}\right)\mathcal{R}_{aa}^{(0)2} = 0.$$

An analysis of Eq. (8) indicates that there are domains of parameters where one of the eigenvalues of the Peres–Horodecki matrix is negative. This is most evident in the case where each atom at zero time is in a pure state and characterized by its own wave function $|\psi^f\rangle$ or $|\psi^l\rangle$. In this case, the minimum eigenvalue of the Peres–Horodecki matrix is $\lambda_{min} = -0.17$ for $|\psi^{f,\,l}\rangle \sim |0\rangle \pm c|1\rangle$.

The radiative decay of two atoms in a common thermostat also gives rise to atomic correlations in the absence of entanglement. The decay of the excited atomic state $|1\rangle$ is an example. For a one-atomic system, one deals with the usual radiative decay:

$$\rho_{10}^f = 0, \quad \rho_{11}^f = e^{-\tau}, \quad \rho_{00}^f = 1 - e^{-\tau}. \tag{9}$$

The collective decay of two excited atoms is described by the expressions

$$\mathcal{R}_{ss} = 2\tau e^{-2\tau}, \quad \mathcal{R}_{ee} = e^{-2\tau},$$

$$\mathcal{R}_{gg} = 1 - (1 + 2\tau)e^{-2\tau}, \tag{10}$$

$$\mathcal{R}_{ag} = \mathcal{R}_{aa} = \mathcal{R}_{ae} = \mathcal{R}_{sa} = \mathcal{R}_{se} = \mathcal{R}_{eg} = \mathcal{R}_{sg} = 0,$$

or, in the $g, f, l,$ and e variables,

$$\mathcal{R}_{ff} = \mathcal{R}_{ll} = \tau e^{-2\tau}, \quad \mathcal{R}_{fl} = e^{i\theta}\tau e^{-2\tau},$$

$$\mathcal{R}_{ef} = \mathcal{R}_{el} = \mathcal{R}_{gl} = \mathcal{R}_{gf} = 0.$$

Here, the initial condition is that both atoms are in the excited state (only the matrix element $\mathcal{R}_{ee}^{(0)} = 1$ is non-

zero). In this case, the one-particle density matrix of each atom evolves as

$$\rho_{11}^f = e^{-2\tau}(1+\tau), \quad \rho_{00}^f = 1-(1+\tau)e^{-2\tau},$$
$$\rho_{10}^f = 0. \tag{11}$$

According to the Peres–Horodecki criterion, state (10) is not entangled, even though the equation for the one-particle density matrix is not closed and is governed by the dynamics of the two-particle density matrix:

$$\widehat{\Gamma}\rho_{11}^f = \rho_{11}^f + \frac{1}{2}(\mathscr{R}_{fl}e^{-i\theta} + \mathscr{R}_{lf}e^{i\theta}),$$

$$\widehat{\Gamma}\rho_{00}^f = -\rho_{11}^f - (e^{-i\theta}\mathscr{R}_{fl} + e^{i\theta}\mathscr{R}_{lf}),$$

$$\widehat{\Gamma}\rho_{10}^f = \rho_{10}^f - \frac{1}{2}e^{i\theta}(\mathscr{R}_{ef} - \mathscr{R}_{lg}).$$

The above examples indicate that the role of a common thermostat in the entanglement of atomic states reduces to ensuring different dynamics for the atomic states differing in the types of permutation symmetry. The interaction of atoms with the common thermostat is determined by operators (3), which are characterized by certain types of permutation symmetry. At the same time, among the two-atomic states, at least two types ($|s\rangle$ and $|a\rangle$), differing in behavior with respect to atomic permutations, are involved in the relaxational dynamics in different ways. In the simplest case, the states of one of the types ($|a\rangle$) evolve unitarily, whereas the dynamics of the second type ($|s\rangle$) is not unitary. As a result, the representation of the nonentangled initial state in terms of the entangled basis vectors $|s\rangle$ and $|a\rangle$ is disbalanced. For this reason, atomic states become entangled after a time. Different dynamics can be manifested not only in the unitary or nonunitary evolution of the entangled basis atomic states but also in the different rates of their relaxation in the common nonunitary evolution. The decay of two atoms initially occupying the upper excited level does not result in the entanglement of atomic states, because the initial states are characterized only by one type of permutation symmetry.

Finally, if one-atomic dynamics serves as a quantum channel, then the above conclusion about the entanglement of atomic states agrees with recent results demonstrating an increase in the information capacity of quantum communication channels exposed to correlated noises [21].

REFERENCES

1. S. Ya. Kilin, Usp. Fiz. Nauk **169**, 507 (1999).
2. I. V. Bargatin, B. A. Grishanin, and V. N. Zadkov, Usp. Fiz. Nauk **171**, 625 (2001).
3. D. F. Walls and G. J. Milburn, *Quantum Optics* (Springer-Verlag, Berlin, 1995).
4. G. K. Brennen *et al.*, Phys. Rev. Lett. **82**, 1060 (1999).
5. A. Beige *et al.*, J. Mod. Opt. **47**, 401 (2000).
6. I. V. Bargatin, B. A. Grishanin, and V. N. Zadkov, Fortschr. Phys. **48**, 637 (2000).
7. L. M. Duan, J. I. Cirac, P. Zoller, and E. S. Polzik, Phys. Rev. Lett. **85**, 5643 (2000).
8. B. Julsgaard, A. Kozhekin, and E. S. Polzik, quant-ph/0106057 (2001).
9. C. P. Yang and G. C. Guo, Physica A (Amsterdam) **273**, 352 (1999).
10. G. C. Guo and C. P. Yang, Physica A (Amsterdam) **260**, 173 (1998).
11. V. N. Gorbachev, A. I. Zhiliba, and A. I. Trubilko, Izv. Akad. Nauk, Ser. Fiz. **66**, 345 (2002).
12. M. B. Menskiĭ, *Quantum Measurings and Decoherention. Models and Phenomenology* (Fizmatlit, Moscow, 2001).
13. A. V. Andreev, V. I. Emel'yanov, and Yu. A. Il'inskiĭ, *Cooperative Phenomena in Optics* (Nauka, Moscow, 1988).
14. M. G. Benedict, A. M. Ermolaev, V. A. Malyshev, *et al.*, *Superradiance: Multiatomic Coherent Emission* (Inst. of Physics Publ., Bristol, 1996).
15. A. Peres, Phys. Rev. Lett. **77**, 1413 (1996).
16. M. Horodecki, P. Horodecki, and R. Horodecki, Phys. Lett. A **223**, 1 (1996).
17. S. Bose, I. Fuentes-Guridi, P. L. Knight, and V. Vedral, quant-ph/0103063 (2001).
18. C. W. Gardiner, *Quantum Noise* (Springer-Verlag, Berlin, 1991), Chap. 5.
19. A. I. Maimistov and A. M. Basharov, *Nonlinear Optical Waves* (Kluwer, Dordrecht, 1999), Appendix 1.
20. G. Lindblad, Commun. Math. Phys. **48**, 119 (1976).
21. C. Macchiavello and G. M. Palma, quant-ph/0107052 (2001).

Transformation of the Orbital Angular Momentum of a Beam with Optical Vortex in an Astigmatic Optical System

A. Ya. Bekshaev*, M. V. Vasnetsov**, V. G. Denisenko**, and M. S. Soskin**

* Odessa State University, Odessa, 65026 Ukraine
** Institute of Physics, National Academy of Sciences of Ukraine, Kiev, 03039 Ukraine

Double sign inversion of the topological charge of an optical vortex was predicted and observed experimentally for a beam focused by a cylindrical lens. Beam evolution after passing through the lens is analyzed by the decomposition of the orbital angular momentum into the "vortical" and "mechanical" components. Topological reactions in the beam wave resulting in the sign inversion of the optical vortex upon the intersection of the wave-front edge dislocation are considered. © *2002 MAIK "Nauka/Interperiodica".*

PACS numbers: 41.85.-p

Light beams with optical vortices (OVs) are of interest because of their unusual properties and possible applications to the manipulation of microobjects [1]. The OV structure is determined by the phase circulation about the vortex axis, on which the phase is indefinite while the amplitude vanishes. The presence of the orbital angular momentum (OAM) is a fundamental property of a beam with OV [2, 3]. For an axially symmetric beam with a "longitudinal" OV [e.g., Laguerre–Gaussian (LG) mode of laser cavity], the OAM is caused by the helical shape of the wave front, and the OAM is uniquely determined by the OV topological charge. For the broken OV symmetry (e.g., after passing through an astigmatic optical system), the OV structure can change noticeably, although the beam OAM in the free space is conserved. The vortex can even change its sign in the topological intersection reaction of the OV axis and the wave-front edge dislocation [4, 5] (this principle underlies the operation of LG-mode π converter [2, 3]). At present, there is no commonly accepted approach to the description of these "variable" OVs. The concepts of "noncanonical strength" of OV [5] or "anisotropic dislocation" [6], although helpful in certain cases, characterize only local features of the geometric structure of a beam and are not directly related to its physical parameters. It is the purpose of this work to analyze the transformations of the orbital angular momentum of an OV beam in an astigmatic system by introducing the concept of "vortex" OAM and to observe experimentally the predicted effects.

In the general case, OAM of a light beam also contains the irrotational ("mechanical") component arising due to the misalignment of the symmetry axes of the transverse distributions of intensity and phase (e.g., a rotating Gaussian beam is a vortex-free beam with OAM [7]). The indicated components are fundamentally different, because the mechanical OAM can change upon passing through the corresponding phase corrector, whereas the vortical OAM cannot.

As an illustration, we restrict ourselves only to the simplest case of focusing a circular LG mode LG_0^1 by a cylindrical lens. In this case, the distribution of the electric-field complex amplitude at the lens entry has the form

$$
\begin{aligned}
u(x, y) &= \frac{2}{b^2}\sqrt{\frac{2\Phi}{c}}(x + iy)\exp\left(-\frac{x^2 + y^2}{2b^2}\right) \\
&= \frac{2}{b^2}\sqrt{\frac{2\Phi}{c}}\rho\exp\left(-\frac{\rho^2}{2b^2} + i\varphi\right),
\end{aligned}
\tag{1}
$$

where x and y are the Cartesian coordinates in the cross-sectional plane, ρ and φ are the corresponding polar coordinates, Φ is the total energy flux in the beam, c is the speed of light, and b is the parameter of the beam cross-sectional size. It is convenient to analyze beam evolution by using the properties of the matrix of second moments [7, 8]

$$
\begin{aligned}
\mathbf{M} &= \begin{pmatrix} \mathbf{M}_{11} & \mathbf{M}_{12} \\ \tilde{\mathbf{M}}_{12} & \mathbf{M}_{22} \end{pmatrix} \\
&= \frac{c}{8\pi\Phi}\int\begin{pmatrix}\mathbf{r}\\\mathbf{p}\end{pmatrix}(\tilde{\mathbf{r}}\tilde{\mathbf{p}})I(\mathbf{r}, \mathbf{p}, z)\,dx\,dy\,dp_x\,dp_y,
\end{aligned}
\tag{2}
$$

where $I(\mathbf{r}, \mathbf{p}, z)$ is the Wigner function of the light beam [8, 9], $\mathbf{r} = \begin{pmatrix} x \\ y \end{pmatrix}$ is the transverse radius vector ($|\mathbf{r}| = \rho$),

$\mathbf{p} = \begin{pmatrix} p_x \\ p_y \end{pmatrix}$, and ~ means transposition (the matrix of moments $\mathbf{Q} = 2k\mathbf{M}$ equivalent to Eq. (2) was used in [8]). As was shown in [7], the OAM per unit beam length is determined as

$$\Lambda = -\frac{\Phi}{c^2}\mathrm{tr}(\mathbf{M}_{12}\mathbf{J}), \qquad (3)$$

where $\mathbf{M}_{12}$ is the right upper block of the matrix of moments (2) and $\mathbf{J} = \begin{pmatrix} 0 & 1 \\ -1 & 0 \end{pmatrix}$. In particular, matrix (2) for initial beam (1) has the form

$$\begin{pmatrix} \mathbf{M}_{11} & \mathbf{M}_{12} \\ \tilde{\mathbf{M}}_{12} & \mathbf{M}_{22} \end{pmatrix} = \begin{pmatrix} b^2\mathbf{I} & \dfrac{1}{2k}\mathbf{J} \\ -\dfrac{1}{2k}\mathbf{J} & \dfrac{1}{k^2 b^2}\mathbf{I} \end{pmatrix}, \qquad (4)$$

where $\mathbf{I}$ is the 2×2 unit matrix and k is the radiation wave number. It follows from Eq. (3) that $\Lambda = \Phi/c^2 k$ in accordance with the known results presented in [1].

Using Eq. (4) and formulas describing the transformation of the matrix of moments in an arbitrary optical system [8], we find that, after passing through the astigmatic lens with focal lengths f_y, $f_x = \infty$ and the free interval of length z, the blocks of the matrix of beam moments take the form

$$\mathbf{M}_{11}(z) = \frac{b^2}{2\eta^2}\begin{pmatrix} 2\eta^2(1+\sigma^2) & \sigma^2\eta \\ \sigma^2\eta & 2(\sigma-\eta)^2 + 2\sigma^2\eta^2 \end{pmatrix}, \quad (5)$$
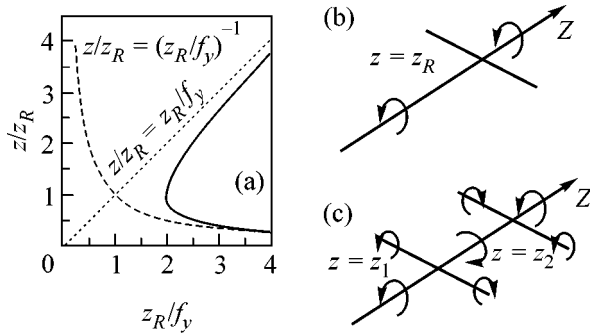

Fig. 1. (a) The solid line corresponds to the zeros of Λ_v (vortical OAM component) vs. the z_R/f_y ratio. Asymptotes are shown by the dashed lines. (b) The diagram of the topological intersection reaction between the longitudinal OV and the edge dislocation for the degenerate case; the vortex does not change its sign. (c) The same for the double inversion; the vortex changes its sign upon each intersection. The arrows indicate the direction of the circulation of the Poynting vector about the vortex axis.

$$\mathbf{M}_{12}(z) = \frac{1}{2k\eta^2}\begin{pmatrix} 2\sigma\eta^2 & \eta(\sigma+\eta) \\ \eta(\sigma-\eta) & 2(\sigma-\eta)+2\sigma\eta^2 \end{pmatrix}, \quad (6)$$

where $\sigma = z/z_R$, $\eta = f_y/z_R$, $z_R = kb^2$ is the Rayleigh length of the initial beam.

It is seen from Eqs. (6) and (3) that the total OAM of the beam retains its input value. To separate its vortical component, let us consider the possibility of the OAM transformation by a "smooth" phase corrector. The matrix $\mathbf{M}_{12}$ changes under this transformation as

$$\mathbf{M}_{12}^{\mathrm{out}} = \mathbf{M}_{12} - \mathbf{M}_{11}\Omega, \qquad (7)$$

where Ω is the matrix of wave-front astigmatic correction [8]. The fact that the correction matrix is always symmetric imposes restrictions on the possible changes in OAM. In particular, it follows from Eq. (7) that $\mathrm{tr}(\mathbf{M}_{12}^{\mathrm{out}}\mathbf{J}) = \mathrm{tr}(\mathbf{M}_{12}\mathbf{J})$ for beam (1) with matrix of moments (4); i.e., the vortical OAM of this beam is conserved. To separate the vortical OAM for an arbitrary beam, the OAM should be subjected to the transformation of type (7), under which the entire mechanical OAM is "subtracted"; i.e., the beam wave front should be made as plane as possible. With this aim, it is necessary to compensate the effective wave-front curvature $\mathbf{K}$ (see [8]), and the correction matrix should have the form

$$\Omega = \mathbf{K} = \mathbf{M}_{11}^{-1}\left[\mathbf{M}_{12} + \mathbf{J}\frac{\mathrm{tr}(\mathbf{M}_{12}\mathbf{M}_{11}\mathbf{J})}{\mathrm{Sp}\mathbf{M}_{11}}\right]. \qquad (8)$$

In this case, the matrix $\mathbf{M}_{12}^{\mathrm{out}}$ becomes antisymmetric and, according to Eqs. (7) and (3), the beam OAM proves to be equal to

$$\Lambda_v = -\frac{2\Phi}{c^2}\frac{\mathrm{tr}(\mathbf{M}_{12}\mathbf{M}_{11}\mathbf{J})}{\mathrm{Sp}\mathbf{M}_{11}}. \qquad (9)$$

The quantity (9) is conserved under transformations of type (7); i.e., it cannot be changed by the quadratic phase correlation. Moreover, it coincides with the total OAM (3) for the axially symmetric vortex [e.g., for the LG mode with matrix of moments (4)]. For this reason, one can treat Eq. (9) as a definition of the vortical OAM component of an axially symmetric beam with OV. For the beam formed via focusing of the LG_0^1 mode by a cylindrical lens, the substitution of the running values of matrices (5) and (6) in Eq. (9) allows one to describe the evolution of the vortical OAM component in the space behind the lens:

$$\Lambda_v(z) = \frac{\Phi}{kc^2}\frac{1-(\sigma/\eta)+\sigma^2}{1-(\sigma/\eta)+\sigma^2+(\sigma^2/2\eta^2)}. \qquad (10)$$

This formula gives the quantitative characteristic of the beam vortical OAM. In particular, zero Λ_v corresponds

to the absence of OV, and a change in the Λ_v sign means the inversion of the vortex sign. It is seen from Eq. (10) that this occurs at $\sigma = (1 \pm \sqrt{1 - 4\eta^2})/2\eta$, i.e., at those points on the Z axis where

$$z = \frac{z_R}{2f_y}(z_R \pm \sqrt{z_R^2 - 4f_y^2}). \qquad (11)$$

At $f_y < z_R/2$, there are two such inversion points, whereas at $f_y > z_R/2$ no such point exist (Fig. 1a). The critical relation $f_y = z_R/2$ between the lens focal length and the Rayleigh length of the initial beam separates these regions. If this relation is fulfilled, the quantity Λ_v turns to zero only once at a distance $z_0 = z_R$ (Fig. 1b).

In the transverse beam structure, a node line of zero amplitude arises in the inversion planes determined by Eq. (11). This signifies that the vortex inversion results from the topological intersection reaction of an axial OV and the wave-front edge dislocation representing a "transverse" OV [10] (see Fig. 1c). If the lens power is not too high, edge dislocations in the beam do not arise and OV does not change its sign. In any case, the sign of the axial OV in the far zone coincides with the sign of the initial OV, as corroborated by calculating the Fourier transform of the beam.

Each intersection leads to the inversion of both axial and transverse OV. The dislocation topology uniquely determines the signs of vortex charges (diagram in Fig. 1c). It should be emphasized that a change in the vortical OAM component is compensated by the mechanical component, whose value may become higher than the initial OAM of the beam upon the inversion of the vortex sign.

In the experiments, a beam with an axial OV was formed through the diffraction of a Gaussian beam from an He–Ne laser by a specially synthesized diffraction grating [11] giving an LG_0^1 mode in the first diffraction order. The beam was focused by a spherical lens onto the plane of a cylindrical lens. The beam diameter in the waist was 0.8 mm, which corresponds to $z_R = 80$ cm. The focal length of the cylindrical lens was 33 cm. The lens axis was directed vertically. Figure 2 shows the intensity distributions and beam interferograms for various distances. The OV position is identified through the splitting of an interference band [1]. Immediately behind the lens, the sign of the axial OV is the same as in the initial beam, although it becomes anisotropic (Figs. 2b, 2c). The first inversion is observed behind the lens focal plane (Figs. 2d, 2e). The splitting of the interference fringe in the interferogram is directed oppositely. The clockwise rotation of the pattern as a whole reflects the contribution from the mechanical OAM component. The second inversion of the vortex charge sign was detected at a distance of 155 cm (Figs. 2f, 2g). Thereafter, the intensity distribution shows no considerable changes and the sign of the OV is retained.
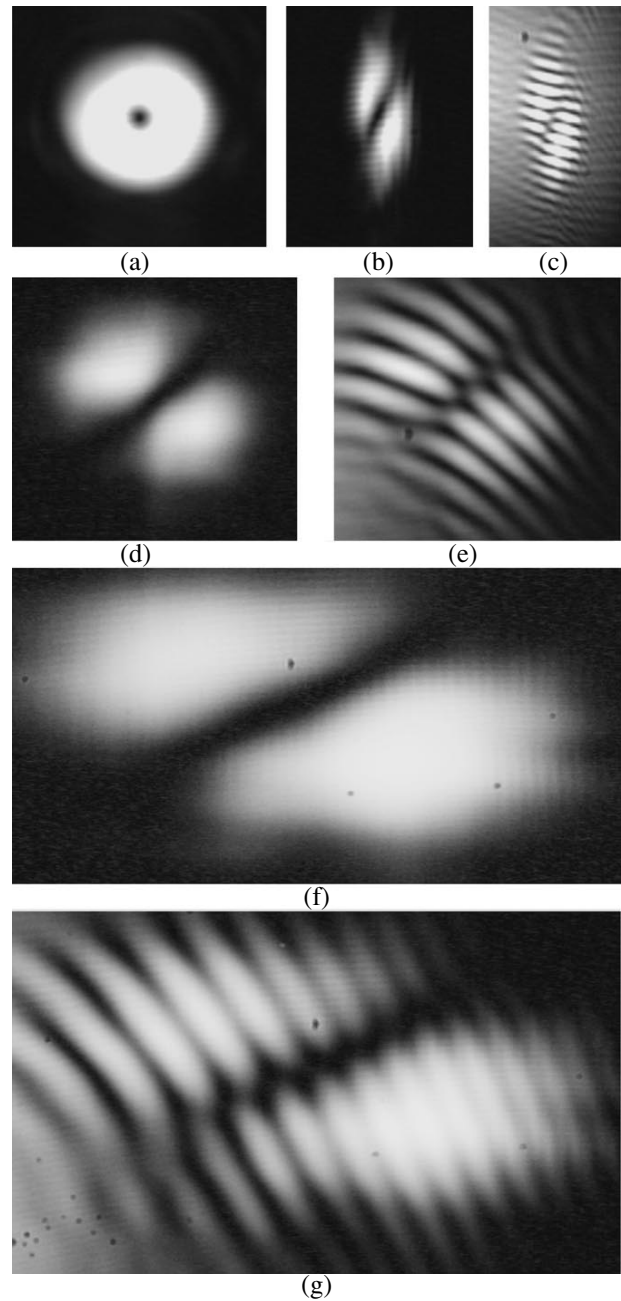
Fig. 2. Intensity distributions and interferograms of the beam with an axial OV. (a) Initial beam. (b, c) Beam at a distance of 29 cm behind the lens; the beam interferogram indicates the presence of an anisotropic OV. (d, e) A distance of 67 cm from the lens; the vortex sign is inverted. (f, g) A distance of 155 cm; the second sign inversion occurred.

The positions of inversion planes ($z_1 \approx 40$ cm and $z_2 \approx 144$ cm) are close to their calculated values (42 and 155 cm, respectively). Note that, although it is difficult to accurately determine the positions of inversion planes in the real experiment, it was distinctly demonstrated that the vortex doubly inverts its sign and that the conditions for its observation depend on the cross-

sectional size of the initial beam and on the lens focal length. Thus, the concept of decomposition of the beam OAM into the vortical and mechanical components has found its corroboration. The suggested approach can be used for analyzing more complex situations, e.g., diffraction of beams with OVs [12].

In conclusion, note that the single OV sign inversion is also possible in the general case of astigmatic lens. The necessary conditions for this to occur are different signs of f_x and f_y and the relation

$$|f_x f_y| < z_R^2. \tag{12}$$

We are grateful to I.V. Basistyǐ for assistance in synthesizing the diffraction grating and to V.A. Pas'ko for calculations.

REFERENCES

1. *Horizons in World Physics*, Vol. 228: *Optical Vortices*, Ed. by M. Vasnetsov and K. Staliunas (Nova Science, Huntington, 1999).
2. M. W. Beijersbergen, L. Allen, H. E. L. O. van der Veen, and J. P. Woerdman, Opt. Commun. **96**, 123 (1993).
3. L. Allen, M. J. Padgett, and M. Babiker, Prog. Opt. **39**, 291 (1999).
4. M. S. Soskin and M. V. Vasnetsov, Prog. Opt. **42**, 219 (2001).
5. G. Molina-Terriza, J. Recolons, J. P. Torres, and L. Torner, Phys. Rev. Lett. **87**, 023902 (2001).
6. I. Freund, N. Shvartsman, and V. Freilikher, Opt. Commun. **101**, 247 (1993).
7. A. Ya. Bekshaev, Proc. SPIE **3904**, 131 (1999).
8. Yu. A. Anan'ev and A. Ya. Bekshaev, Opt. Spektrosk. **76**, 624 (1994) [Opt. Spectrosc. **76**, 558 (1994)].
9. M. J. Bastiaans, J. Opt. Soc. Am. **69**, 1710 (1979).
10. V. A. Pas'ko, M. S. Soskin, and M. V. Vasnetsov, Opt. Commun. **198**, 49 (2001).
11. V. Yu. Bazhenov, M. V. Vasnetsov, and M. S. Soskin, Pis'ma Zh. Éksp. Teor. Fiz. **52**, 1037 (1990) [JETP Lett. **52**, 429 (1990)].
12. M. V. Vasnetsov, I. G. Marienko, and M. S. Soskin, Pis'ma Zh. Éksp. Teor. Fiz. **71**, 192 (2000) [JETP Lett. **71**, 130 (2000)].

Translated by R. Tyapaev

Pulse Duration Control for Intense Molecular Beams

G. N. Makarov

Institute of Spectroscopy, Russian Academy of Sciences, Troitsk, Moscow region, 142190 Russia
e-mail: g.makarov@isan.troitsk.ru
Received December 19, 2001

The method of pulse duration control is proposed for intense molecular beams. The method is based on the shortening of a primary molecular-beam pulse through the formation of a pressure shock ahead of a solid surface through which the beam is passed. The method was used to obtain intense SF_6, H_2, He, SF_6/H_2 (1/10), and SF_6/He (1/10) molecular beams with a pulse duration of ≤ 10–15 μs and a spatial length of ≤ 1–2 cm. © 2002 MAIK "Nauka/Interperiodica".

PACS numbers: 34.90.+q; 79.20.Rf; 61.80.Lj

1. Intense [$\geq 10^{20}$ molecule/(sr s)] pulsed molecular beams are used in various fields of fundamental and applied investigations (chemical reactions with energy barriers, elastic and inelastic collisions, interactions of molecules with a surface, etc.) [1]. In recent years, they have also been widely used in laser spectroscopy and photochemistry [2, 3], including laser isotope separation [4, 5]. The most popular method of obtaining intense molecular beams consists in the use of a skimmer for their separation from the gas-dynamically cooled jets formed by pulsed nozzles [6]. Pulse intensity, duration, velocity, and spread of molecular velocities in a beam (degree of gas cooling) are the main characteristics of pulsed beams.

Several nozzle types are used for the formation of pulsed molecular beams [6]. Among them, (1) nozzles with solenoid control (the fuel injector of an automobile is among this type), (2) nozzles with piezoelectric control, and (3) nozzles of the current-loop type [6, 7] are most popular. Pulses with a duration from several hundreds of microseconds to several milliseconds are typical of the first type, and pulses with a duration from approximately 100 μs to 10 ms are typical of the second type. Nozzles of the current-loop type are ordinarily used to generate pulses with a duration from 50 to 200 μs. The designers of nozzles of this type have succeeded in obtaining molecular beams with the shortest presently attainable pulse duration of $\cong 7$ μs [8].

The formation of short pulses (≤ 20 μs) presents considerable difficulties in designing the nozzles themselves and encounters serious problems associated with the input of a high energy (≥ 20 J) for fast opening of the nozzle [6]. At the same time, short-length (short-duration) molecular beams are required in many experiments, especially in the experiments on excitation and dissociation of molecular beams by high-intensity laser pulses [9, 10]. In this work, a rather simple method of pulse duration control is proposed for intense molecu-

lar beams. This method can be used to form molecular beams with a duration of ≤ 10 μs.

2. In the method proposed, the pulse duration of a molecular beam is controlled by the pressure shock (shock wave) [11–13] formed upon the interaction of the primary molecular beam with a solid surface. The shock plays the role of a high-speed gas-dynamic gate. The essence of the method is illustrated in Fig. 1. In the experiments, an intense [$\geq 10^{20}$ molecule/(sr s)] wide-aperture (divergence $\omega \cong 0.05$ sr) pulsed molecular beam was incident on the surface of a solid plate (a thin $\cong 100$-μm metallic plate was used) with a hole in $\cong 2$–3 mm diameter in its center. An intense supersonic molecular beam interacted with the plate to form a pressure shock ahead of it [14, 15], with the characteristic shock sizes on the order of the mean free path of molecules [11, 12].
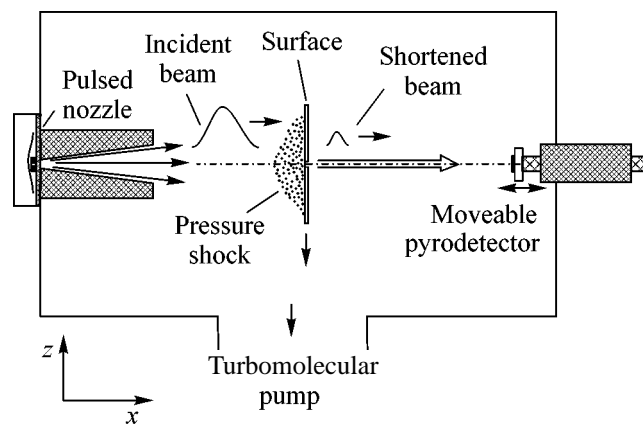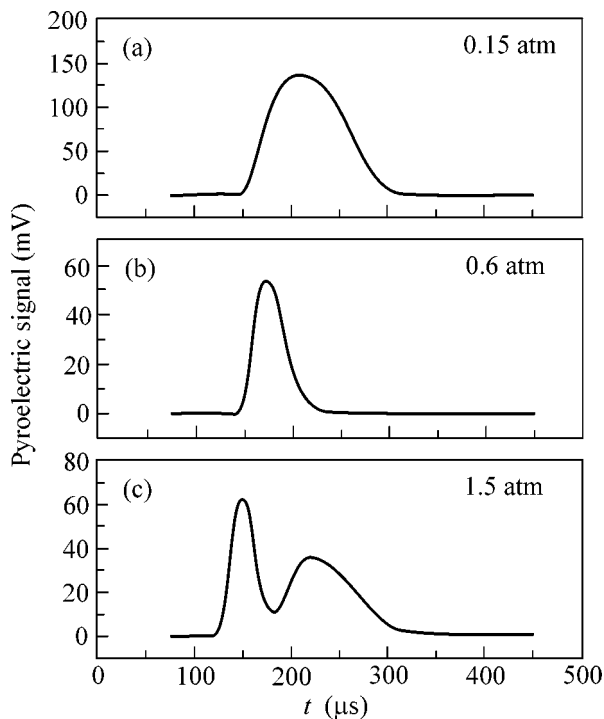

Fig. 1. Scheme of the experiment.

Fig. 2. Time evolution of a pulse of the ($SF_6/H_2 = 1/10$) molecular beam passing through a hole with a diameter of 2 mm in the plate for different gas pressures in the nozzle. The distance from the nozzle to the surface is 68 mm, and to the detector it is 143 mm. Gas pressure in the nozzle: (a) l0.15, (b) 0.6, and (c) 1.5 atm.

For low-intensity beams (with molecular concentration $N_1 \le 3 \times 10^{14}$ cm^{-3}), the pressure shock did not form ahead of the surface [16, 17]. In this case, the incident molecular beam propagating inside a solid angle defined by the hole area and the distance from the nozzle to the surface passed completely through the hole in the plate. The molecules reflected from the surface only slightly weakened the beam. As for the beam of rather high intensity [$I \ge 10^{20}$ molecule/(sr s), $N \ge 10^{15}$ cm^{-3}], only the leading low-intensity portion of the pulse passed through the hole in the plate, whereas the successively more intense portion of the beam was completely scattered ("absorbed") by the shock formed ahead of the surface. As a result, the pulse duration of the primary molecular beam shortened considerably. Note that there is a certain analogy with the shortening of the optical, e.g., laser pulse as a result of the onset of optical breakdown in the lens or telescope focus, when the trailing portion of the pulse is completely absorbed in the formed plasma.

A pulsed nozzle of the current-loop type was used in the experiments [7]. The nozzle outlet was 0.75 mm in diameter. The opening time was equal to $\cong$70–100 μs (FWHM), depending on the gas composition and pressure in the nozzle. The gas pressure in the nozzle was varied in the range from $\cong$0.1 to 7 atm. The nozzle cross section was shaped like a cone with a cone angle of 15°.

The cone length was 35 mm. The vacuum chamber where the molecular beam was formed was evacuated to a pressure of $\cong 1 \times 10^{-6}$ torr by a turbomolecular pump. The number of molecules flowing out of the nozzle during a pulse depended on the gas pressure in the nozzle and was varied in the experiments from $\cong 3 \times 10^{15}$ to $\cong 1.1 \times 10^{17}$ molecule/pulse. The method of measuring the number of molecules was described in detail in [16, 17].

We studied the duration and intensity of the shortened molecular beams as functions of the incident beam intensity and the hole diameter in the plate and measured the mean molecular velocity in the shortened beam and the spread of molecular velocities in it. Measurements were performed by the time-of-flight method based on the use of a pyrodetector (PD), with a time resolution of $\cong$3–5 μs, as a detector of the molecular beam [18, 19]. The molecular time-of-flight spectra were measured at different distances from the nozzle. They were used to determine the beam velocities and the spread of molecular velocities in the beams.

3. The experiments were carried out with the SF_6, H_2, He, SF_6/H_2 (1/10), and SF_6/He (1/10) molecular beams. In all cases, the primary beam pulse shortened appreciably (by 2–7 times). The time evolution of a beam pulse (molecular time-of- flight spectrum) passed through the hole in the plate is shown in Fig. 2 for different gas ($SF_6/He = 1/10$) pressures in the nozzle. The distance from the nozzle to the surface was 68 mm, and to the detector it was 143 mm. At a low gas pressure ($p \le 0.15$ atm), the incident beam intensity is low and the shock is not formed ahead of the surface [16, 17]; accordingly, the beam does not shorten upon passing through the hole in the plate (Fig. 2a). As the pressure is built up, the shock appears ahead of the surface and the incident pulse shortens (Fig. 2b). On further increase in the primary beam intensity (gas pressure in the nozzle), the pulse shortens even more (Fig. 2c), but this is accompanied by the generation of a rather intense secondary pulsed beam by the shock [20–22].

To suppress the formation of the secondary beam, the plate was turned through the angle $\alpha \cong 50°-65°$ about the incident beam. In this case, the shock ahead of the plate became oblique and the gas density in it was appreciably lower than in the normal shock [11, 13]. As a result, the intensity of the secondary beam became negligibly small compared to the intensity of the shortened primary beam. Note that, at large angles of incidence ($\alpha \ge 75°$), the shock ahead of the surface did not form [11–13] and the incident pulse did not shorten.

It was established experimentally that the higher the intensity of the incident molecular beam and the smaller the hole diameter, the shorter the beam. For the incident intensity $I \ge 10^{21}$ molecule/(sr s) ($N_1 \ge 10^{16}$ cm^{-3}), the duration of a pulse passed through the hole with a diameter of 2 mm was shorter than 10–15 μs.

The dependence of the pulse duration on the gas pressure in the nozzle is demonstrated in Fig. 3 for the H_2 beam. The angle of incidence on the plate was $\alpha \cong 65°$. The duration of the incident pulse was ~78 μs. One can see that the pulse does not shorten at pressures $p \le 0.15$ atm, and the duration of the passing pulse is $\le 10–12$ μs at a pressure of 4–5 atm.

The experimentally measured intensity, duration, and mean velocity of molecular beams, as well as the spread of molecular velocities in the beams obtained upon passing the SF_6/He (1/10) beam through the holes of different diameter, are given in the table. The overall gas pressure in the nozzle was 2.8 atm. The distance from the nozzle to the surface was 68 mm, and to the detector it was 143 mm. One can see that the pulse duration decreases appreciably with decreasing diameter of the hole through which the beam passes. Simultaneously, the mean beam velocity and the spread of molecular velocities in the beam increase. The increase in mean velocity is caused by fact that, as the pulse shortened, the successively higher-velocity portion of the primary beam passes through the hole, while the increase in velocity spread is due to the enhanced effect of beam scattering by the molecules reflected from the surface and hole walls. In the shortened beam, the velocity spread was 1.5–2 times greater than in the incident beam. Nevertheless, from the results given in the table it follows that the gas in the shortened beam was also quite cool (the Mach number was $M \cong v/\Delta v \cong 4–8$).

Note that the gas density in the shock depends on the index $\gamma = c_p/c_v$, i.e., on the ratio of specific heats. For a gas with a constant heat capacity, the maximum increase in the density of the normal shock is given by the relation [13] $\rho_2/\rho_1 = (\gamma + 1)/(\gamma - 1)$, where ρ_1 and ρ_2 are the gas densities in the incident beam and the shock, respectively. Because of this, a rather dense shock is formed ahead of the surface in the case of molecules with a small index γ [16, 17] (e.g., $\gamma \cong 1.1$ and $\rho_2/\rho_1 \cong 21$ for SF_6 [23]). Such a shock considerably shortens the primary pulse but simultaneously serves as the source of an intense secondary beam. As for the molecules with large index γ {e.g., He ($\gamma \cong 1.66$ [23]) and H_2
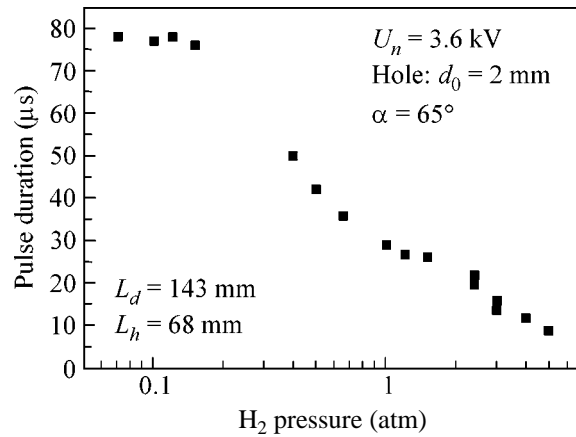

Fig. 3. Pulse duration of the H_2 beam passing thorough a hole of diameter 2 mm in the plate vs. gas pressure in the nozzle. The angle of incidence of the beam on the plate is $\alpha \approx 65°$. The distance from the nozzle to the plate $L_h = 68$ mm and to the detector $L_d = 143$ mm.

($\gamma \cong 1.4$ [23])}, the maximum increase in the density of the shock is appreciably smaller ($\rho_2/\rho_1 \cong 4$ and 6, respectively). In this case, the shock ahead of the surface has a moderate density. For this reason, the intensity of the secondary beam is appreciably lower than in the case of SF_6.

Thus, it has been shown in this work that the pulse duration can be controlled by virtue of the formation of a pressure shock ahead of the surface through which the molecular beam passes. A method is proposed and used to obtain molecular beams with a pulse duration of $\le 10–15$ μs and a spatial length of $\le 1–2$ cm. In the case of short-length pulses, one can excite (dissociate) almost all molecules in the beam by a high-intense laser pulse and, thereby, considerably enhance the efficiency of the laser action on the molecular beam [9, 10].

Experimental data on the shortening of the SF_6 /He (1/10) beam pulse

d_0, mm	Beam characteristics				
	beam duration, μs	intensity, rel. units	beam velocity v, m/s	spread of molecular velocities in the beam Δv, m/s	$v/\Delta v$
Unperturbed beam	78	100	980	105	9.3
4	68	60	1005	120	8.4
3	59	40	1040	150	6.8
2.5	51	22	1070	180	5.9
2	23	9	1095	240	4.6

REFERENCES

1. *Atomic and Molecular Beam Methods*, Ed. by G. Scoles (Oxford Univ. Press, New York, 1988).

2. V. N. Bagratashvili, S. I. Ionov, and G. N. Makarov, in *Laser Spectroscopy of Vibrationally Excited Molecules,* Ed. by V. S. Letokhov (Nauka, Moscow, 1990).

3. V. N. Bagratashvili, V. S. Letokhov, A. A. Makarov, and E. A. Ryabov, *Multiple Photon Infrared Laser Photophysics and Photochemistry* (Harwood Academic, New York, 1985).

4. G. N. Makarov, V. N. Lokhman, D. E. Malinovskiĭ, and D. D. Ogurok, Kvantovaya Élektron. (Moscow) **25**, 545 (1998).

5. V. M. Apatin, V. N. Lokhman, G. N. Makarov, *et al.*, Opt. Spektrosk. **91**, 910 (2001).

6. W. R. Gentry, in *Atomic and Molecular Beam Methods*, Ed. by G. Scoles (Oxford Univ. Press, New York, 1988).

7. W. R. Gentry and C. F. Giese, Rev. Sci. Instrum. **49**, 595 (1978).

8. W. R. Gentry, Comments At. Mol. Phys. **9**, 113 (1980).

9. G. N. Makarov, D. E. Malinovsky, and D. D. Ogurok, Laser Chem. **17**, 205 (1998).

10. G. N. Makarov, D. E. Malinovskiĭ, and D. D. Ogurok, Zh. Tekh. Fiz. **69** (1), 35 (1999) [Tech. Phys. **44**, 31 (1999)].

11. Ya. B. Zel'dovich and Yu. P. Raizer, *Physics of Shock Waves and High-Temperature Hydrodynamic Phenomena* (Nauka, Moscow, 1966; Academic, New York, 1967).

12. L. D. Landau and E. M. Lifshitz, *Course of Theoretical Physics*, Vol. 6: *Fluid Mechanics* (Nauka, Moscow, 1986; Pergamon, New York, 1987).

13. G. N. Abramovich, *Applied Gas Dynamics* (Nauka, Moscow, 1991), Part 1.

14. G. N. Makarov and A. N. Petin, Pis'ma Zh. Éksp. Teor. Fiz. **71**, 583 (2000) [JETP Lett. **71**, 399 (2000)].

15. G. N. Makarov and A. N. Petin, Chem. Phys. Lett. **323**, 345 (2000).

16. G. N. Makarov and A. N. Petin, Zh. Éksp. Teor. Fiz. **119**, 5 (2001) [JETP **92**, 1 (2001)].

17. G. N. Makarov and A. N. Petin, Chem. Phys. **266**, 125 (2001).

18. V. M. Apatin, L. M. Dorozhkin, G. N. Makarov, and L. M. Pleshkov, Appl. Phys. B **29**, 273 (1982).

19. V. M. Apatin and G. N. Makarov, Zh. Éksp. Teor. Fiz. **84**, 15 (1983) [Sov. Phys. JETP **57**, 8 (1983)].

20. V. M. Apatin, G. N. Makarov, and V. V. Nesterov, Pis'ma Zh. Éksp. Teor. Fiz. **73**, 735 (2001) [JETP Lett. **73**, 651 (2001)].

21. V. M. Apatin, G. N. Makarov, and V. V. Nesterov, Chem. Phys. Lett. **347**, 101 (2001).

22. G. N. Makarov, Zh. Éksp. Teor. Fiz. **120**, 1411 (2001) [JETP **93**, 1222 (2001)].

23. *CRC Handbook of Chemistry and Physics*, Ed. by D. R. Lide (CRC Press, Boca Raton, 1993-1994, 74th ed.).

Translated by V. Sakun

Oscillations of the Absorbance of PbS Nanocrystals Grown *in situ* in Langmuir–Blodgett Films of Lead Stearate

Yu. N. Savin, A. V. Tolmachev*, and Yu. A. Tolmacheva

Institute for Single Crystals, National Academy of Sciences of Ukraine, Kharkov, 61001, Ukraine
avtol@isc.kharkov.com
Received December 6, 2001

Oscillations of the absorbance of PbS nanocrystals point to the high uniformity of their sizes at the stage of "normal" growth in the matrix. The size quantization energies of the ground and the first excited states of an electron–hole pair are analyzed within the effective mass approximation. It is found that the mean radius of PbS nanocrystals is $r \approx 1.7$ nm and the potential barrier height at the contact between the semiconductor and the matrix is $V_e \approx 4.5$ eV. It is suggested that the finite barrier height is due to the action of electric fields of $\sim 10^7$ V/m in the contact regions upon breaking the polar symmetry of the dipole arrangement of matrix molecules with respect to the surfaces of growing planar nanocrystals. © *2002 MAIK "Nauka/Interperiodica".*

PACS numbers: 78.67.-n; 73.22.-f; 68.47.Pc

Optical effects due to the size quantization of the energy of an electron–hole (*e–h*) pair in semiconductor nanocrystals of radius $r < a_{ex}$, where a_{ex} is the Bohr radius of the bulk exciton, have been studied intensively in recent years (see, for example, [1, 2]). The short-wavelength ("blue") shift of the optical absorption edge of nanocrystals has been studied most comprehensively [3–6]. Oscillations of the absorbance of a nanocrystal due to transitions between its hole and electron levels with the same values of the principal (*n*) and orbital (*l*) quantum numbers present more difficulties for experimental observation. In order to observe this effect, a high degree of uniformity of nanocrystal sizes is required. Growing such nanocrystals in a dielectric matrix is a complicated problem. These effects have been observed so far in inorganic glass matrices [4]. This work reports on the observing and interpreting of the oscillating character of absorbance variations of PbS nanocrystals grown in Langmuir–Blodgett (LB) films of lead stearate.

PbS nanocrystals in LB films were synthesized in accordance with the procedure described in detail in our work [7]. This process is matrix-controlled in the sense that the synthesis of the inorganic phase is due to the diffusion of S^{2-} ions along interlayer spaces of the LB structure (polar planes in which lead ions are arranged). The morphology of these spaces determines the shape of the growing nanocrystals as plates with the thickness of the order of the semiconductor lattice constant [8, 9]. The synthesis conditions were optimized to obtain isolated nanocrystals in the matrix. Here, the multilayer LB matrix must retain periodicity, which was controlled by measuring small-angle reflection x-ray diffraction patterns [9] and checking the period of bilayer alternation (5.05 ± 0.05 nm). The synthesis conditions ($T = 305$ K, the exposure time $t_{exp} = 15$ min) were maintained so that the dependence of the mean radius of PbS nanocrystals on the exposure time had the form $r \sim t^{1/2}$ [7], which corresponded to the stage of "normal" growth and to a Gaussian dispersion of nanocrystal sizes [10].

A specific feature of the experimental absorption spectrum of nanocrystals (Fig. 1; Specord M40 UV-VIS; reference sample, an LB film of lead stearate of similar thickness) is evidently its oscillating character with a significant "blue" shift of ~1 eV of the absorption edge in reference to the spectrum of bulk PbS [5]. In order to interpret this feature quantitatively, we will use the effective mass approximation for noninteracting electrons and holes in a spherically symmetric potential well with infinite walls at a Gaussian distribution of nanocrystal radii [11]

$$h\nu_{ln} = E_g + \hbar^2 (k_{ln})^2 / 2\mu \equiv E_g + E_{ln}, \qquad (1)$$

where E_g is the energy band gap of the bulk semiconductor (for PbS, $E_g = 0.41$ eV at 300 K [12]); $\hbar$ is the Planck constant; $k_{ln} = \varphi_{ln}/r$ are the roots of the Bessel function; φ_{ln} is a universal set of numbers independent of r, $n = 1, 2, 3, \ldots$ and $l = 0, 1, 2, \ldots$; μ is the reduced exciton mass in the bulk crystal; and E_{ln} is the size quantization energy of an *e–h* pair. The radius of particles and its standard deviation σ^2 were varied. Estimating the mean radius from the position of the first experimental peak of absorbance oscillations and the energy by Eq. (1) for the ground state ($n = 1$, $l = 0$) gives $r = 2.1$ nm; that is, the condition $r < a_{ex}$ is fulfilled well (in PbS, $a_{ex} = 0.53\varepsilon m_0/\mu \approx 19.6$ nm [1], ε is the dielectric constant of the semiconductor, and m_0 is the free electron mass). However, Fig. 1 (curve *2*) demonstrates that
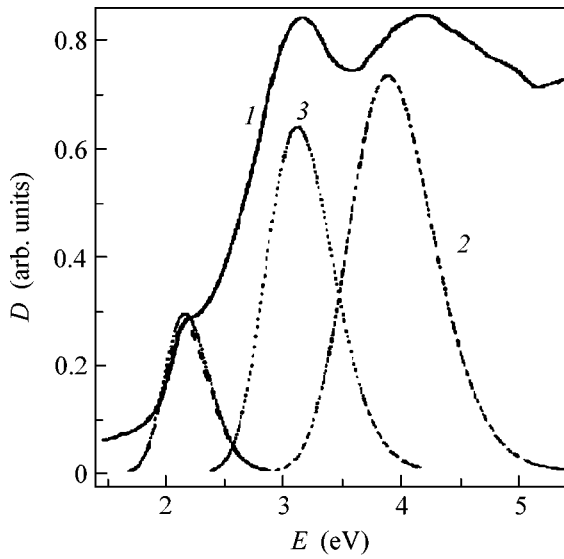
Fig. 1. (*1*) Experimental absorption spectrum of PbS nanocrystals in a 30-bilayer LB film of lead stearate and calculated spectral bands for the ground and the first excited states of an *e–h* pair in the approximation (*2*) $V_e = \infty$ and (*3*) $V_e = 12E_g$ for $\sigma^2/2r^2 = 5 \times 10^{-3}$.
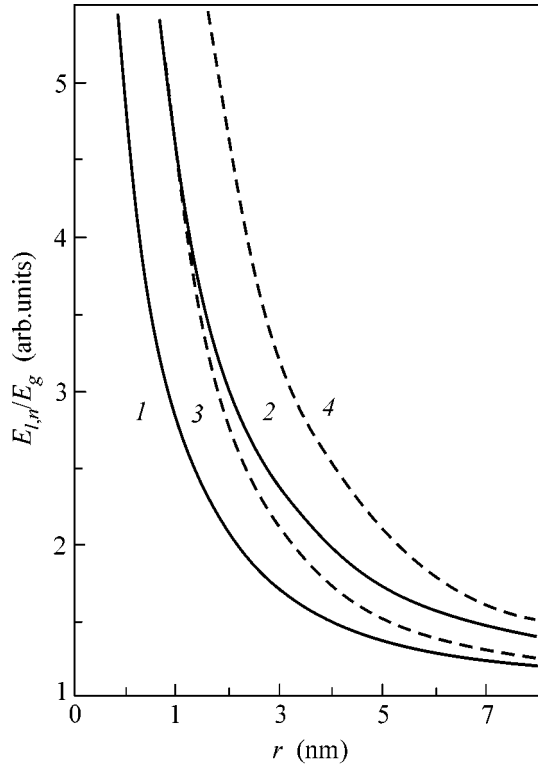

Fig. 2. Calculated energies of (*1, 3*) the ground and (*2, 4*) the first excited states of an *e–h* pair as functions of the radius of PbS nanocrystals, dashed lines correspond to $V_e = \infty$; solid lines correspond to $V_e = 12E_g$.

the position of the second peak of the spectrum for transitions with $l = 0$ calculated by Eq. (1) differs significantly from the experimental value. It may be suggested that the decrease in the gap between the ground and the excited states of an *e–h* pair observed in the experiment is due to both an increase in the Coulomb correlation of electrons and holes and the finite height of the actual potential barriers at the phase boundaries. At $r < a_{\mathrm{ex}}$, the contribution of the Coulomb interaction of carriers to the total energy of an *e–h* pair is small, $E_C/E_{ln} \sim e^2\mu r/\pi^3\varepsilon\varepsilon_0\hbar^2$ [1] (ε_0 is the electric constant), and this contribution does not exceed 5% at $r = 2.1$ nm. The polarization contribution of an interacting electron–hole pair to the potential energy of the *e–h* pair is also small in spite of the significant (~1.5 order of magnitude) difference in the dielectric constants of PbS and the matrix material [13].

In our opinion, it is necessary to take into account the fact that the motion of photoexcited carriers in nanocrystals located in polar planes of the LB matrix is affected by the confining potential generated by polar groups of amphiphilic molecules having a large area of contacts with planar boundaries of nanocrystals. Its value is finite; therefore, in principal, wave functions of carriers can penetrate the barrier at the boundary with the matrix. Let us determine the energies of the two lowest states E_{01} and E_{11} of an *e–h* pair as functions of the nanocrystal size at a finite value of the potential V_e at the nanocrystal–matrix boundary [14]

$$\tan(k_{i01}r)/(k_{i01}r) = \{1 - (1 + q_{i01}r)m_{i1}/m_{i2}\}^{-1}, \quad (2)$$

$$\tan(k_{i11}r)/(k_{i11}r) = \{1 + (k_{i11}r)^2/\{[m_{i1}/m_{i2} \times (2 + 2q_{i11}r + q_{i11}^2r^2)/(1 + q_{i11}r)] - 2\}\}^{-1}. \quad (3)$$

In Eq. (2), $k_{iln} = (2m_{1i}E_{iln}/\hbar^2)^{1/2}$ and $q_{iln} = [2m_{2i}(V_i - E_{iln})/\hbar]^{1/2}$; $i = e, h$; m_{1i} is the carrier mass in the nanocrystal; and m_{2i} is the carrier mass in the matrix.

Figure 2 displays $E_{01}(r)$ and $E_{11}(r)$ curves for various V_e obtained by numerically solving Eqs. (2) and (3) for $m_{1e}/m_0 = 0.085$, $m_{1h}/m_0 \approx 0.101$, and $m_{2e}/m_0 \approx 1$. It is assumed that $m_{2e} \approx m_0$ and $V_h = \infty$ for holes. Electrons in a real dielectric matrix are localized, and $m_{2e}/m_0 > 1$; therefore, the ratio of effective electron masses in the matrix to electron mass in the nanocrystal can actually be smaller than the value $m_{1e}/m_{2e} = 0.085$ assumed in calculations. However, it can be easily shown that a decrease in m_{1e}/m_{2e} by a factor of, for example, two leads to an insignificant change in the difference $E_{11} - E_{01}$ within the range ~ 6–7%; that is, the approximation $m_{2e} \approx m_0$ is quite acceptable. Figure 2 demonstrates that a decrease in the potential barrier height leads to a decrease in the size quantization energy. Owing to the fact that, when V_e decreases, the excited state energy decreases more rapidly than the ground state energy, the difference $E_{11}(r, V) - E_{01}(r, V)$ also decreases. A

comparison of the calculated values $E_{01}(r, V_e)$ and $E_{11}(r, V_e) - E_{01}(r, V_e)$ with the experimental E_{01} and $E_{11} - E_{01}$ values allows one to refine the mean radius of PbS nanocrystals $r \approx 1.7$ nm and to estimate $V_e \approx 12E_g$. The corresponding two bands of the calculated absorption spectrum are represented by curves *3* in Fig. 1.

An analysis of particular physical reasons for the formation of a potential barrier at the boundaries of a planar nanocrystal with the LB matrix is the subject of a separate study; however, we would like to emphasize here that an LB film, as a whole, retains its ordering in the process of "normal" nanocrystal growth. However, the polar matrix planes become distorted in the vicinities of PbS nanocrystal formation and internal stresses in the matrix increase [9]. It is evident that this will result in a perturbation of the polar symmetry and, as a consequence, in the occurrence of local regions of spontaneous polarization and electric fields in the nearest environment of nanocrystals. Estimates show that the strength of the total electric field of the intrinsic and induced (as a result of polarizing electron shells of the oxygen bound in carbonyl and hydroxyl groups of matrix molecules by the PbS lattice [15]) dipoles can reach $\sim 10^7$ V/m at a density of polar stearic acid molecules (dipole moments ≈ 2 D) of $\sim 4 \times 10^{18}$ cm^{-2} in the simple case of azimuthal misalignment of their dipole moments by $\sim 10°$. This is quite a real value [16] to decrease the work function of the surface of PbS nanocrystals in the polar environment of an LB matrix.

REFERENCES

1. A. D. Yoffe, Adv. Phys. **42**, 173 (1993).

2. I. P. Suzdalev and P. I. Suzdalev, Usp. Khim. **70**, 203 (2001).

3. D. M. Mittlemen, R. W. Schoenlein, J. J. Shiang, *et al.*, Phys. Rev. B **49**, 14435 (1994).

4. S. Gaponenko, U. Woggon, M. Salech, *et al.*, J. Opt. Soc. Am. B **10**, 1947 (1993).

5. Y. Wang, A. Suna, W. Mahler, *et al.*, J. Chem. Phys. **87**, 7315 (1987).

6. Yu. N. Savin, Funct. Mater. **4**, 515 (1997).

7. Yu. Savin, T. Pak, and A. Tolmachev, Mol. Cryst. Liq. Cryst. **361**, 223 (2001).

8. U. N. Roy, Aika Ingale, Shramana Mishra, *et al.*, Vide: Sci., Tech. Appl. **55**, 247 (2000).

9. A. G. Fedorov, Yu. N. Savin, I. A. Shneiderman, and A. V. Tolmachev, Funct. Mater. **6**, 556 (1999).

10. V. V. Slezov and V. V. Sagalovich, Usp. Fiz. Nauk **151**, 67 (1987) [Sov. Phys. Usp. **30**, 23 (1987)].

11. Al. A. Éfros and A. A. Éfros, Fiz. Tekh. Poluprovodn. (Leningrad) **16**, 1209 (1982) [Sov. Phys. Semicond. **16**, 772 (1982)].

12. *Tables of Physical Quantities: Handbook*, Ed. by I. K. Kikoin (Atomizdat, Moscow, 1976).

13. N. A. Efremov and S. I. Pokutniĭ, Fiz. Tverd. Tela (Leningrad) **32**, 1637 (1990) [Sov. Phys. Solid State **32**, 955 (1990)].

14. D. B. Tran Thoai, Y. Z. Hu, and S. W. Koch, Phys. Rev. B **42**, 4137 (1990).

15. F. F. Vol'kenshteĭn, *Physicochemistry of Semiconductor Surface* (Nauka, Moscow, 1973).

16. S. Sze, *Physics of Semiconductor Devices* (Wiley, New York, 1981; Mir, Moscow, 1984), Vol. 1.

Translated by A. Bagatur'yants

Anomalous Transport Properties of a Paramagnetic NiTiO$_3$ + HTSC Two-Phase System Representing a Random Josephson Junction Network

M. I. Petrov*, D. A. Balaev, K. A. Shaĭkhutdinov, and S. I. Popkov

Kirenskiĭ Institute of Physics, Siberian Division, Russian Academy of Sciences, Krasnoyarsk, 660036 Russia
*e-mail: smp@iph.krasnoyarsk.su
Received October 12, 2001; in final form, December 26, 2001.

Composites representing a network of random Josephson junctions and characterized by the compositions 92.5 at. % Y$_{3/4}$Lu$_{1/4}$Ba$_2$Cu$_3$O$_7$ + 7.5 at. % NiTiO$_3$ and 92.5 at. % Y$_{3/4}$Lu$_{1/4}$Ba$_2$Cu$_3$O$_7$ + 7.5 at.% MgTiO$_3$ are synthesized, and their magnetoresistance properties are studied. The temperature dependence of the resistance $R(T)$ measured for the composite that contains the paramagnetic NiTiO$_3$ compound exhibits a characteristic feature below the superconducting transition temperature T_c of the high-T_c superconductor, namely, a region where R is independent of the current j and weakly depends on the magnetic field H. Below a certain temperature T_m, a strong dependence of R on j and H is observed, which is peculiar to a network of Josephson junctions. The dependences $R(T, j, H)$ obtained for the "reference" samples with the nonmagnetic MgTiO$_3$ compound exhibit no such features. The anomalous behavior of the HTSC + NiTiO$_3$ composite is explained by the effect produced by the magnetic moments of Ni atoms in the insulating barriers on the transport current. © 2002 MAIK "Nauka/Interperiodica".

PACS numbers: 75.70.Cn; 74.50.+r; 74.80.Dm

Josephson structures with different types of magnetic ordering in the barriers (superconductor–ferromagnet–superconductor or superconductor–paramagnet–superconductor) have been intensively studied on the basis of conventional superconductors for years, both theoretically and experimentally [1–13]. These structures attract the interest of researchers, because they exhibit such effects as the nonmonotone temperature dependence of the critical current [6, 7, 10–12], the presence of π junctions [6, 7, 10–12], the reduction of the superconducting properties, and the characteristic behavior of magnetoresistance [13]. The strong chemical activity of high-T_c superconductors (HTSCs) hinders the fabrication of single Josephson junctions of the aforementioned kinds on their basis. However, the characteristic features of the resistive state of such junctions can be observed on two-phase composites whose one ingredient is an HTSC and the other is a compound with magnetic ordering. Technologically, the fabrication of such composites presents no difficulties. The necessary condition for their synthesis is the absence of strong chemical interaction between the initial ingredients of the composite. Earlier, it was shown [14–18] that, below the transition temperature T_c of the superconducting grains, the transport properties of composite HTSCs prepared by the fast sintering technique represent a Josephson junction network.

We studied composite samples with the volume content of the HTSC 92.5 vol % and the content of NiTiO$_3$ (or MgTiO$_3$) 7.5 vol %. The samples were prepared as follows. First, the initial components were synthesized. The Y$_{3/4}$Lu$_{1/4}$Ba$_2$Cu$_3$O$_7$ superconductor was synthesized by the conventional ceramic technology. The NiTiO$_3$ and MgTiO$_3$ compounds were obtained from NiO, MgO, and TiO$_2$ (high purity grade) also by the ceramic technology, by heating at 1250°C within 100 h with five intermediate grindings. Then, the initial components of the future composite were taken in the necessary proportion and grinded and mixed in an agate mortar, after which they were pressed into pellets. The pellets were placed for 2 min in an furnace heated to 910°C and then placed in another furnace heated to 350°C, in which they were annealed within 3 h to saturate them with oxygen. After this, the pellets were cooled together with the furnace. For the samples used in our study, we introduce he following notation: S+7.5(Ni) for composites with NiTiO$_3$, and S+7.5(Mg) for composites with MgTiO$_3$. Since the MgTiO$_3$ compound is nonmagnetic and isostructural with NiTiO$_3$, the S+7.5(Mg) composites were used as reference to reveal the effect of the magnetic moments of nickel.

Magnetic measurements performed for the synthesized NiTiO$_3$ showed that this material is an antiferromagnet with the Néel point ~ 22 K and, above 22 K, it is a paramagnet. The experimental value of the effective moment per atom was found to be ~4 μ_B. These data agree well with the results obtained in [19].

The X-ray structure studies of S+7.5(Ni) and S+7.5(Mg) composite samples revealed the presence of

only two phases (within the accuracy of the X-ray analysis): the 1-2-3 structure and the ilmenite structure. No foreign reflections were observed. The relative intensities of the reflections correspond to the volume contents of the composite components. The measurements of the temperature dependences of magnetization $M(T)$ for the S+7.5(Ni) and S+7.5(Mg) composite samples showed that both composites have a single superconducting phase with the transition temperature $T_c = 93.5$ K, which coincides with T_c of the initial polycrystalline $Y_{3/4}Lu_{1/4}Ba_2Cu_3O_7$ HTSC, which was annealed in the same way as the composites.

Figure 1 presents the dependences $R(T)$ measured for the S+7.5(Mg) composite by the four-probe method at different strengths of the external magnetic field (the magnetic field is perpendicular to the current) (Fig. 1a) and at different values of the transport current j (Fig. 1b). The behavior of these dependences is typical of the composites with an insulator, such as HTSC + CuO [15] and HTSC + Pb_2ScTaO_6 [18], with a short sintering time. The onset of the superconducting transition is observed at $T_c = 93.5$ K for all transport currents in small magnetic fields (<1 kOe), which coincides with T_c of the initial HTSC. At this temperature, the superconducting transition of the HTSC grains is observed in the form of a sharp decrease in the resistance. The magnitude of the resistivity drop is independent of both the external field and the current and is determined by the volume content of the superconducting component in the composite. The inset in Fig. 1b shows (on an enlarged scale) the dependences $R(T, j)$ for the composite. One can see that all these dependences are functions of the transport current (the $I–V$ characteristics are nonlinear) immediately below the superconducting transition temperature. The dependences $R(T, H)$ (Fig. 1a) behave in a similar way. The broadening of the superconducting transition in magnetic fields 1–60 kOe is related to the penetration of the magnetic field into the superconducting crystallites. As the temperature decreases further, the resistance smoothly decreases, which corresponds to the transition of the network of Josephson weak links. The temperature at which the resistance becomes zero decreases with increasing current and magnetic field. These dependences, $R(T, j)$ and $R(T, H)$, can be described in terms of the thermally activated phase slippage mechanism [20], as was done for HTSC + CuO composites in [15].

Figure 2 shows the temperature dependences of the resistance $R(T)$ of the S+7.5(Ni) composite for different strengths of the external magnetic field (0–60 kOe) (Fig. 2a) and different transport currents j (Fig. 2b). The onset of the superconducting transition looks similar to that observed for the S+7.5(Mg) samples. However, as the temperature decreases, the dependences $R(T)$ exhibit a plateau (see the inset in Fig. 2b) within which the dependences $R(T, j)$ are not functions of the current (the $I–V$ characteristics are linear) and R weakly
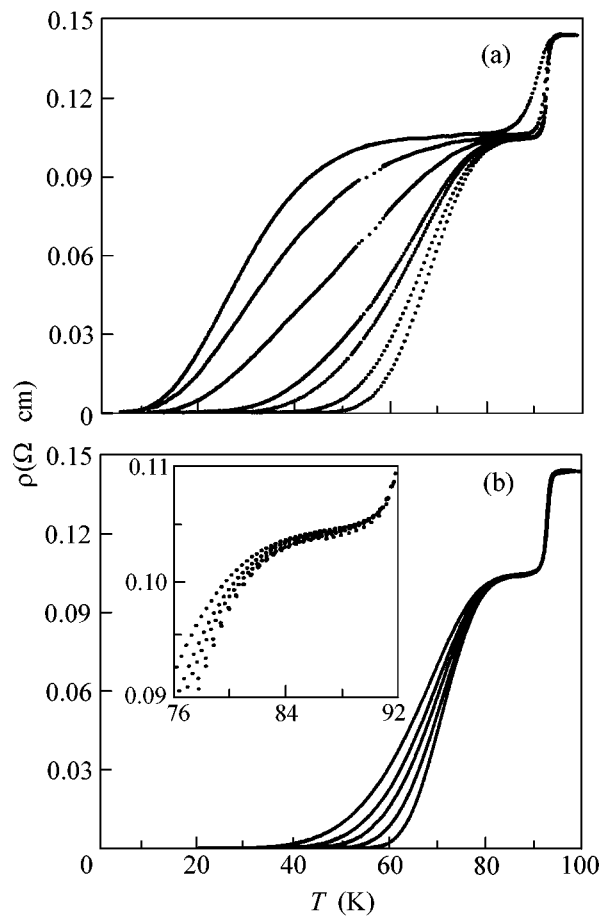

Fig. 1. Temperature dependences of the resistivity of an S+7.5(Mg) sample (a) for different strengths of the external magnetic field H at $j = 27$ mA/cm^2 and (b) for different values of the current density j at $H = 0$: (a) $H = 20$ Oe, 38 Oe, 80 Oe, 116 Oe, 1 kOe, 10 kOe, and 60 kOe (from right to left); (b) $j = 27$, 135, 270, 407, and 520 mA/cm^2 (from right to left).

depends on the magnetic field. Only starting from a certain temperature T_m do the dependences $R(T)$ become functions strongly dependent on both the magnetic field (Fig. 2a) and the current (Fig. 2b), as in the case of the S+7.5(Mg) composites. In high magnetic fields (<10 kOe), the point T_m becomes spread, but no displacement of this temperature is observed. The latter is confirmed by Fig. 3, which presents the temperature dependence of the derivative dR/dT. As the transport current and the magnetic field increase, the temperature corresponding to the zero resistance value decreases. We also note that the dependences $R(T, H)$ and $R(T, j)$ behave in different ways, which is presumably related to the effect of the distribution function of the parameters of the Josephson junctions formed in the composites on the behavior of $R(T)$. The dependences $R(T, j)$ for the S+7.5(Ni) composite (Fig. 2b) cannot be described in the framework of the approach proposed in [20] and used for the HTSC + CuO composites in [15].
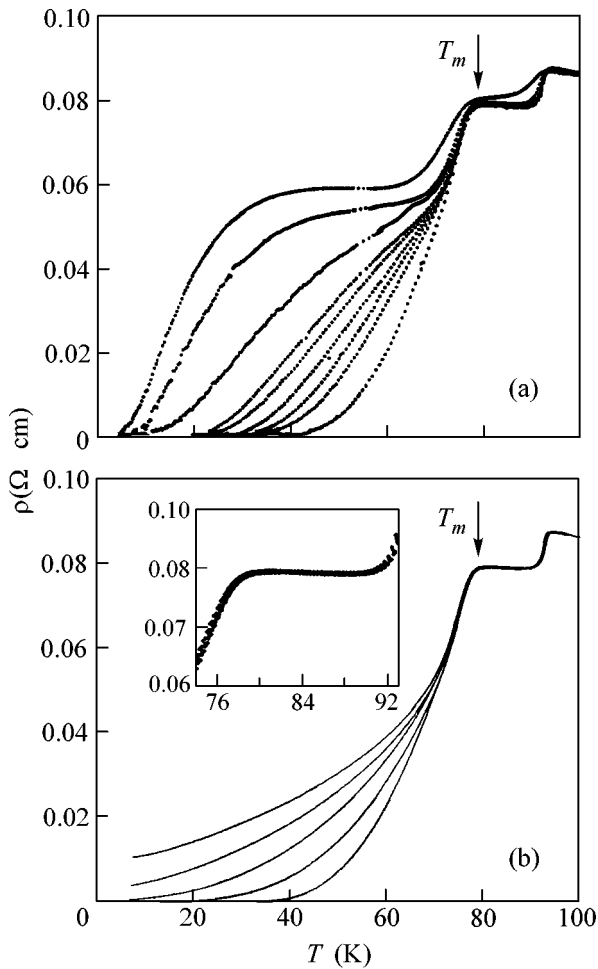
Fig. 2. Temperature dependences of the resistivity of an S+7.5(Ni) sample (a) for different strengths of the external magnetic field H at $j = 20$ mA/cm^2 and (b) for different values of the current density j at $H = 0$: (a) $H = 0$, 20 Oe, 38 Oe, 80 Oe, 116 Oe, 200 Oe, 1 kOe, 10 kOe, and 60 kOe (from right to left); (b) $j = 20$, 100, 200, 300, and 400 mA/cm^2 (from right to left).
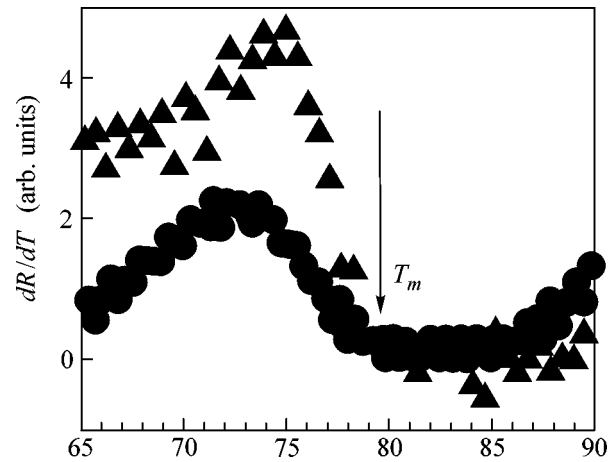

Fig. 3. Fragments of the temperature dependences of the derivative dR/dT for the dependences obtained at $H = 0$ (triangles) and 60 kOe (circles) for an S+7.5(Ni) sample.

The appearance of the aforementioned feature for the S+7.5(Ni) composites, i.e., the appearance of the temperature T_m, cannot be explained by any kind of chemical mechanism (this statement is confirmed by the S+7.5(Mg) sample used as reference). Taking into account that both types of samples were prepared by identical procedures, one can conclude that the feature in question is associated with the use of the NiTiO$_3$ paramagnet as the second component of the composite. It is the presence of magnetic moments of nickel atoms that gives rise to the anomalous behavior of the dependences $R(T)$.

This behavior can be explained by the mechanism similar to that proposed in [21, 22]. The cited publications report on the resistance measurements along the c axis of YBa$_2$Cu$_3$O$_7$ [21] and Bi$_2$Sr$_2$CaCu$_2$O$_8$ [22] single crystals placed in a strong magnetic field up to 18 T

coplanar with the a–b plane of the crystal. A broadening of the resistive transition was observed, and the curves $\rho(T)$ showed two characteristic regions: one immediately below T_c with ρ independent of j and the other below a certain point T_m with ρ not being a function of the current. The authors of these publications [21, 22] believe that the point T_m is the melting temperature of the Abrikosov vortex lattice. Evidently, in the aforementioned geometry ($H \parallel a, b$), the magnetic field penetrates into the nonsuperconducting layers of the quasi-two-dimensional single crystal to a greater extent than into the superconducting layers with the generation of Abrikosov vortices. When the current flows along the c axis, the charge carriers tunnel from the superconducting layers through the nonsuperconducting ones, in which the spins of the carriers interact in the Zeeman way with the external field. In addition, Abrikosov vortices can move, and, at temperatures above T_m, they move without pinning, which leads to a specific form of the temperature dependence of magnetoresistance.

Our HTSC + NiTiO$_3$ composite can be considered as a macroscopic analog of the experiment described above. In fact, the charge carriers tunnel between the superconducting grains through the paramagnet in which the spins of the carriers become involved in the exchange interaction (an approximate analog of the Zeeman interaction) with the magnetic moments of nickel. The probability of such an interaction is close to unity, because $a_0 < \xi_0$, where a_0 is the lattice constant of NiTiO$_3$, i.e., the distance between the magnetic moments, and ξ_0 is the coherence length. The paramagnetic material NiTiO$_3$ induces a fluctuating effective magnetic field (evidently, its time average strength is equal to zero), which penetrates into the superconducting grains to the depth λ (~1000 Å) [23]. This field causes the formation of Abrikosov vortices in the near-

surface layer of the HTSC adjacent to $NiTiO_3$. In the interval between the melting temperature of the Abrikosov vortex lattice T_m and the superconducting transition temperature T_c, the resistance of the sample does not depend on the transport current, as in the case of [21, 22]. Below this interval, the Abrikosov vortices are pinned inside the HTSC grains. In this case, the I–V characteristic depends on the transport current density and a strong dependence of the resistance on the magnetic field takes place (Fig. 2).

We note that the dependences we obtained resemble the results reported in a recent publication [13] where the transport properties of single Josephson junctions with conventional superconductors, Nb/Al/Gd/Al/Nb (superconductor–ferromagnet–superconductor), were studied and similar dependences $R(T)$ were obtained. Below the superconducting transition temperature, these dependences also displayed two characteristic regions. Immediately below T_c, the dependences $R(T)$ in [13] did not depend on the transport current, and, only starting from a certain temperature (analogous to T_m), the curves $R(T)$ were found to depend on j. However, the effect of the ferromagnetism of Gd on the tunneling of charge carriers through this kind of barrier was unfortunately not analyzed in [13].

REFERENCES

1. I. O. Kulik, Zh. Éksp. Teor. Fiz. **49**, 1211 (1965) [Sov. Phys. JETP **22**, 841 (1966)].

2. H. Shiba and T. Soda, Prog. Theor. Phys. **41**, 25 (1969).

3. L. N. Bulaevskiǐ, V. V. Kuziǐ, and A. A. Sobyanin, Pis'ma Zh. Éksp. Teor. Fiz. **25**, 314 (1977) [JETP Lett. **25**, 290 (1977)].

4. J. L. Paterson, J. Low Temp. Phys. **35**, 371 (1979).

5. J. Niemeyr and G. von Minnigerode, Z. Phys. B **36**, 57 (1979).

6. L. N. Bulaevskiǐ, A. I. Buzdin, and S. V. Panjukov, Solid State Commun. **44**, 539 (1982).

7. A. I. Buzdin, B. Bujicic, and M. Yu. Kupriyanov, Zh. Éksp. Teor. Fiz. **101**, 231 (1992) [Sov. Phys. JETP **74**, 124 (1992)].

8. S. V. Kuplevakhskiǐ and I. I. Fal'ko, Fiz. Tverd. Tela (St. Petersburg) **34**, 183 (1992) [Sov. Phys. Solid State **34**, 96 (1992)].

9. A. S. Borukhovich, Usp. Fiz. Nauk **169**, 737 (1999).

10. M. Fogelström, Phys. Rev. B **62**, 11812 (2000).

11. Y. Tanaka and S. Kashiwaya, J. Phys. Soc. Jpn. **69**, 1152 (2000).

12. V. V. Ryazanov, V. A. Oboznov, A. Yu. Rusanov, *et al.*, Phys. Rev. Lett. **86**, 2427 (2001).

13. O. Bourgeois, P. Gandit, A. Sulpice, *et al.*, Phys. Rev. B **63**, 064517 (2001).

14. M. I. Petrov, D. A. Balaev, S. V. Ospishchev, *et al.*, Phys. Lett. A **237**, 85 (1997).

15. M. I. Petrov, D. A. Balaev, K. A. Shaǐkhutdinov, and K. S. Aleksandrov, Fiz. Tverd. Tela (St. Petersburg) **41**, 969 (1999) [Phys. Solid State **41**, 881 (1999)].

16. M. I. Petrov, D. A. Balaev, K. A. Shaǐkhutdinov, and S. G. Ovchinnikov, Fiz. Tverd. Tela (St. Petersburg) **40**, 1599 (1998) [Phys. Solid State **40**, 1451 (1998)].

17. M. I. Petrov, D. A. Balaev, S. V. Ospishchev, and K. S. Aleksandrov, Fiz. Tverd. Tela (St. Petersburg) **42**, 791 (2000) [Phys. Solid State **42**, 810 (2000)].

18. D. Berling, B. Loegel, A. Mehdaoui, *et al.*, Supercond. Sci. Technol. **11**, 1292 (1998).

19. G. S. Heller, J. J. Stickler, S. Kern, and A. Wold, J. Appl. Phys. **34**, 1033 (1963).

20. V. Ambegaokar and B. I. Halperin, Phys. Rev. Lett. **22**, 1364 (1969).

21. M. Charalambous, J. Chaussy, and P. Lejay, Phys. Rev. B **45**, 5091 (1992).

22. M. S. Fuhrer, K. Ino, K. Oka, *et al.*, Physica C (Amsterdam) **282–287**, 2041 (1997).

23. A. P. Malozemoff, in *Physical Properties of High Temperature Superconductors*, Ed. by D. M. Ginsberg (World Scientific, Singapore, 1989; Mir, Moscow, 1990), Vol. I.

Translated by E. Golyamina

Ultrathin Co/Cu(110) Film as a Lattice of Ferromagnetic Grains with Dipolar Interaction

E. Z. Meĭlikhov* and R. M. Farzetdinova

*Institute of Molecular Physics, Russian Research Centre Kurchatov Institute,
pl. Akademika Kurchatova 1, Moscow, 123182 Russia*
* e-mail: meilikhov@imp.kiae.ru
Received December 29, 2001

The well-known fact of magnetic ordering in ultrathin Co films (with an effective thickness of several mono-atomic layers) on a single-crystal Cu(110) substrate is described quantitatively using the model according to which the thin film is a lattice of three-dimensional ferromagnetic grains with dipole–dipole interactions. The critical film thickness corresponding to the ferromagnetic transition and the corresponding Curie temperature were calculated.© 2002 MAIK "Nauka/Interperiodica".

PACS numbers: 75.70.Ak

To date, much experimental work has been devoted to the study of magnetic ordering in ultrathin Fe, Co, and Ni films [1]. Although it has been found that a long-range ferromagnetic order is established in films having a certain effective thickness, the nature and regularity of this phenomenon still remain to be clarified. The main difficulty in the generalization and adequate description of the experimental results is caused by the complex character of the film growth process, because the morphology and properties of these films depend on many factors and, in particular, on the type of substrate (its material, crystallinity, surface orientation, cleanliness, temperature, etc.) and growth conditions (atmosphere pressure and composition, growth rate, methods of material evaporation, etc.). For the results to be reproducible, it is necessary to carefully control and keep constant many parameters during the course of the experiment. As for the development of a physical notion of the mechanism for establishing magnetic order in ultrathin films, the control of the topology of such films and, in particular, the geometry and magnetic properties of "islands" composed of Co (Fe, Ni), the substrate surface area covered by these islands, the film structure, and the evolution of the relevant parameters during the film growth are highly important.

One recent work [2] is noteworthy in this respect. It was shown in that work that, at a sufficiently high temperature (e.g., 300 K) of a single-crystal Cu(110) substrate, the deposited Co film grew through "natural lithography," i.e., through the formation of nuclei (distributed more or less homogeneously over the substrate area) which transformed into ellipsoidal grains with major axes aligned (to within a small scatter of ~5°–10°) with the substrate [001] axes. It was established that the size of these grains increased in the course of film growth, but both the separation between their centers and the grain shapes (i.e., their eccentricity) remained unchanged.

The effective thickness d of such an inhomogeneous film composed of grains is equal to the thickness of a *homogeneous* film containing the same number of atoms. It is the effective thickness d which is measured in the experiments (from the amount of material deposited on the substrate) and ordinarily described in terms of the number of monoatomic layers (MLs). The experiment shows that such films become ferromagnetic only if their thickness is sufficiently large (critical). The authors of [2] assume that the critical thickness d_c is equal to the thickness for which the hysteresis loop of the film demonstrates nonzero coercivity for the first time. According to their measurements, $d_c \approx 4.6$ ML, although a noticeable nonlinearity in the magnetic-field dependence of film magnetization, being the consequence of intergrain interaction, appears even at $d \approx 4$ ML.

We assume that the process of transformation to the ferromagnetic state can be associated with a change in the magnetic state of the lattice of ellipsoidal Co grains coupled together by the long-range dipole–dipole interactions. The appropriate model is considered below.

Magnetic state of a system of ferromagnetic grains coupled by the dipolar interaction and magnetism of ultrathin films. Let us consider a system of identical *magnetically anisotropic* ferromagnetic grains with magnetic moments μ and centers lying in the x, z plane and positioned at the sites of a *two-dimensional rectangular* lattice with lattice constants l_x and l_z. Let the easy axes of the grains and, hence, their magnetic moments also lie in the x, z plane and let them be parallel to each other and form angle θ with the x axis. With allowance made for the long-range dipole–dipole

interaction, the magnetic state of this system is determined by the magnetic field

$$H_d = \sum_{m,n} H_{mn}$$

created in the volume of an individual grain (for definiteness, positioned at the origin of coordinates) by all remaining grains. In this expression, H_{mn} is the field component (parallel to the grain magnetic moments) created at the origin by the grain centered at the point (ml_x, nl_z), where m and n are integers; the sum does not include the term with $m = n = 0$.

The interaction energy between the chosen grain and the magnetic field H_d is

$$W_d = -(\mu/V)\int_V H_d(r)dV, \qquad (1)$$

where the integration is over the volume of the central grain. The ground state of the system corresponds to the configuration of grain magnetic moments μ_{mn}, for which the energy W_d is minimum. In our case, only one ferromagnetic configuration (the grain magnetic moments are aligned with their major axes and are parallel to each other) is possible. As to the antiferromagnetic state of the system, we restrict ourselves to the situation where the grain magnetic moments form two identical magnetic sublattices with antiparallel magnetic moments. Then $\mu_{mn} = \mu\exp[i(\phi_x m + \phi_z n)]$, where $\phi_x = \phi_z = 0$ for the ferromagnetic state. The antiferromagnetic states S_{10}, S_{01}, and S_{11} (Fig. 1) correspond, respectively, to $(\phi_x = 0, \phi_z = \pi)$, $(\phi_x = \pi, \phi_z = 0)$, and $(\phi_x = \phi_z = \pi)$.

Let i_1 be the absolute value of sublattice magnetization (in the ferromagnetic state, the total magnetization is $i = 2i_1$, and $i = 0$ in the antiferromagnetic state). According to the mean-field theory, the energy of dipole–dipole interaction is proportional to the magnetization i_1, i.e., $W_d = -\lambda i_1$. Of all the states considered (ferromagnetic and three antiferromagnetic), the state corresponding to the largest dipole–dipole interaction parameter λ is energetically most favorable. Therefore, to elucidate the character of the ground state of the system, it would suffice to determine and compare with each other these parameters for the ferromagnetic and different antiferromagnetic configurations of the grain magnetic moments.

As for the lattice magnetization i_1, it is determined from the self-consistent equation of the mean-field theory

$$i_1 = i_0\tanh[\lambda i_1/kT], \qquad (2)$$

where $i_0 = (1/2)\mu N$ and $N = 1/l_x l_z$ is the surface concentration of grains. As usual, this equation determines the Curie temperature $T_C = \lambda i_0/k$ for the system. However, it should be noted that Eq. (2) applies only if the difference in energies W_d of the ferro- and antiferromagnetic
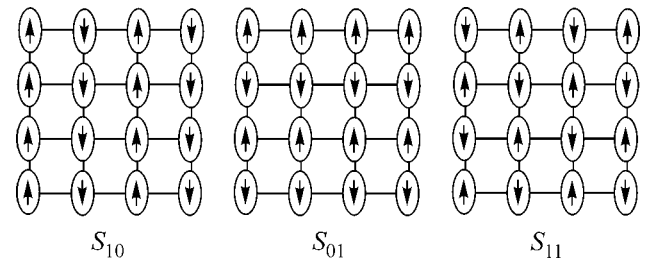
Fig. 1. Antiferromagnetic structures S_{10}, S_{01}, and S_{11} of the rectangular lattices of magnetic moments.

states is large compared to kT. Otherwise the thermal fluctuation of magnetic order must be taken into account.

We will restrict ourselves to the consideration of three-dimensional grains shaped like ellipsoids of revolution with easy axes aligned with their major axes. The method of approximate calculation of the intergrain dipole–dipole interaction energy W_d for the lattice of such grains was developed in [3]. This method is based on the use of the following (giving an accuracy of ~1%) expression for the energy w_d of dipolar interaction between two ellipsoidal grains, one of which is centered at the origin of coordinates:

$$w_{mn} = -\mu H_{mn},$$

$$H_{mn} = \frac{1}{2}\left[3\left(\frac{\Psi_{mn}(a) - \Psi_{mn}(-a)}{2a}\right) + \Psi'_{mn}(0)\right] \\ - \frac{3}{20}a^2\left(1 + \frac{32}{9\pi}\frac{b^2}{a^2}\right)\Psi'''_{mn}(0), \qquad (3)$$

where

$$\Psi_{mn}(x') = \left[\frac{3\mu(x_0 + x')}{e^3 a^3}\right](\operatorname{arctanh}t - t) \qquad (4)$$

$$t = e/\sqrt{1 + \xi}$$

is the magnetic field potential produced by the "central" grain on the axis of another grain centered at the point with coordinates $x_0 = ml_x$, $z_0 = nl_x \equiv \beta nl_x$ ($x' = x - x_0$); ξ is the larger root of equation $((z_0/a)^2/(1 - e^2 + \xi) + [(x_0 + x')/a]^2/(1 + \xi) = 1$; $\Psi'_{mn}(0) = \partial\Psi_{mn}/\partial x'|_{x'=0}$; and $\Psi'''_{mn}(0) = \partial^3\Psi_{mn}/\partial x'^3|_{x'=0}$.

Therefore, the parameter λ governing the type of magnetic order in the plane lattice of ellipsoidal magnetic grains has the form

$$\lambda = 2\left(\frac{\mu\beta}{l_x}\right)\sum_{m,n}(H_{mn}/H_0)e^{i(\phi_x m + \phi_x n)}, \qquad (5)$$
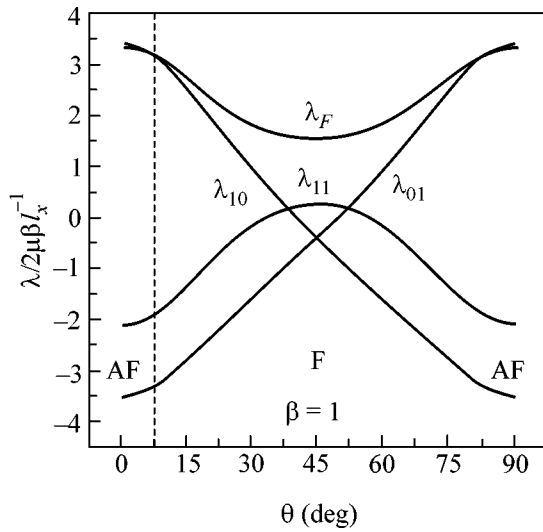
$$H_0 = \mu/l_x^3,$$

Fig. 2. Dipole–dipole interaction parameters for the rectangular ferro- and antiferromagnetic grain lattices vs. tilt angle of their magnetic moments. Ellipsoidal grains: $e = 0.95$ and $l_x/a = 3$.

where $\beta = l_z/l_x$ is the lattice extension coefficient.

The magnetic phase diagram of the system can be constructed after the calculation of the interaction parameters λ for the different magnetic configurations of grain magnetic moments and comparison of these parameters with each other. For the rectangular ferro- and antiferromagnetic lattices of ellipsoidal grains, the dependences of these parameters on the tilt angle of their magnetic moments are presented in Fig. 2. Examples of magnetic phase diagrams are given in Fig. 3 for two lattices of ellipsoidal grains with different scale ratios l_x/a. For a sufficiently small value of this ratio, the lattices exist whose ground states are ferromagnetic even at $\theta = 0$ (e.g., for $l_x/a = 2.5$ all lattices with $\beta < 1$ are of this type). Moreover, one can see from the comparison of Figs. 3a and 3b that, at small angles θ, the system may undergo transition from the antiferromagnetic to the ferromagnetic state upon a decrease in this ratio.

We assume that it is precisely this feature of the phase diagrams of the lattices of ellipsoidal grains that accounts for the magnetic phase transitions in thin films of magnetic metals. Within the framework of our model, the film growth process reduces only to a change in the scale factor, which is equal to the length a of the major semiaxis of the ellipsoidal grain in our case.

For the quantitative description of the film growth process, it is necessary to relate the parameters characterizing grain size and shape (semiaxis length a and eccentricity e) to the effective thickness of the film d. To do this, one can use the experimentally determined (for the same system) relation $\epsilon = \epsilon(d)$ between the fraction ϵ of a free (unoccupied by the Co grains) substrate sur-
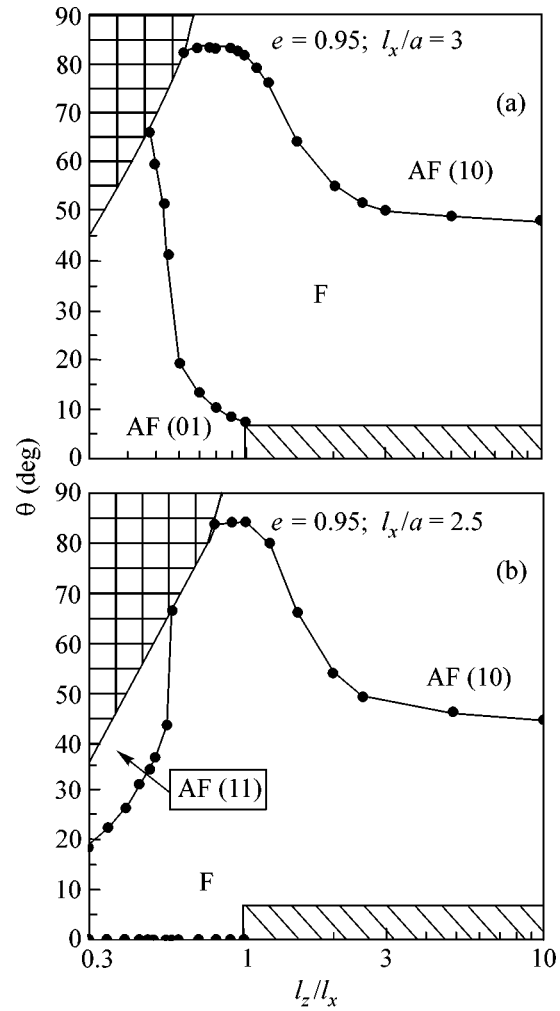

Fig. 3. Magnetic phase diagrams of the rectangular lattices of ellipsoidal grains with eccentricity $e = 0.95$ for $l_x/a = $ (a) 3 and (b) 2.5. The boundaries of the hatched regions, which are "forbidden" by the geometry of the system, correspond to the contacting grains. Because of the limited accuracy of the model, the exact form of the interphase boundaries cannot be determined in the region $\theta \ll 10°$, $\beta > 1$. It is only known that these boundaries lie inside the lower hatched regions.

face and the film effective thickness [4]. Evidently, the surface fraction covered by the grains is $1 - \epsilon = \pi ab/l_x l_z$. Therefore, the desired expression for the parameter l_x/a determining the character of the magnetic phase diagram is $l_x/a = [l_x^{(0)}/a^{(0)}][(1 - \epsilon(d^{(0)}))/\epsilon(d)]$, where the parameters labeled (0) correspond to the thinnest film (in the experiments in [4], $d^{(0)} = 0.9$ ML). The corresponding function constructed on the basis of the experimental data reported in [4] for the Co film on a Cu(110) substrate is shown in Fig. 4.

According to [2], the grain shape is close to the ellipsoid with eccentricity $e \approx 0.95$, and the ratio of the average intergrain distances ("lattice constants") is $\beta = l_z/l_x = 0.5–1$. As for the angles θ of grain orientation, it
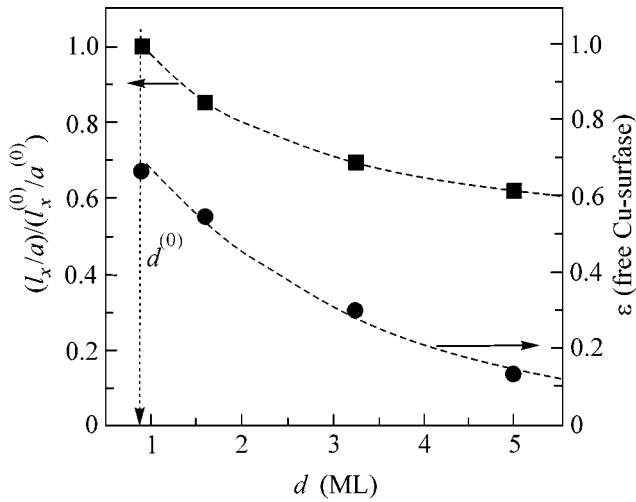
Fig. 4. (lower curve) Experimental dependence of the fraction $\epsilon(d)$ of the free (unoccupied by Co) surface of Cu(110) substrate on the effective thickness of the Co film [4] and (upper curve) the corresponding calculated values of the parameter l_x/a. The parameters labeled (0) refer to the thinnest film with thickness $d_0 \approx 0.9$ ML (indicated by the vertical arrow). The experiment was approximated by the exponential function $\epsilon = \exp(-d/2.56)$, and the calculation was approximated by the hyperbolic function $[l_x/a][l_x^{(0)}/a^{(0)}] = [1 - \epsilon(d^{(0)})]/[1 - \epsilon(d)] = 0.971/d^{0.289}$.
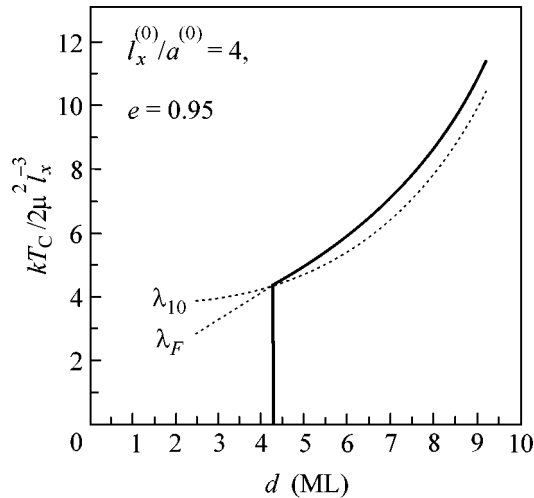

Fig. 5. Dependence of the Curie temperature $T_C(d)$ on the film effective thickness. The major axes of the grains are parallel to each other ($\theta = 0$), and the eccentricity is $e = 0.95$; parameters of the grain lattice: $\beta = 0.5$ and $l_x^{(0)}/a^{(0)} = 4$ [4].

follows from the STM images obtained in [2] that they are distributed within a rather narrow interval near $\theta = 0°$. As the film effective thickness increases, the grain size increases, while the lattice constants remain virtually constant (up to the intergrain contact). Hence, the ratio l_x/a decreases monotonically, resulting in the magnetic phase transition from the initial antiferromagnetic state to the ferromagnetic state. The critical film thickness d_c corresponding to this transition and the subsequent behavior of the Curie temperature T_c in the ferromagnetic state are determined, as was pointed out above, by the dipolar interaction parameter λ in different magnetic states of the system.

On the basis of the STM images obtained for the Co films in [2], it was assumed in our calculations that (1) the grain axes are parallel to each other ($\theta = 0$), (2) $\beta \equiv l_z/l_x = 0.5$, and (3) $l_x^{(0)}/a^{(0)} = 4$. The resulting $T_C(d) = \lambda(d)i_0/k$ dependence of the Curie temperature on the film effective thickness is shown in Fig. 5. For the chosen set of parameters, the transition of the grain system from the antiferromagnetic to the ferromagnetic state occurs at the critical thickness $d_c \approx 4.3$ ML, which is close to the corresponding value reported in [2]. As the critical thickness is achieved, the Curie temperature of the arisen ferromagnetic state becomes finite jumpwise and then increases with further film growth. The scale of the initial critical temperature is determined by the quantity μi_0, giving $T_C \sim 300$ K for $\mu = 300\mu_B$ and $i_0 = 10^{-4}$ Oe cm (this corresponds to a grain volume of 40 nm³ and grain concentration $N = 10^{-14}$ cm⁻²). This estimate agrees well with the results obtained in works [1], where a sharp rise in the Curie temperature to $T_c = 200–300$ K was experimentally observed for ultrathin Co films as their thicknesses achieved the critical value.

Thus, the model suggested properly predicts both the character of transition and its quantitative characteristics.

REFERENCES

1. W. Dürr, M. Taborelli, O. Paul, *et al.*, Phys. Rev. Lett. **62**, 206 (1989); C. M. Schneider, P. Dressler, P. Schuster, *et al.*, Phys. Rev. Lett. **64**, 1059 (1990); J. de la Figuera, J. E. Pietro, C. Okal, and R. Miranda, Phys. Rev. B **47**, 13043 (1993); A. K. Schmid, D. Atlan, H. Itoh, *et al.*, Phys. Rev. B **48**, 2855 (1993); F. Huang, M. T. Kief, G. J. Mankey, and R. F. Willis, Phys. Rev. B **49**, 3962 (1994); F. O. Shumann, M. E. Buckley, and J. A. C. Bland, Phys. Rev. B **50**, 16424 (1994); H. J. Elmers, J. Haushild, H. Höche, *et al.*, Phys. Rev. Lett. **73**, 898 (1994).

2. E. Gu, S. Hope, M. Tselepi, and J. A. C. Bland, Phys. Rev. B **60**, 4092 (1999).

3. E. Z. Meĭlikhov and R. M. Farzetdinova, Zh. Éksp. Teor. Fiz. **121** (4) (2002) (in press) [JETP **94** (2002) (in press)].

4. M. T. Kief and W. F. Egelhoff, Phys. Rev. B **47**, 10785 (1993).

Translated by V. Sakun

Resonance Scattering in Quantum Wells with Nanocenters

A. M. Satanin* and V. B. Shtenberg

Lobachevski State University, Nizhni Novgorod, 603600 Russia

*e-mail: satanin@phys.unn.runnet.ru

It is shown that, in 2D electron layers, nanocenters of finite radius (quantum dots, donors) may give rise to Fano resonances in the scattering cross section. The resonance contribution to the residual resistance is calculated. © 2002 MAIK "Nauka/Interperiodica".

PACS numbers: 73.21.Fg; 03.65.Ge

Interference phenomena closely related to asymmetric Fano resonances [1] have been widely studied, both theoretically and experimentally, in such processes as photoionization of atoms [2], electron and neutron scattering [3, 4], Raman scattering [5], and photoabsorption in quantum wells and superlattices [6–8]. Recently, Fano resonances were also observed in electron transport through a 1D quantum channel [9, 10]. The resonances can be considered as quantum "probes" that provide important information on the geometric relief and internal potential fields of low-dimensional structures. Therefore, the search for new effects related to the configuration interaction of different kinds of states in low-dimensional systems may be of interest.

In this paper, we study the Fano resonances in 2D systems and calculate their contribution to the residual resistance. As a model, we consider a quantum well with the states that interfere with nanocenters (e.g., with donor states of the δ layer or with quantum dot states). It is demonstrated that the states localized at the centers give rise to additional asymmetric peaks in the dependence of the resistance on the Fermi energy.

We assume that the states $\varphi_n(z)$ with the motion along the z axis (where the z axis is perpendicular to the 2D layer plane) and the corresponding energy levels E_n of electrons in an ideal quantum well of width W are known. Let an isolated quantum center be described by the function $V(x, y, z - Z_0)$, where Z_0 determines the position of the center with respect to the symmetry plane of the quantum well. The wave function can be represented as a series expansion in the complete basis of the functions $\varphi_n(z)$: $\Psi(x, y, z) = \sum_{n=1}^{\infty} \psi_n(x, y)\varphi_n(z)$.

Then, the Schrödinger equation yields

$$
-\frac{\hbar^2}{2m^*}\left(\frac{\partial^2}{\partial x^2} + \frac{\partial^2}{\partial y^2}\right)\psi_n(x, y)
$$
$$
+ \sum_{n'=1}^{\infty} V_{nn'}(x, y)\psi_{n'}(x, y) = (E - E_n)\psi_n(x, y), \tag{1}
$$

where

$$
V_{nn'}(x, y) = \int \varphi_n(z) V(x, y, z - Z_0)\varphi_{n'}(z)dz \tag{2}
$$

are the matrix elements of the center potential and m^* is the effective electron mass.

Assuming that the scattering center possesses a symmetry axis, we consider the electron states in the energy interval $E_1 < E < E_2$. The wave function in an open scattering channel can be represented as

$$
\psi_1(r, \theta) = e^{ik_1 r\cos\theta} + \frac{f(\theta)}{\sqrt{r}}e^{ik_1 r}, \tag{3}
$$

where $k_1 = \sqrt{2m^*(E - E_1)}/\hbar$ is the wave vector in the first zone and r and θ are the coordinates of the layer plane. We represent the wave functions in the form

$$
\psi_n(r, \theta) = \sum_{m=-\infty}^{\infty} e^{im\theta}\psi_{n,m}(r). \tag{4}
$$

From Eq. (1), we can derive equations for the amplitudes $\psi_{n,m}(r)$. The amplitude expansion coefficients $f(\theta)$ are expressed through the S matrix or through the scattering phases:

$$
f_m = \sqrt{\frac{2}{\pi k_1}}i^m e^{-i(\pi m/2 - \pi/4)}(S_m - 1), \tag{5}
$$
$$
S_m = e^{2i\delta_m} - 1,
$$

and the partial cross sections are determined by the expression

$$\sigma_m = \frac{\pi}{k_1}\sin^2(\delta_m). \qquad (6)$$

Using the approach described in [11], we express the residual resistance determined by the ensemble of quantum dots through the scattering phases:

$$\rho = \frac{n_i \hbar k_1}{e^2 n}\int_0^{2\pi}|f(\theta)|^2(1 - \cos\theta)$$

$$= \frac{2n_i \hbar}{e^2 n}\sum_{m=-\infty}^{\infty}\sin^2(\delta_m - \delta_{m+1}), \qquad (7)$$

where n_i is the 2D density of scatterers and n is the electron concentration.

If the electron energy is close to the group of levels in the potential well $V_{22}(r)$, it is precisely these bound states that will most strongly interfere with the incident wave. In the resonance approximation [12], we can retain only the terms that are closest in energy (the resonance terms) in the system of equations (1). In doing so, we take into account the arbitrary number of possible localized states in the field of the center. In other words, in Eq. (1) we retain the terms that contain $\psi_{1,m}$ and $\psi_{2,m}$:

$$\left(-\frac{\hbar^2}{2m^*}\frac{1}{r}\frac{\partial}{\partial r}r\frac{\partial}{\partial r} + V_{11,m}(r)\right)\psi_{1,m}(r)$$

$$+ V_{12}(r)\psi_{2,m}(r) = (E - E_1)\psi_{1,m}(r), \qquad (8)$$

$$\left(-\frac{\hbar^2}{2m^*}\frac{1}{r}\frac{\partial}{\partial r}r\frac{\partial}{\partial r} + V_{22,m}(r)\right)\psi_{2,m}(r)$$

$$+ V_{21}(r)\psi_{1,m}(r) = (E - E_2)\psi_{2,m}(r), \qquad (9)$$

where the diagonal matrix elements $V_{11,m}$ and $V_{22,m}$ involve the centrifugal energy. Note that we assume the matrix element V_{12}, which describes the coupling of the channels, to be small compared to the gap between the quantization subbands.

First, we construct the states for the potential scattering in the case of the 1D equation:

$$\left(-\frac{\hbar^2}{2m^*}\frac{1}{r}\frac{\partial}{\partial r}r\frac{\partial}{\partial r} + V_{11,m}(r)\right)\chi_m^{1,2}(r)$$

$$= (E - E_1)\chi_m^{1,2}(r). \qquad (10)$$

For a finite-radius potential, as linearly independent solutions we can choose the functions $\chi_m^{1,2}(r)$, which

have the following asymptotics at $r \longrightarrow +\infty$:

$$\chi_m^1(r) \longrightarrow \sqrt{\frac{2}{\pi k_1 r}}\cos\left(k_1 r - \frac{\pi m}{2} - \frac{\pi}{4} + \delta_m^p\right),$$

$$\chi_m^2(r) \longrightarrow \sqrt{\frac{2}{\pi k_1 r}}\sin\left(k_1 r + \frac{\pi m}{2} - \frac{\pi}{4} + \delta_m^p\right), \qquad (11)$$

where δ_m^p is the phase shift at the potential scattering. The formal solution to Eq. (8) can be represented in the form

$$\psi_{1,m}(r) = \chi_m^1(r) + \int_0^{\infty}dr'r'G_{1,m}(r,r')V_{12}(r')\psi_{2,m}(r'), \qquad (12)$$

where the Green function is expressed as

$$G_{1,m}^+(r,r') = \frac{\pi m^*}{\hbar^2}\begin{cases}\chi_m^1(r')\chi_m^2(r), & r > r', \\ \chi_m^1(r)\chi_m^2(r'), & r < r'.\end{cases} \qquad (13)$$

Now, we consider Eq. (9). If we ignore the term with V_{21} in Eq. (9), the latter will take the form of a 1D Schrödinger equation. Depending on the parameters of the attracting well $V_{22}(r)$, in the effective potential $V_{22,m}(r)$ at some energy values $\mathcal{E}_{j,m}$, the existence of bound states $u_{j,m}$ ($j = 1, \ldots, N$) and continuous spectrum states $u_{\nu,m}(r)$ is possible. Taking into account the localized states and the continuous spectrum states, we write the solution to Eq. (8) in the form

$$\psi_{2,m}(r) = \sum_{\lambda}A_{\lambda,m}u_{\lambda,m}(r), \qquad (14)$$

where $A_{\lambda,m} = (A_{j,m}, A_{\nu,m})$ are arbitrary (as yet) amplitudes, $\lambda = (j, \nu)$ is a complete set of quantum numbers, and $u_{\lambda,m} = (u_{j,m}, u_{\nu,m})$.

Substituting Eqs. (12) and (14) in Eq. (9) and taking into account the orthogonality of the states $u_{\lambda,m}(x)$, we obtain an equation for the determination of the amplitudes $A_{\lambda,m}$:

$$(E - \mathcal{E}_{\lambda,m})A_{\lambda,m} - \sum_{\lambda'}U_{\lambda,\lambda';m}A_{\lambda',m} = F_{\lambda,m}, \qquad (15)$$

where

$$U_{\lambda,\lambda';m} = \int_0^{\infty}dr\,r\int_0^{\infty}dr'\,r'u_{\lambda,m}(r)$$

$$\times V_{12}(r)G_{1,m}(r,r')V_{21}(r')u_{\lambda',m}(r'), \qquad (16)$$

$$F_{\lambda,m} = \int_0^{\infty}dr\,r\,u_{\lambda,m}(r)V_{12}(r)\chi_m^1(r).$$

In its turn, the function $\psi_{1,m}$ is obtained from Eq. (12) by substituting $\psi_{2,m}$, determined by Eq. (14), on the
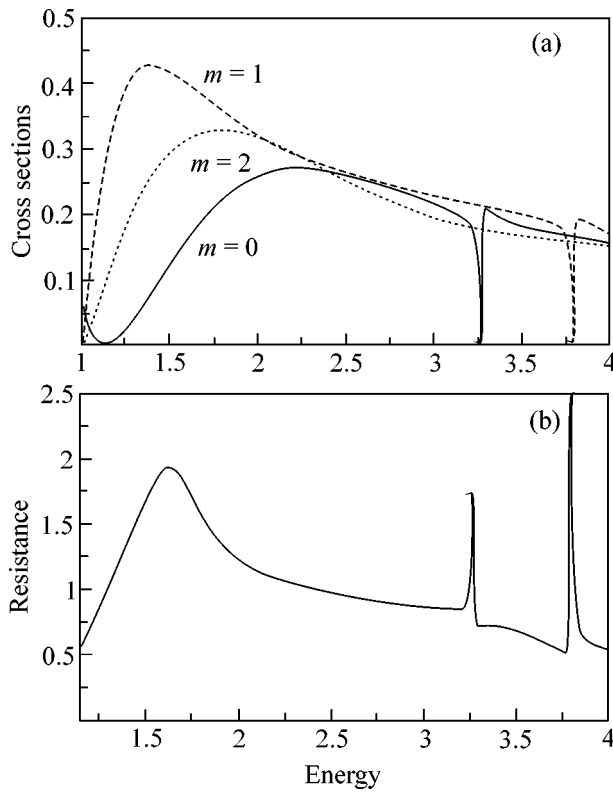
Fig. 1. (a) Partial cross sections with $m = 0, 1, 2$ and (b) the resistance of the system versus the electron energy. The Fano resonances can be seen at $\mathscr{E}_{R,0} = 3.3113E_1$ ($m = 0$) and $\mathscr{E}_{R,1} = 3.7602E_1$ ($m = 1$). The units of measurement for the cross sections, the resistance, and the energy are $\sigma_0 = W$, $\rho_0 = 2\hbar n_i/e^2 n$, and $E_1 = \pi^2\hbar^2/2m^*W^2$, respectively.

right-hand side of Eq. (12):

$$\psi_{1,m}(r) = \chi_m^1(r)$$
$$+ \sum_\lambda \left(\int_0^\infty dr' r' G_{1,m}(r, r') V_{12}(r') u_{\lambda,m}(r') \right) A_{\lambda,m}. \quad (17)$$

Consider the asymptotics of the wave function $\psi_{1,m}(r)$ at $r \longrightarrow +\infty$. With allowance for Eqs. (11) and (13), from Eq. (17), we obtain

$$\psi_{1,m}(r) = \sqrt{\frac{2}{\pi k_1 r}} \left(\cos\left(k_1 r - \frac{\pi m}{2} - \frac{\pi}{4} + \delta_m^p\right) \right.$$
$$\left. + \tan\delta_m^f \sin\left(k_1 r - \frac{\pi m}{2} - \frac{\pi}{4} + \delta_m^p\right) \right), \quad (18)$$

where δ_m^f is the additional phase shift determined by the expression

$$\tan\delta_m^f = \frac{\pi m^*}{\hbar^2} \sum_\lambda F_{\lambda,m} A_{\lambda,m}. \quad (19)$$

Thus, the scattering phases caused by interference can be found from Eqs. (15) and (19). Note that the scattering characteristics depend on the total phase $\delta_m = \delta_m^p + \delta_m^f$.

The partial cross section is determined by the states with a given moment projection m. If the center has a characteristic size $\sim R$ in the radial direction, a noticeable contribution to the potential phase shift and partial scattering cross section is made by the states with $m \sim k_1 R$. Then, in the field of the potential $V_{11,m}(r)$, Breit–Wigner resonances may occur due to the interference of radial waves propagating in opposite directions. The discrete levels in the well $V_{22,m}(r)$ give rise to additional resonances, which are determined by the phase shift δ_m^f. Let us consider the behavior of the phase near an isolated level. In this case, we have

$$\tan\delta_m^f = \frac{\pi m^*}{\hbar^2} \frac{F_{1,m}^2}{E - \mathscr{E}_{1,m} - U_{1,1;m}}. \quad (20)$$

One can easily show that, near the given level, the functions $F_{1,m}$ and $U_{1,1;m}$ slowly vary with energy and they can be considered as approximately constant. Then, we can write the following expressions:

$$\tan\delta_m^t = \frac{\Gamma_m^f}{E - \mathscr{E}_{R,m}}, \quad \Gamma_m^f = \frac{\pi m^*}{\hbar^2} F_{1,m}^2,$$
$$\mathscr{E}_{R,m} = \mathscr{E}_{1,m} - U_{1,1;m}. \quad (21)$$

Hence, the behavior of the partial cross sections near the resonance can be described by the formula

$$\sigma_m = \frac{\pi}{k_1} \sin^2(\delta_m^p) \frac{(\epsilon + q_m)^2}{\epsilon^2 + 1}, \quad (22)$$

where $\epsilon = (E - \mathscr{E}_{R,m})/\Gamma_m^f$ and $q_m = \cot\delta_m^p$. As one can see from Eq. (22), near the now virtual level, asymmetric Fano resonances arise in the scattering cross section [1]. Note that, both the width and the shift of the initial position of the level depend on the configuration interaction of the discrete level with the continuum.

As an illustration, we present the results obtained by calculating the partial cross sections and the resistance for the case of centers modeled by potential wells with cylindrical shape (with the depth V_0, the height W_a and the radius R). The solutions to the equations inside and outside the center can be expressed through the Bessel functions for both bound and scattering states. Thus, for the problem under consideration, one can easily determine the phases of the potential scattering and the discrete levels and derive an explicit expression for the matrix elements involved in Eq. (15). The numerical solution of the system of linear equations (15) is performed in a standard way. We present the results of such calculations for the simplest case. We assume that, in a quantum well of width W, identical quantum dots exist

at the distance $Z_0 = 0.1W$ from the well symmetry plane ($z = W/2$) and their size is $W_a = 0.4W$. Let the depth of the initial well be such that the conditions $V_{11} = 1.515E_1$, $V_{12} = 0.521E_1$, and $V_{22} = 1.0E_1$ are satisfied. As the energy unit, we choose $E_1 = \pi^2/2m^*W^2$. If the radius of the center is $R = W$, two levels can exist in the field of the center: with $m = 0$, $\mathcal{E}_{1,0} = 3.326E_1$, and with $m = 1$, $\mathcal{E}_{1,1} = 3.777E_1$. As one can see from Fig. 1a, each level gives rise to Fano resonances in the partial cross sections at $\mathcal{E}_{R,0} = 3.3113E_1$ ($m = 0$) and $\mathcal{E}_{R,1} = 3.7602E_1$ ($m = 1$); the resonance widths are $0.0064E_1$ and $0.0059E_1$, respectively. Other partial cross sections monotonically vary with energy in the energy interval under consideration. Note that, for the energy close to the bottom of the band with $n = 1$, a Breit–Wigner resonance is observed ($\mathcal{E}_{BW,3} = 1.51E_1$ with $m = 3$; its width is $0.42E_1$).

Each Fano resonance makes a contribution to the resistance in the form of additional characteristic profiles (Fig. 1b shows two resonance peaks near the separated levels). Since the contribution to the resistance is determined by the transport scattering cross section, it consists of two components: $\int_0^{2\pi} d\theta |f(\theta)|^2$ – $\int_0^{2\pi} d\theta |f(\theta)|^2 \cos\theta$. The behavior of each component near the Fano resonance is similar to that in the case of partial cross sections. However, the minimum in the cross section difference corresponds to the maximum in the resistance and vice versa; i.e., in the residual resistance, inverted (with respect to the partial cross sections) Fano resonances must be observed.

When the parameters of the center are such that the center contains several levels (resonances), new effects caused by the interference of waves near the center become possible. For example, an intersection of Breit–Wigner resonances with Fano resonances may occur, which will lead to a collapse of the Fano resonances. In this case, the Fano resonance swing may take place with the change from the zero–pole sequence to the pole–zero one. The effects indicated above are similar to the effects that occur in a quasi-one-dimensional system [13].

Thus, nanocenters of finite size give rise to a series of quasi-localized states, which manifest themselves as resonance–antiresonance pairs in the scattering cross sections and in the resistance. The characteristics of the Fano resonances determine the magnitude of the configuration coupling of the states in a nanostructure. The resonance contribution to the resistance can be revealed, e.g., by the dependence of the resistance on the position of the Fermi level.

REFERENCES

1. U. Fano, Phys. Rev. **104**, 1866 (1961).
2. U. Fano and J. W. Cooper, Phys. Rev. A **137**, 1364 (1965).
3. R. K. Adair, C. K. Bockelman, and R. E. Peterson, Phys. Rev. **76**, 308 (1949).
4. J. A. Simpson and U. Fano, Phys. Rev. Lett. **11**, 158 (1963).
5. F. Cardeira, T. A. Fjeldly, and M. Cardona, Phys. Rev. B **8**, 4734 (1973).
6. J. Feist, F. Capasso, C. Sirtori, *et al.*, Nature (London) **390**, 589 (1997).
7. H. Schmidt, K. L. Campman, A. C. Gossard, and A. Imamoglu, Appl. Phys. Lett. **70**, 3455 (1997).
8. C. P. Holfeld, F. Löser, M. Sudzius, *et al.*, Phys. Rev. Lett. **81**, 874 (1998).
9. J. Göres, D. Goldhaber-Gordon, S. Heemeyer, *et al.*, Phys. Rev. B **62**, 2188 (2000).
10. O. A. Tkachenko, V. A. Tkachenko, D. G. Baksheev, *et al.*, Pis'ma Zh. Éksp. Teor. Fiz. **71**, 366 (2000) [JETP Lett. **71**, 255 (2000)].
11. C. Kittel, *Quantum Theory of Solids* (Wiley, New York, 1963; Nauka, Moscow, 1967).
12. H. Feshbach, Ann. Phys. **5**, 357 (1958).
13. C. S. Kim, A. M. Satanin, Y. S. Joe, and R. M. Cosby, Phys. Rev. B **60**, 10962 (1999).

Translated by E. Golyamina

Spontaneous Breaking of Molecular Identity and Phase Diagrams of Thermally Reversible Association Systems with Alternating Molecules

I. Ya. Erukhimovich and M. V. Tamm*

Moscow State University, Vorob'evy gory, Moscow, 119899 Russia

Nesmeyanov Institute of Organoelement Compounds, Russian Academy of Sciences,
ul. Vavilova 28, Moscow, GSP-1, 117813 Russia

* e-mail: ierukhs@polly.phys.msu.su

Received January 4, 2002

The global phase behavior of a mixture of molecules A_f and B_f, each containing f functional groups of, respectively, types A and B capable of forming thermally reversible chemical bonds, is considered. Contrary to the traditional approach based on the consideration of an infinite cluster of labile bonds that appears in such systems on the Bethe lattice (i.e., in the Cayley tree approximation) under certain conditions, we additionally take into account the contribution to the thermodynamics from the cluster fragments forming mesoscopic cycles. It is shown, within the framework of the suggested mesoscopic cyclization approximation, which is based on the concept of spontaneous breaking of molecular identity upon the formation of an infinite cluster, that this contribution is finite. Phase diagrams are constructed for the systems considered. The presence of a point of equal concentrations, where two liquid phases coexist and one of them contains an infinite cluster of thermally reversible bonds, is the specific feature of the phase diagrams in the approximation suggested. © *2002 MAIK "Nauka/Interperiodica"*.

PACS numbers: 82.30.Nr; 05.70.Fh; 64.70.Ja

The statistical description of molecular systems capable of forming thermally reversible intermolecular chemical bonds is of great interest primarily in the context of the theory of fluids. It is precisely the association solutions that often exhibit the nontrivial phase behavior such as a decrease in solubility upon an increase in temperature. This manifests itself in the appearance of lower critical points of solubility and high-temperature insolubility corridors or closed loops [1]. In this connection, of particular interest is the description of the contribution to the thermodynamics from an infinite cluster (IC) of labile bonds (gel) that appears under certain conditions in the association solutions.

In most works on the thermodynamics of association systems, free energy of the latter in the postgel region is taken as an analytic continuation of the free energy of a system of finite tree-like clusters (sol fraction) [2–8]. In other words, the description of IC on the Bethe lattice is assumed to be adequate in the mean-field approximation [9]. In [10], we proposed a basically different approach [mesoscopic cyclization (MC) approximation] and refined it in [11, 12]. This approach is based on the obvious fact that the tree-like IC cannot be put in a real finite-dimensional space without forming cycles by a finite fraction of bonds. If the number of monomers, to which each monomer can be bonded, is large enough, then the size of these cycles is also large

compared to the bond length. For this reason, these (mesoscopic) cycles show up as trees on small (compared to the cycle size) scales. However, the combinatorial analyses of the tree-like fragments and of the fragments forming mesoscopic cycles are different (this fact is ignored in the classical approach ordinarily ascribed to Flory [13]). In the MC approximation, which generalizes the mean-field approximation to the case of IC with mesoscopic cycles, we take this distinction into account by ascribing different symmetry indices to the monomers belonging to different structural fragments of IC. Then, the thermodynamically equilibrium IC structure is found by minimizing the free energy as a function of the densities of monomers in the structurally different fragments (this method of calculating the free energy of association systems has much in common with the calculation of the contribution from the high-order diagrams to the Gell-Mann–Low function [14]).

The thermodynamically equilibrium fraction of cycle-forming monomers becomes finite simultaneously with the IC formation in association systems composed of molecules A_f, whose any two A groups can form thermally reversible chemical bonds A–A [10–12]. Therefore, in the MC approximation, the appearance of IC is nothing but the phase transition accompa-

nied by spontaneous breaking of monomer identity. An important experimentally observed consequence of the MC approximation is that the phase diagrams of such systems may contain points corresponding to a pure substance and triple points characteristic of the liquid–solid phase equilibrium [15]. As for the Flory approach, it allows only the critical points corresponding to the liquid–liquid phase equilibrium [15].

In this work, we demonstrate that the spontaneous breaking of monomer identity upon the IC formation can occur in one more class of association systems and lead to phase diagrams containing points of equal concentrations [16].

Let us consider an association system of clusters consisting of molecules of two types A_f and B_f, each bearing f functional groups of, respectively, types A and B capable of forming thermally reversible bonds:

$$A + B \xrightleftharpoons[k(T)] AB, \qquad (1)$$
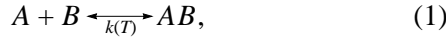
where $k(T)$ is the temperature-dependent equilibrium constant for the corresponding reaction.

In the mean-field approximation, the free energy of this system is the sum of the energetic contribution to the free energy of a nonassociation mixture and the structural (caused by association) contribution,

$$F = F^* + F_{str}. \qquad (2)$$

In the simplest case, the first term in Eq. (2) can be written as

$$F^* = N\theta\phi_A\phi_B/2, \qquad (3)$$

where θ is the characteristic van der Waals interaction energy of molecules, N is the total number of molecules, and $\phi_{A,B}$ are the volume fractions of components satisfying the incompressibility condition

$$\phi_A + \phi_B = 1. \qquad (4)$$

By analogy with [12], the second term can be represented as

$$F_{str}(\phi_A, \phi_B, N, T) = NT\min_{\{\phi_C\}}\tilde{F}(\phi_A, \phi_B, \phi_C, \kappa), \qquad (5)$$

where $\kappa = k/v$ is the equilibrium constant (normalized to the molecular volume) for the bond-formation reaction (1) and $\tilde{F}(\phi_A, \phi_B, \phi_C, \kappa)$ is the free energy of a system for which the monomer association is the only interaction and which is in the partial equilibrium state with a given total volume fraction ϕ_C of all AB bonds involved in the cyclic fragments. As in [11, 12], this

free energy can be written in the form

$$\tilde{F}(\phi_A, \phi_B, \phi_C, \kappa)$$
$$= \min\left\{\sum_{\substack{S=A,B}}\sum_{\substack{0 \le i+j \le f, \\ j \ne 1}} \phi_{i,j}^S \ln(i!j!(f-i-j)!\phi_{i,j}^S/e)\right.$$
$$\left. - \phi_T\ln(\kappa\phi_T/e) - \phi_C\ln(\kappa\phi_C/e)\right\}, \qquad (6)$$

where $\phi_{i,j}^S$ is the volume fraction of molecules S_f whose i and j functional groups underwent a reaction to form tree-like and cyclic fragments, respectively; and ϕ_T is the total volume fraction of the bonds involved in the tree-like fragments. The first term in the braces in Eq. (6) corresponds to the translational entropy of molecules (with account taken of the above-mentioned distinctions in the symmetry coefficients and the fact that the monomer cannot be involved in the cyclic fragment through the formation of less than two bonds), and the last two terms correspond to the free energy of formation of the AB bonds [12] for the groups involved in the tree-like and cyclic fragments, respectively. By minimizing Eq. (6) with respect to the $\{\phi_{i,j}^S\}$ and ϕ_T variables and taking into account the conservation laws

$$\sum_{\substack{0 \le i+j \le f \\ j \ne 1}} \phi_{i,j}^S = \phi_S, \qquad \sum_{\substack{0 \le i+j \le f \\ j \ne 1}} j\phi_{i,j}^S = \phi_C,$$
$$\sum_{\substack{0 \le i+j \le f \\ j \ne 1}} i\phi_{i,j}^S = \phi_T, \quad S = A, B, \qquad (7)$$

one obtains the following expression for the structural free energy:

$$\tilde{F}(\phi_A, \phi_B, \phi_C, \kappa) = \phi_A\mu_A + \phi_B\mu_B + \phi_C(\mu_A^C + \mu_B^C)$$
$$+ T(\phi_T - \phi_A - \phi_B - \phi_C\ln(\kappa\phi_C/e)). \qquad (8)$$

In this expression, the chemical potentials (Lagrange multipliers) μ_S, μ_S^T, and μ_S^C corresponding to conditions (7), the activities $\Phi_S = \exp(\mu_S^T/T)$ and $\Psi_S = \exp(\mu_S^C/T)$, and the density ϕ_T are given by the relations

$$\mu_S = T\ln(f!\phi_S/A_f(\delta_S)) - f\ln(1 + \Phi_S), \qquad (9a)$$

$$\phi_C = f\phi_A[1 - A_{f-1}(\delta_A)/A_f(\delta_A)]$$
$$= f\phi_B[1 - A_{f-1}(\delta_B)/A_f(\delta_B)]; \qquad (9b)$$

$$\delta_S = \Psi_S/(1 + \Phi_S), \qquad (9c)$$
$$\kappa\phi_T = \Phi_A\Phi_B,$$

$$\kappa(f\phi_A - \phi_C) = \phi_B + \Phi_A\Phi_B;$$
$$\kappa(f\phi_B - \phi_C) = \Phi_A + \Phi_A\Phi_B, \tag{9d}$$

where $A_f(x) = (1+x)^f - fx$ (an unusual form of the function A_f follows from the above-mentioned fact that the monomers cannot be involved in the cycle through the formation of only a single bond).

The function $\tilde{F}(\phi_A, \phi_B, \phi_C, \kappa)$ can reach its extremum either at the edge of the interval of physical values of ϕ_C, i.e., at $\phi_C = 0$, or at ϕ_C satisfying equation

$$\kappa\phi_C = \Psi_A\Psi_B, \tag{9e}$$

where $\Psi_S(\phi_A, \phi_B, \phi_C)$ is determined by Eqs. (9b) and (9d).

In the case of the Bethe lattice (Flory approximation), the cycles are absent $(\phi_{i,j}^S\big|_{j\neq 0}^S = \phi_C = 0)$ and Eq. (8) takes the form

$$F_{str}^{Fl} = NT \sum_{S=A,B} \{\phi_S\ln(f!\phi_S/e)$$
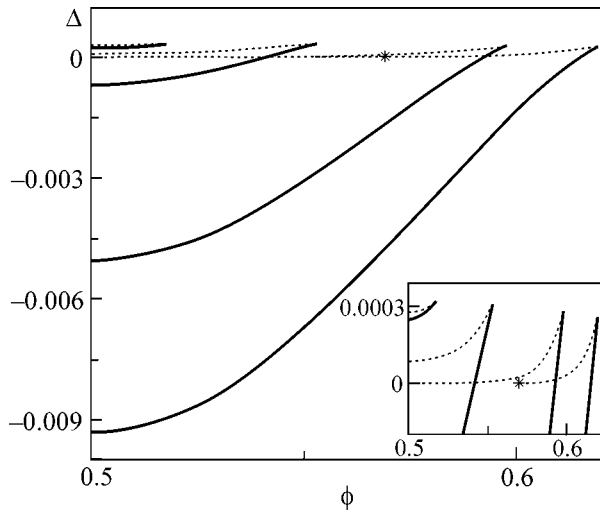$$+ f(\phi_S\ln(1-\Gamma_S) - (\phi_S\Gamma_S/2))\}, \tag{10}$$

Fig. 1. The $\Delta(\phi_A)$ function for $f = 3$ and different κ values.
The dotted lines correspond to the maxima of F_{str}^{MC} (absolutely unstable barrier tops between the phases). The region of small Δ is given in the inset on a larger scale. At $\kappa = 1.21$ (curve 1), the MC gel can only be metastable ($F_{MC} > F_{Fl}$) in a narrow region near $\phi = 0.5$. The region of thermodynamically stable MC gel appears at $\kappa = 1.24$ (curve 2). Curve 3 [$\kappa = \kappa_F(0.5) = 4/3$] corresponds to the classical gel point at $\phi = 0.5$. The region near $\phi = 0.5$, where the tree-like IC is absolutely unstable against an increase in the fraction ϕ_C of bonds involved in the cycle-forming fragments, appears at $\kappa = 1.4 > \kappa_F(0.5)$ (curve 4). The boundary of this region is indicated by an asterisk.

where $\Gamma_S = \phi_T/f\phi_S = \Phi_S/(1 + \Phi_S)$ ($S = A, B$) are related to ϕ_S by the mass action law:

$$f\kappa\phi_A = \Gamma_B/(1 - \Gamma_A)(1 - \Gamma_B);$$
$$f\kappa\phi_B = \Gamma_A/(1 - \Gamma_B)(1 - \Gamma_A). \tag{11}$$

At $\phi_C \neq 0$, the minimum value of function $\tilde{F}(\phi_A, \phi_B, \phi_C, \kappa)$ is equal to

$$F_{str}^{MC}(\phi_A, \phi_B, \phi_C, \kappa)$$
$$= \phi_A\mu_A + \phi_B\mu_B + T(\phi_T + \phi_C - \phi_A - \phi_B), \tag{12}$$

where μ_C, ϕ_T, and ϕ_C are given by Eqs. (9).

The direct calculation shows that, under the condition

$$\kappa > \kappa_F(\phi_A, \phi_B) = 2((f-1)/f)$$
$$\times (\sqrt{(1 - (\phi_A - \phi_B)^2)}[1 + (f-1)^2] - 2(f-1))^{-1}, \tag{13}$$

corresponding to the formation of an infinite tree-like cluster in the Flory approximation, the point $\phi_C = 0$ is not even the point of a local minimum of the function $\tilde{F}(\phi_A, \phi_B, \phi_C, \kappa)$. In other words, the classical (on the Bethe lattice) solution the (10) and (11) corresponding to the zero volume fraction ϕ_C of the bonds forming mesoscopic cycles is absolutely unstable against the increase in ϕ_C in the gel phase.

As for the interval $\kappa_1 \approx 0.9k_F < \kappa < \kappa_F$, the free energy $\tilde{F}(\phi_A, \phi_B, \phi_C, \kappa)$ has two minima in it. This signifies that two thermodynamically stable (or metastable) states occur in this interval: sol phase and gel phase with mesoscopic cyclization described, respectively, by Eqs. (9), (12) and (10), (11). The first-order phase transition between these states (for a given ϕ_A) occurs as the association constant increases to a certain value $\kappa = \kappa_{tr}(f, \phi_A)$, which depends only slightly on f and strongly on ϕ_A and reaches its minimum at $\phi_A = 0.5$, where, hence, the gel phase appears for the first time upon increasing κ. The numerical solution of the equation

$$F_{str}^{Fl}(\kappa_{tr}, \phi_A = \phi_B = 0.5)$$
$$= F_{str}^{MC}(\kappa_{tr}, \phi_A = \phi_B = 0.5) \tag{14}$$

yields, e.g., for $f = 3$, $\kappa_{tr} \approx 1.2195$, $\delta_{A,B}^{tr} \approx 0.1844$, and $\Gamma_{A,B}^{tr} \approx 0.4851$.

A quantitative estimate of the correction to the structural free energy caused by the mesoscopic cyclization is given in Fig. 1, where the concentration dependences are shown for the differences $\Delta = F_{str}^{MC} - F_{str}^{Fl}$ between the extremums of the structural free energy calculated by Eqs. (10) and (11) for different association constants κ with allowance for the incompressibility condition (4).
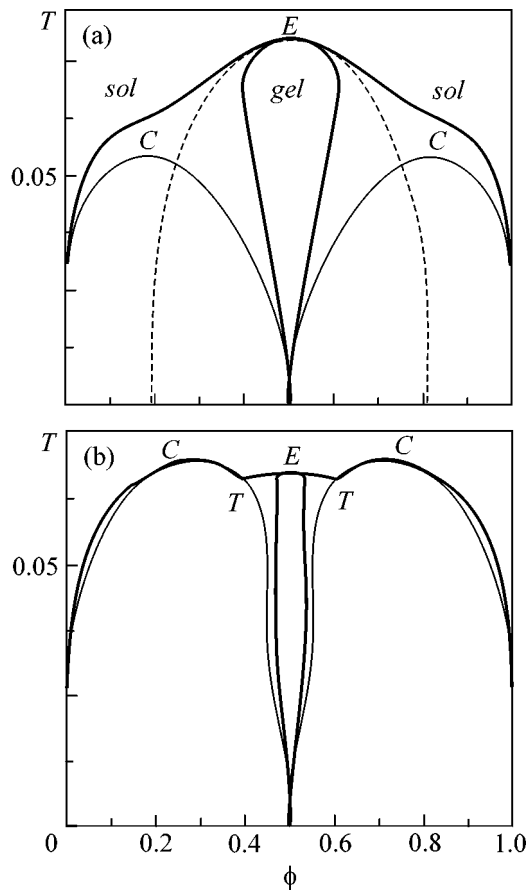
Fig. 2. Typical phase diagrams for $f = 3$. The heavy lines correspond to the phase equilibrium curves in the MC approximation, and the thin lines correspond to the Flory approximation. Letters E, C, and T indicate the points of equal concentrations, the critical points, and the triple points, respectively. (a) $\ln \kappa_0 = -2$ and $E = -0.175$. The dotted line corresponds to the sol–gel transition curve. It is seen that the Flory's critical points correspond to the sol phase, and, hence, they can be metastable also in the MC approximation. (b) $\ln \kappa_0 = -2.02$ and $E = -0.15$.

A variation in temperature generally results in the phase separation into two phases of different composition, whose equilibrium is governed by the temperature dependence of κ. When constructing the corresponding phase diagrams, it is natural to express energy and temperature in units θ and take κ in the simplest Arrhenius form $\kappa = \kappa_0 \ln(-E/T)$. In this case, the phase behavior of the system is governed solely by the parameters κ_0 and E.

Two typical phase diagrams of the systems considered are presented in Fig. 2. One can see that the stability of these systems against phase layering increases in the region of compositions close to their stoichiometric values ($\phi_A = \phi_B = 0.5$) [17], regardless of the chosen approximation. Nevertheless, specific to the MC approximation (compared to the Flory approximation) is the presence of a point of equal concentrations, which may be accompanied both by the disappearance
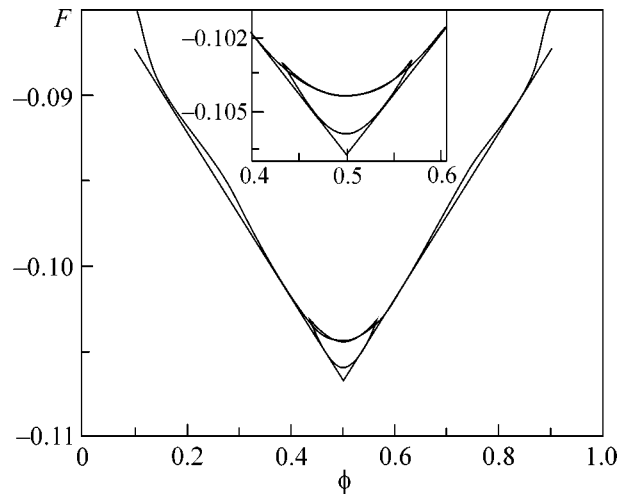

Fig. 3. Free energy as a function of volume fraction ϕ_A at $T = T_3$, where T_3 is the temperature of triple points in the phase diagram shown in Fig. 2b ($\kappa = 1.2628$ and $T = 0.06657$). The straight lines are the common tangents to the graph of free energy. The region near the stoichiometric relation $\phi_A = \phi_B = 0.5$ between the components is shown in the inset on a larger scale.

of a pair of critical points appearing in the Flory approximation (more precisely, by their transformation into the metastable points; see Fig. 2a) and by the appearance of an additional pair of triple points lying between the point of equal concentrations and the critical points (Fig. 2b).

One can clearly see in Fig. 3, where the concentration dependence of the total free energy (2) is shown for the temperature corresponding to the triple point in Fig. 2b, that the point of equal concentrations appears due to the presence of a knee in the $F(\phi_A)$ curve at the compositions satisfying the equation

$$F_{str}^{Fl}(\kappa_{tr}, \phi_A, 1 - \phi_A) = F_{str}^{MC}(\kappa_{tr}, \phi_A, 1 - \phi_A).$$

In turn, the knee at the points, where the global minimum of the structural free energy moves from the tree-like sol-phase state to the gel-phase state with mesoscopic cyclization, is caused by the presence of an order parameter characterizing different partial equilibrium states that can appear at a given temperature and composition of the system. It is conceivable that this mechanism also generates points of equal concentrations in traditional phase diagrams describing thermodynamic equilibrium between the liquid and solid phases, where the role of the order parameter is played by the amplitude of spatially inhomogeneous distribution of a composition with the symmetry of one or another spatial lattice. As demonstrated above, such a situation can also occur in the case of equilibrium between two liquid phases in the systems with alternating associating particles, where the fraction of particles involved in the fragments forming mesoscopic cycles in an IC of labile

bonds serves as an order parameter, while the monomer identity is the broken symmetry.

A complete classification of the phase diagrams for arbitrary values of κ_0 and E will be given elsewhere.

REFERENCES

1. M. M. Coleman, J. E. Graf, and P. C. Painter, *Specific Interactions and the Miscibility of Polymer Blends* (Technomic Publ., Lancaster, 1991).

2. J. C. Wheeler, J. Chem. Phys. **62**, 433 (1975).

3. A. Coniglio, H. F. Stanley, and W. Klein, Phys. Rev. Lett. **42**, 518 (1979).

4. A. Coniglio, H. F. Stanley, and W. Klein, Phys. Rev. B **25**, 6805 (1982).

5. I. Ya. Erukhimovich, Candidate's Dissertation (Moscow, 1979).

6. B. A. Veitsman, J. Phys. Chem. **94**, 8499 (1990).

7. C. Panayiotou and I. C. Sanchez, J. Phys. Chem. **95**, 10090 (1991).

8. A. N. Semenov and M. Rubinstein, Macromolecules **31**, 1373 (1998).

9. P. D. Gujrati and D. Bowman, J. Chem. Phys. **111**, 8151 (1999).

10. I. Ya. Erukhimovich, Zh. Éksp. Teor. Fiz. **108**, 1004 (1995) [JETP **81**, 553 (1995)].

11. I. Ya. Erukhimovich and A. V. Ermoshkin, Zh. Éksp. Teor. Fiz. **115**, 979 (1999) [JETP **88**, 538 (1999)].

12. I. Ya. Erukhimovich, M. V. Thamm, and A. V. Ermoshkin, Macromolecules **34**, 5653 (2001).

13. P. J. Flory, *Principles of Polymer Chemistry* (Cornell Univ. Press, Ithaca, 1953).

14. L. N. Lipatov, Zh. Éksp. Teor. Fiz. **71**, 1634 (1976) [Sov. Phys. JETP **44**, 855 (1976)].

15. I. Ya. Erukhimovich and A. V. Ermoshkin, J. Chem. Phys. **116**, 368 (2002).

16. L. D. Landau and E. M. Lifshitz, *Course of Theoretical Physics*, Vol. 5: *Statistical Physics* (Nauka, Moscow, 1995; Pergamon, Oxford, 1980), Part 1.

17. F. Tanaka and M. Ishida, Physica A (Amsterdam) **204**, 660 (1994).

Translated by V. Sakun

New Mechanism of Impurity Conduction in Lightly Doped Crystalline Noncompensated Silicon

A. P. Mel'nikov[1]*, Yu. A. Gurvich[1], S. A. Shevchenko[2], L. N. Shestakov[3], and L. I. Men'shikov[4]

[1] *Moscow State Pedagogical University, Moscow, 119891 Russia*
[2] *Institute of Solid-State Physics, Russian Academy of Sciences, Chernogolovka, Moscow region, 142432 Russia*
[3] *Seaside State University, Arkhangel'sk, 163006 Russia*
[4] *Russian Research Centre Kurchatov Institute, pl. Kurchatova 1, Moscow, 123182 Russia*
*e-mail: melnikov@rpl.mpgu.msk.su
Received January 9, 2002

It is found that the plastic deformation of lightly doped crystalline silicon samples ($N < 6 \times 10^{16}$ cm^{-3}) with a low compensation ($K \sim 3 \times 10^{-2}$) gives rise to nonohmic conduction σ_M in electric fields that differs radically from conventional hopping conduction via the ground states of impurities (σ_3). The values of σ_M can exceed values of σ_3 by a factor of 10^3–10^5. The value of σ_M and its dependence on the electric (E) and magnetic (H) fields can be controlled by varying the density of dislocations and the mode of thermal sample treatment. A strong anisotropy of σ_M is observed in samples with oriented dislocations: the conductivities along and across dislocations can differ by a factor of 10^4. The results are explained by the occurrence of conduction via the H^--like states of impurities concentrated in the vicinity of dislocations. The levels of these states lie between the upper and the lower impurity Hubbard bands. © 2002 MAIK "Nauka/Interperiodica".

PACS numbers: 72.20.-i; 72.80.Cw; 71.55.Cn

The static impurity conductivity in doped crystalline semiconductors (σ) is commonly interpreted as a sum of conductivities via the ground states of impurities (σ_3) and via the H^--like states (σ_2) of the upper and the lower impurity Hubbard bands, respectively. The latter type of conductivity is observed at low compensation degrees (K) within a narrow range of concentrations of the major impurity (N) close to the Mott transition [1] (for shallow impurities in silicon, $N \sim 4 \times 10^{18}$ cm^{-3}).

Complex studies of impurity conduction were performed in [2–7] at temperatures $T < 15$ K in silicon crystals lightly doped with boron ($10^{16} < N < 10^{17}$ cm^{-3}) with low compensation rates $K < 10^{-3}$. It was originally found that nonohmic conductivity σ_M emerges when the electric field strength is increased up to values $E > E^* = f(K, T) \sim 20$–$200$ V/cm. Its dependences on N, K, H, and T differ radically from those expected for the conductivity σ_3 [8]. The conductivity σ_M sharply increases with increasing E and can exceed the conductivity σ_3 by several orders of magnitude; σ_M decreases with increasing K ($\sigma_M \sim K^{-n}$, $n > 1$) and N ($-\ln \sigma_M \sim N^{-1/3}$) and is characterized by a high magnetoresistance. Note that the level via which this conductivity is effected (ε_{tr}) is separated by 10–15 meV from the empty band bottom [4]; that is, it lies between the energies of the boron ground state ($\varepsilon_0 \sim -45$ meV) and the H^--like state ($\varepsilon^- \sim -2$ meV). The main question that

arises in connection with the σ_M conductivity is that of the nature of the states lying very deep in the Mott–Hubbard gap.

When studying the σ_M conductivity, we came up against the fact that samples almost identical in their parameters can strongly differ in the values of E^* and σ_M. This fact, as well as a number of other considerations, led us to the hypothesis that the σ_M conductivity is associated with defects of the crystal structure, presumably, with dislocations. In order to check this hypothesis, we studied the effect of high-temperature annealing and plastic deformations on the $\sigma(E)$ relationships.

As an example, Fig. 1 demonstrates $\sigma(E)$ curves obtained at $T = 8$ K for a Si : B sample grown by crucibleless zone melting (CZM) with $N = 3.5 \times 10^{16}$ cm^{-3}, $K \sim 3 \times 10^{-5}$, and the density of growth dislocations $N_D \sim 10^4$ cm^{-2} obtained using various annealing modes. Ohmic contacts were coated by spark alloying of aluminum. During alloying, the sample was locally heated up to $t > 1000°$C and then was cooled down to room temperature within approximately 3 min. The flat section in Fig. 1 (curve *1*) corresponds to the σ_3 conductivity, and the region of sharp growth at $E > E^* \sim 120$ V/cm corresponds to the σ_M conductivity. After that, the sample was heated up to $t = 700°$C, was held at this temperature for 2 h, and was slowly (for 3 h) cooled

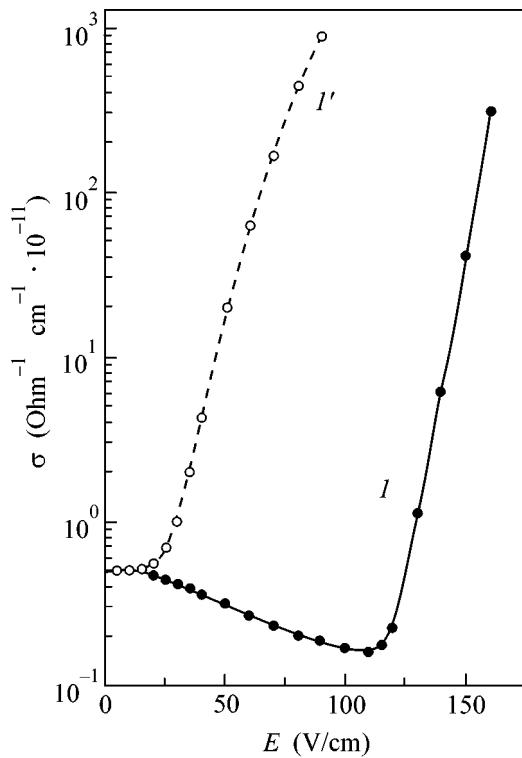**Fig. 1.** Curves $\sigma(E)$ for sample 1 with $= 3.5 \times 10^{16}$ cm^{-3} and $K \sim 3 \times 10^{-5}$ at $T = 8$ K after annealing (*1*) at $t = 1000°$C and (*1'*) at $t = 700°$C.

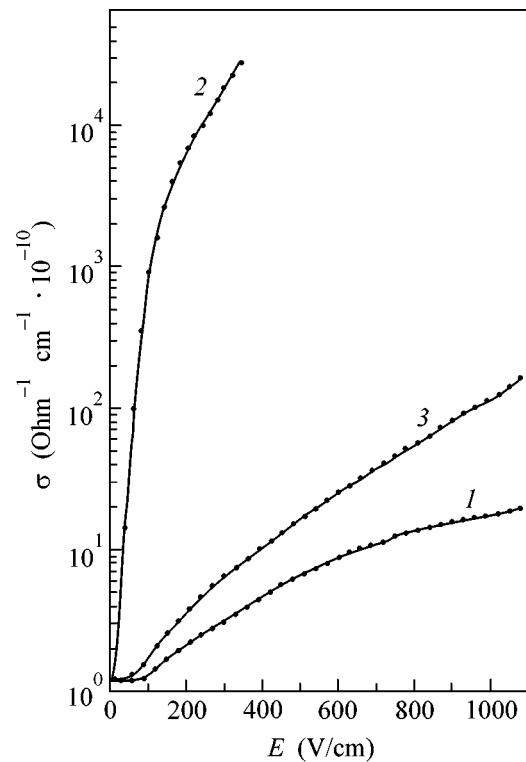**Fig. 2.** Curves $\sigma(E)$ for sample 2 with $N = 5.2 \times 10^{16}$ cm^{-3} and $K \sim 2.5 \times 10^{-2}$ at $T = 4.2$ K: (*1*) reference sample, (*2*) and (*3*) deformed sample ($N_D \sim 10^7$ cm^{-2}); (*2*) **E** ∥ **D** and (*3*) **E** ⊥ **D**.

to room temperature. This annealing mode favored a decrease in E^* down to a value of ~ 20 V/cm (Fig. 1, curve *1'*). When the sample was repeatedly heated up to $t \sim 1000°$C and rapidly cooled down to room temperature, the $\sigma(E)$ dependence turned out to be close to curve *1* (Fig. 1). Subsequent heating up to $t = 700°$C and slow cooling down to room temperature led to a $\sigma(E)$ dependence close to curve *1'* (Fig. 1). The ohmic conductivity σ_3 remained unchanged.

For plastic deformation, we used Si : B single crystals grown by the CZM method with $N = 5.2 \times 10^{16}$ cm^{-3} and $K \sim 2.5 \times 10^{-2}$, in which σ_M was not observed. Chemically polished parallelepipeds $3.2 \times 3.5 \times 10$ mm^3 in size were deformed at $t = 800°$C by compression along the long edge, whose crystallographic direction deviated by $10°$ from the [1, –1, 0] plane by rotation around [110]. The density of dislocations was determined by etch pits on the (110) face. The chosen geometry provided plastic deformation at small applied stresses due to the glide of the screw and 60-degree dislocations in one (111) plane, so that the preferred direction (**D**) of 60-degree dislocations was perpendicular to the compression direction (**P**); that is **P** ⊥ **D**, **D** ∥ [110] (see Eq. [9]). Simultaneously, an unstrained (reference) sample was subjected to heating up to $t = 800°$C. Next,

both samples were cooled for ~ 10 min down to room temperature.

In a reference sample, the $\sigma_3(T)$ dependence in the ohmic region and the form of the $\sigma(E)$ curve at 4.2 K (curve *1*, Fig. 2) coincide with those for the initial samples and characterize the standard σ_3 conductivity. In a deformed sample ($N_D \sim 10^7$ cm^{-2}), the $\sigma(E)$ curve was measured for two orientations of the electric field **E** with respect to the preferred direction of 60-degree dislocations **D**: **E** ⊥ **D** (along the compression axis, **E** ∥ **P**) and **E** ∥ **D** (perpendicular to the compression axis, **E** ⊥ **P**). In the case of **E** ∥ **D**, the form of the $\sigma(E)$ dependence in this sample (Fig. 2, curve *2*) changed radically as compared with that in the reference sample. In the case of **E** ⊥ **D**, the change was significantly smaller (curve *3*). In the case of **E** ∥ **D**, the growth of σ with increasing E started at $E^* \sim 15$ V/cm. It is evident that the difference in the values of σ for **E** ⊥ **D** and **E** ∥ **D** at $E = 300$ V/cm comprises ~10^4. Thus, there is strong anisotropy of the nonohmic conductivity along and across dislocations.

At a different geometry of the deformed sample when dislocations moved over three intersecting glide planes and there was no preferred direction of dislocations, the nonohmic conductivity was also observed for the **E** ∥ **P** orientation (Fig. 3, curve *1*, $N_D \sim 2 \times 10^7$ cm^{-2}).

Annealing at $t = 700°C$ and the subsequent slow cooling do not affect the value of E^*. Differences arise at higher values of E (curve *2*). In this case, the dependences of σ on E and H are qualitatively similar to those observed previously in unstrained, weakly compensated samples of Si [3].

Let us discuss the results obtained. Because the reference and the deformed samples in Figs. 2 and 3 differ only in the density of dislocations, such factors as the effects of the surface, contacts, thermal donors, oxygen precipitates, etc. can be excluded from consideration (in spite of the fact that this conclusion seems to be well substantiated, special experiments were performed to confirm that the surface and contacts are not important here). The emergence of nonohmic conductivity σ_M with increasing density of dislocations in a sample in which σ_M was not observed at all (Fig. 3) and the anisotropy of σ_M (Fig. 2) confirm the hypothesis that σ_M is effected along dislocations. Note that the static conductivity via dislocation cores in Si does not occur even at $N_D \sim 10^9$–10^{10} cm^{-2} [10]. It may be suggested that σ_M is due to conductivity via impurities located in the vicinity of dislocations.

The effect of dislocations on the impurity conductivity was observed previously [11]. Samples of *n*-germanium with the antimony concentration $N = 2.5 \times 10^{16}$ cm^{-3} (which is close to the Mott transition for germanium) and compensation $K < 0.5$ were studied. Using plastic deformations, dislocations were introduced in samples with density $N_D \leq 10^{10}$ cm^{-2}. The main result of this work is a decrease in the σ_3 conductivity with increasing N_D. The authors explain this by the "drawing" of impurities together toward dislocations and the formation of impurity "Cottrell atmospheres" [12] during high-temperature treatment in the case of plastic deformation. This phenomenon, which is known rather well, is the reason for the "rarefaction" (decrease in concentration) of impurities in the bulk, that is, an increase in the mean distance between impurities, which results in a decrease in σ_3. This "drawing" is caused by the effective attraction of Sb atoms to the dislocation core arising from a difference in the covalent radii of Sb and Ge. The same must take place for B atoms in Si at the corresponding temperatures and annealing durations. It is evident that, generally speaking, a high-temperature hold followed by rapid cooling (the first annealing mode) creates an excessive impurity concentration in the vicinity of dislocations as compared to the bulk. The higher the annealing temperature, the smaller is this concentration. This concentration is higher in the case of heating to $t = 700°C$ and slow cooling (the second mode). We associate the difference between the solid (the first mode) and the dashed (the second mode) curves in Fig. 1 with this fact. One form of the $\sigma(E)$ dependence can be changed to another and back by alternating annealing modes. This was performed for sample 1 in Fig. 1. The smaller
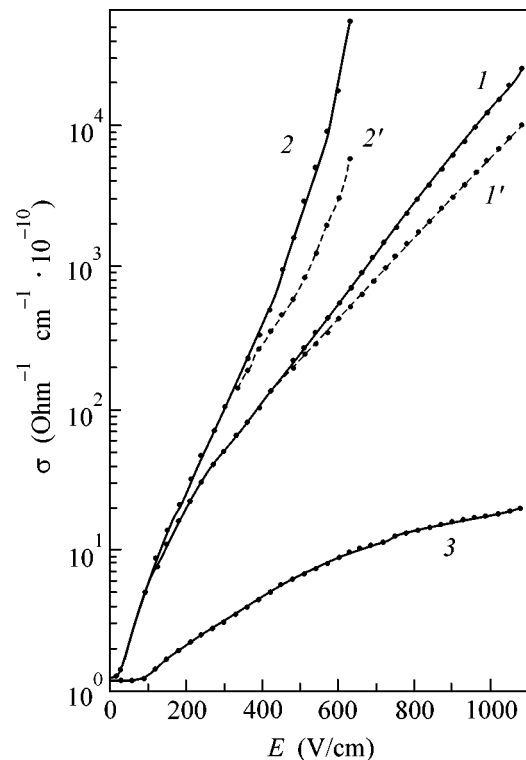

Fig. 3. Curves $\sigma(E)$ for (*1*) deformed sample 2 with disoriented dislocations ($N_D \sim 2 \times 10^7$ cm^{-2}), (*2*) deformed sample after long annealing at $t = 700°C$, and (*3*) reference sample; (*1'*) and (*2'*) curves $\sigma(E)$ at $H = 3$ T.

difference between curves in Fig. 2 can be associated with the small difference between the deformation and annealing temperatures (800 and 700°C). The annealing mode does not affect the initial sections of curves in Fig. 1 (σ_3 conductivity), because no significant rarefaction of impurities occurs in the bulk at a low density of dislocations ($N_D \approx 10^4$ cm^{-2}). The same is true for the deformed samples in Figs. 2 and 3.

Within the framework of the hypothesis under discussion, the conclusion can be made that the existence of σ_M conductivity in samples with low K is due to an increased boron concentration in the vicinity of dislocations.

Let us outline our considerations as to how this gives rise to the new conduction mechanism. An elastic deformation field exists in the vicinity of a dislocation. When an impurity atom is brought into this region, it experiences "hydrostatic" compression or tension [12]. From general considerations, it should be expected that the energy levels of the ground (ε_0) and the H^--like (ε^-) states must be displaced. The displacement magnitude depends on R (R is the distance to the dislocation core).

The properties of σ_M can be explained if one assumes that the ε_0 and ε^- levels in Si : B are displaced down in the vicinity of dislocations. In this case, the ε_0

levels of centers close to dislocations go under the Fermi level and become inactive, and the $\varepsilon^-(R)$ levels form a stairway of states in the vicinity of dislocations (the tail of the upper Hubbard band (UHB)) because $\varepsilon^-(R)$ increases with R. Jumping up the steps of this stair, electrons in the field E go up in energy (simultaneously moving away from dislocations) and attain the percolation level (transport level ε_{tr}). A large positive magnetoresistance points to a large localization radius of states at the transport level ε_{tr}. This level, as indicated at the beginning, is located at a distance of 10–15 meV from the empty band bottom. Therefore, centers that form this level must be located sufficiently close to dislocations. Thus, the origin of the UHB tail states, the deep location of the ε_{tr} level, and the mechanism of its filling are explained.

The motion of an electron over the tail states (slow at the initial stage) is interrupted by a recombination with a vacancy. The recombination intensity must increase with σ_3. This immediately explains the fact that σ_M decreases with increasing N and K and that the range of σ_M observation is narrow with respect to N and K (in Si : B, $N < 6 \times 10^{16}$ cm^{-3} and $K < 10^{-3}$ at $N_D < 10^{-4}$ cm^{-2} and $E = 100$ V/cm). The introduction of dislocations and an increase in E extend this range. From the aforesaid it is clear why σ_M conductivity was not observed in [11]: studies were carried out with samples characterized by an excessively high value of σ_3 (~10^{-3} Ω^{-1} cm^{-1}) at small values of E (in the ohmic region).

Within the framework of the hypothesis under discussion, the value of σ_M in samples in which dislocations have a preferred orientation must strongly depend on the angle between the directions of dislocations and the electric field. In our opinion, the anisotropy of conductivity observed experimentally and other results presented here give convincing evidence that the nonohmic σ_M conductivity is effected via impurities localized in the vicinity of dislocations.

REFERENCES

1. H. Fritzshe, Phys. Rev. **99**, 406 (1955).
2. E. M. Gershenzon, Yu. A. Gurvich, A. P. Mel'nikov, and L. N. Shestakov, Pis'ma Zh. Éksp. Teor. Fiz. **52**, 204 (1990) [JETP Lett. **51**, 231 (1990)].
3. A. P. Mel'nikov, Yu. A. Gurvich, L. N. Shestakov, and E. M. Gershenzon, Pis'ma Zh. Éksp. Teor. Fiz. **73**, 50 (2001) [JETP Lett. **73**, 44 (2001)].
4. A. P. Mel'nikov, Yu. A. Gurvich, L. N. Shestakov, and E. M. Gershenzon, Pis'ma Zh. Éksp. Teor. Fiz. **66**, 232 (1997) [JETP Lett. **66**, 249 (1997)].
5. A. P. Mel'nikov, Yu. A. Gurvich, L. N. Shestakov, and E. M. Gershenzon, Pis'ma Zh. Éksp. Teor. Fiz. **65**, 56 (1997) [JETP Lett. **65**, 59 (1997)].
6. A. P. Mel'nikov, Yu. A. Gurvich, L. N. Shestakov, and E. M. Gershenzon, Pis'ma Zh. Éksp. Teor. Fiz. **69**, 70 (1999) [JETP Lett. **69**, 77 (1999)].
7. Yu. A. Gurvich, A. P. Mel'nikov, L. N. Shestakov, and E. M. Gershenzon, Pis'ma Zh. Éksp. Teor. Fiz. **60**, 845 (1994) [JETP Lett. **60**, 859 (1994)].
8. B. I. Shklovskiǐ and A. L. Efros, *Electronic Properties of Doped Semiconductors* (Nauka, Moscow, 1979; Springer-Verlag, New York, 1984).
9. Yu. A. Osip'yan, V. M. Prokopenko, V. I. Tal'yanskiǐ, *et al.*, Pis'ma Zh. Éksp. Teor. Fiz. **30**, 123 (1979) [JETP Lett. **30**, 111 (1979)].
10. S. A. Shevchenko, Yu. A. Ossipyan, T. R. Mchedlidze, *et al.*, Phys. Status Solidi A **146**, 745 (1994).
11. I. V. Klyatskina, M. L. Kozhukh, S. M. Ryvkin, *et al.*, Pis'ma Zh. Éksp. Teor. Fiz. **29**, 268 (1979) [JETP Lett. **29**, 239 (1979)].
12. A. H. Cottrell, *Dislocations and Plastic Flow in Crystals* (Clarendon, Oxford, 1953; Metallurgizdat, Moscow, 1958).

Translated by A. Bagatur'yants

Influence of Magnetic Field on the Interlayer Interaction in (Co/Si/Gd/Si)$_n$ Films

G. S. Patrin[1]*, V. O. Vas'kovskiĭ[2], D. A. Velikanov[3], and A. V. Svalov[2]

[1]*Krasnoyarsk State University, Krasnoyarsk, 660041 Russia*
* *e-mail: pat@iph.krasnoyarsk.su*
[2]*Ural State University, pr. Lenina 51, Yekaterinburg, 620083 Russia*
[3]*Kirenskiĭ Institute of Physics, Siberian Division, Russian Academy of Sciences,*
Akademgorodok, Krasnoyarsk, 660036 Russia
Received December 26, 2001

A singularity sensitive to the external magnetic field was observed in the temperature dependences of the magnetization of multilayer (Co/Si/Gd/Si)$_{20}$ films in the vicinity of compensation temperature. Possible mechanisms responsible for the unusual behavior of the magnetization are discussed. © *2002 MAIK "Nauka/Interperiodica".*

PACS numbers: 73.40.Sx; 75.70.Cn; 75.60.Ej

Among the class of multilayer magnetic films, the structures with a semiconducting interlayer are of considerable interest, because the magnetic state of such systems can be controlled either by changing the concentration of charge carriers in the semiconductor or by varying temperature, introducing dopants, or through optical illumination. Until recently, considerable attention in studying films of this type was focused on the systems containing magnetic iron layers and nonmagnetic layers of silicon or its alloys with other elements. The main effect distinguishing these films from the films with a metallic interlayer consists in the temperature dependence of the interlayer exchange, which can manifest itself both as the temperature-induced enhancement of the interlayer exchange interaction [1, 2] and as a change in the exchange sign with temperature, e.g., in the systems with an α-ZnSe semiconductor as an interlayer material [3]. The effect of photoinduced change in the magnetic state observed for the Fe/Si/Fe films is also noteworthy [4, 5].

One can expect that the inclusion of a layer of a rare-earth metal into the layered structure containing a 3*d*-metal layer will extend the diversity of observed effects on account of the competing interactions. For example, depending on the film preparation technology and spatial period of the structure, a compensation point (T_c) typical of the homogeneous (not layered) 4*f*–3*d* alloys [7] may appear in the magnetization versus temperature curve of a Gd/Co system [6]. However, a magnetization compensation point was also observed in the case where the Co and Gd layers were separated by a small silicon interlayer [8]. It is clear that, in the temperature range where the competing interactions almost completely compensate the contributions from different magnetic layers, the properties of the whole system can be influenced even by weak external action.

In this work, the influence of a magnetic field on the interlayer exchange interaction was observed in the (Co/Si/Gd/Si)$_n$ films.

Films were prepared by the ion rf sputtering technique [6]. Glass was used as the substrate material. Samples were sequences of twenty (Co/Si/Gd/Si) blocks protected at the bottom and the top by silicon layers with a thickness of $t_{Si} = 200$ Å. The thicknesses of each of the cobalt and gadolinium layers were $t_{Co} = 30$ Å and $t_{Gd} = 75$ Å, respectively, and the thickness of the silicon interlayer was varied in the range $t_{Si} = 0$–10 Å. All thickness parameters were specified by the sputtering time and the known deposition rate of the corresponding material. The layered character of the films and the nominal values of the spatial period of the structure were confirmed (to within ±2 Å) by the small-angle X-ray scattering technique. In addition, X-ray and electron microscopy studies of the films showed that they were close to amorphous structures. Magnetization measurements were made on a SQUID magnetometer described in [9]. When performing temperature and field measurements, the sample was placed in a demagnetizer prior to zero-field cooling. The magnetic field was parallel to the sample plane.

Earlier [6], it was shown that the compensation temperature in the Gd/Co films with the layer thickness ratio close to that in the samples studied in this work strongly depends on the period of the multilayer structure, and at temperatures $T < 200$ K the compensation is observed only if $t_{Gd} + t_{Co} \geq 130$ Å. In our case, this feature is absent for the structure with a period of 105 Å (Fig. 1a). However, the compensation point appears
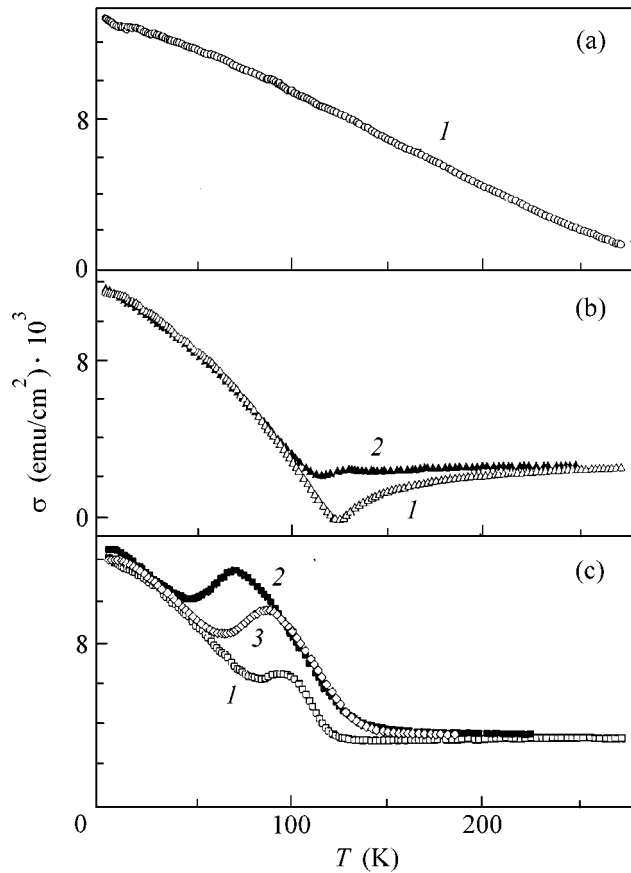
Fig. 1. Temperature-dependent magnetizations of the multilayer $(Gd/Si/Co/Si)_{20}$ films: t_{Si} = (a) 0, (b) 5, and (c) 10 Å. The curves are recorded in the fields H = (*1*) 200, (*2*) 1000, and (*3*) 500 Oe. In all films, t_{Co} = 35 Å and t_{Gd} = 70 Å.

Fig. 2. Field-dependent magnetizations of the multilayer $(Gd/Si/Co/Si)_{20}$ films: t_{Si} = (a) 0, (b) 5, and (c) 10 Å; T = 4.2 K. Arrows indicate the direction of changing magnetic field.

after the inclusion of a silicon interlayer a few angstroms in thickness (Fig. 1b, curve *1*). Unexpectedly, the behavior of the magnetization in the vicinity of the compensation temperature shows a material dependence on the magnetic field even when its value is rather low. For instance, the compensation temperature, in its traditional meaning, is absent at H = 1 kOe in the film with t_{Si} = 5 Å, and the temperature dependence of magnetization takes the form shown by curve *2* in Fig. 1b. It should be noted that a small maximum appears in the temperature curve, while the magnetization minimum shifts to lower temperatures. The situation proved to be even more unusual for the film with t_{Si} = 10 Å (Fig. 1c). In this film, the magnetization minimum (not zero), which could be related to the compensation point, was observed up to the fields on the order of 100 Oe. One can see that the maximum in the magnetization versus temperature curve increases with the magnetic field and shifts to low temperatures.

We recorded field dependences of the magnetization at helium temperatures. It is seen in Fig. 2 that the magnetization curves for the films with t_{Si} = 0 Å and t_{Si} = 5 Å are similar to those in ferromagnets with saturation
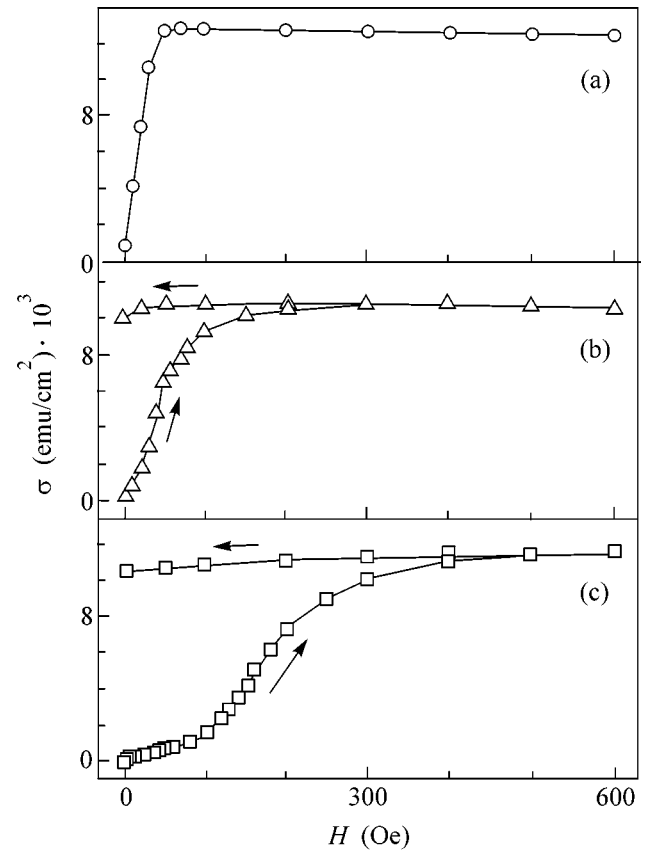
fields $H_s \approx 100$ Oe and $H_s \approx 300$ Oe, respectively. As for the film with t_{Si} = 10 Å, there is a knee on the magnetization curve in the vicinity of $H \cong 100$ Oe, while the saturation field is $H_s \approx 500$ Oe. The reverse run of the magnetization curve of this film only slightly deviates from the straight line. When comparing these results with the temperature behavior of magnetization, one can see that the field-induced magnetization singularity in the region of compensation temperature is most pronounced in the fields higher than the saturation field, i.e., in the region where no singularities are expected. One can see from Figs. 1 and 2 that the saturation magnetizations at low temperatures coincide with good accuracy for the films with a silicon interlayer and a Gd/Co film, indicating that the contribution from the rare-earth subsystem below the singularity temperature is the same in both cases and dominant in this region. For temperatures T > 120 K, where the contribution from the cobalt subsystem dominates, the magnetizations for the films with t_{Si} = 5 Å and t_{Si} = 10 Å also virtually coincide (Fig. 1).

These experimental results do not fit in the traditional scheme describing two-sublattice ferrimagnets

with a compensation point. The appearance of a maximum in the vicinity of the expected compensation temperature can be explained if one assumes, for example, that the interaction of the rare-earth layers with the neighboring cobalt layers through the silicon layer contains a contribution that gives rise, not to a strictly antiferromagnetic configuration, but to a canted magnetic structure. In such a situation, the magnetic structure as a whole represents a cone of magnetic moments of the rare-earth subsystem whose overall moment is antialligned with the overall magnetic moment of the cobalt layers. As the temperature rises, this interaction is first "switched off" on the background of a decreasing overall moment of the rare-earth subsystem and, as a result, the cone of the rare-earth subsystem collapses, whereupon the process evolves following the well-known scenario. Such a behavior of multilayer films is quite realistic. As known [10], the inclusion of a biquadratic exchange interaction (J_2) can give rise, in conjunction with the bilinear exchange (J_1), to a canted magnetic structure. In multilayer films, the mechanism responsible for the biquadratic contribution to the exchange interaction can be caused by the fluctuative variations in the nonmagnetic interlayer thickness [11]. The assumed distinction in the temperature dependences of both exchange parameters [12] is then also understood. Moreover, for the multilayer magnetic films, J_1 and J_2 can be comparable in magnitude.

In our case, the experimentally observed singularities can be naturally rationalized in terms of the interlayer interaction between the magnetic layers; however, the strong dependence of this interaction on a magnetic field still remains to be understood. Clearly, this effect cannot be ascribed to the magnetic crystallographic anisotropy of the materials forming magnetic layers. First, these layers are structurally amorphous, and, second, metallic Co and Gd possess strong local magnetic anisotropy [7], so that the magnetic fields used in this work are too low to rearrange their magnetic structures.

One can assume that the constant J_2 is due to the semiconducting interlayer and that J_2 is precisely the parameter which is sensitive to the magnetic field. This issue will be elucidated in a more comprehensive study.

REFERENCES

1. S. Toscano, B. Briner, H. Hopster, and M. Landolt, J. Magn. Magn. Mater. **117**, L301 (1992).
2. E. E. Fullerton and S. D. Bader, Phys. Rev. B **53**, 5112 (1996).
3. P. Walser, M. Hunziker, T. Speck, and M. Landolt, Phys. Rev. B **60**, 4082 (1999).
4. J. E. Mattson, E. E. Fulerton, S. Kumar, *et al.*, J. Appl. Phys. **75**, 6169 (1994).
5. G. S. Patrin, N. V. Volkov, and V. P. Kononov, Pis'ma Zh. Éksp. Teor. Fiz. **103**, 287 (1998) [JETP Lett. **68**, 307 (1998)].
6. V. O. Vas'kovskiǐ, D. Garsias, A. V. Svalov, *et al.*, Fiz. Met. Metalloved. **86**, 48 (1988).
7. K. N. R. Taylor and M. I. Darby, *Physics of Rare Earth Solids* (Chapman and Hall, London, 1972).
8. D. N. Merenkov, A. B. Chizhik, S. L. Gnatchenko, *et al.*, Fiz. Nizk. Temp. **27**, 188 (2001) [Low Temp. Phys. **27**, 137 (2001)].
9. G. S. Patrin, D. A. Velikanov, and G. A. Petrakovskiǐ, Zh. Éksp. Teor. Fiz. **103**, 234 (1993) [JETP **76**, 128 (1993)].
10. É. L. Nagaev, *Magnets with Compound Exchange Interactions* (Nauka, Moscow, 1988).
11. J. S. Slonczewski, Phys. Rev. Lett. **67**, 3172 (1991).
12. Jun-Zhong Wang, Bo-Zang Li, and Zhan-Ning Hu, Phys. Rev. B **62**, 6570 (2000).

Translated by V. Sakun

Two-Dimensional Site–Bond Percolation as an Example of a Self-Averaging System[1]

O. A. Vasilyev

Landau Institute for Theoretical Physics, Russian Academy of Sciences, ul. Kosygina 2, Moscow, 117940 Russia
e-mail: vasilyev@itp.ac.ru
Received December 27, 2001

The Harris–Aharony criterion for a static model predicts that if a specific heat exponent $\alpha > 0$, then this model does not exhibit self-averaging. In the two-dimensional percolation model, the index $\alpha = -\frac{1}{2}$. This means that, in accordance with the Harris–Aharony criterion, the model can exhibit self-averaging properties. We study numerically the relative variances R_M and R_χ for the probability M of a site belonging to the "infinite" (maximum) cluster and for the mean finite-cluster size χ. It was shown that two-dimensional site–bond percolation on the square lattice, where the bonds play the role of the impurity and the sites play the role of the statistical ensemble over which the averaging is performed, exhibits self-averaging properties. © *2002 MAIK "Nauka/Interperiodica".*

PACS numbers: 64.60.Ak; 64.60.Cn

1. INTRODUCTION

The influence of disorder on a phase transition is one of the important problems in the theory of phase transitions. In experimental measurements, the thermodynamic properties of one (or several) large-sized sample (with respect to the number of molecules) are usually studied. Therefore, it is important to know whether a single large-sized sample with quenched realization of impurities can represent the properties of a model. The self-averaging properties of the system provide an answer to this question. If some quantity is self-averaging, the measurement for a single large sample gives a reasonable value for all samples of such size. If the quantity is not self-averaging, an increase in the system size does not make the measurement on a single sample representative.

Let us consider some statistical model with impurities on the d-dimensional lattice with a linear size L, in which we average some quantity $X(\omega)$ for a certain sample, where ω is the impurity realization from some impurity ensemble Ω. Here we assume that $X(\omega)$ is the exact thermal average for impurity realization ω. Let us denote by $[X]$ the average over all impurity realizations of ensemble Ω: $[X] = \sum_{\omega \in \Omega} P(\omega) X(\omega)$, where $P(\omega)$ is the probability of impurity realization ω. Then, variance $V_X = \sum_{\omega \in \Omega} P(\omega) X^2(\omega) - [X]^2$. Let us define the relative variance of X: $R_X = V(x)/[X]^2$. This quantity characterizes the size-dependent properties of the model. If

---

[1] This article was submitted by the author in English.

$R_X(L) \sim L^x$, $x = -d$, the quantity X is said to be strongly self-averaging. If $x < 0$, X is said to be weakly self-averaging, and if $\lim_{L \to \infty} R_X(L) \longrightarrow$ const, then X is non-self-averaging. We will now discuss self-averaging of a disordered system; therefore, we examine the averaging over all impurity realizations, instead of self-averaging of a pure system, when we study the averaging over the whole statistical ensemble (for example, over all possible spin configuration for spin models).

The Harris criterion states [1] that the weak randomness does not change the critical behavior of the d-dimensional second-order phase-transition model if the specific heat index $\alpha < 0$, which corresponds to the pure correlation-length index $\nu > 2/d$. As was first mentioned by Brout [2], far for critiality, where the system size is much greater than the correlation length $L \gg \xi$, all additive thermodynamic quantities are strongly self-averaging. The self-averaging properties of a disordered system near the criticality obeys the Harris–Aharony (HA) criterion (see [3] and [4]). This criterion states that, if randomness is irrelevant, the system is governed by a pure fixed point and the relative variance $R_X \sim L^{\frac{\alpha_p}{\nu_p}}$, where α_p and ν_p are the critical exponents of a pure system. If however, the system is governed by a random fixed point, then $\lim_{L \to \infty} R_X =$ const. This criterion explains the numerical results of many works [5–7]. Wiseman and Domany in [7] show that the Ashkin–Teller model with $\alpha < 0$ is weakly self-averaging.

Two-dimensional percolation, which can be treated as a q-state Potts model with $q \longrightarrow 1$, is one of the most

popular two-dimensional statistical models with the second-order phase transition. The two-dimensional percolation critical index $\alpha = -\frac{1}{2} < 0$, and, in accordance with the HA criterion, we can expect that this model exhibits weak self-averaging properties. We study numerically the relative variances R_M and R_χ for the probability M of a site belonging to the maximum cluster size (the analog of magnetization) and the mean finite-cluster size χ (the analog of the magnetic susceptibility). It was shown that two-dimensional site-bond percolation, where bonds play the role of impurities and sites play the role of statistical ensemble over which the averaging is performed, exhibits self-averaging properties. The article is arranged as follows. In section 2, we describe the site–bond percolation model and two types of impurity distribution; in section 3; we discuss the self-averaging criterion and its phenomenological derivation; in section 4, we present the numerical results; and section 5 is the conclusion.

2. TWO-DIMENSIONAL SITE–BOND PERCOLATION MODEL AND CANONICAL AND GRAND-CANONICAL IMPURITY DISTRIBUTIONS

Site–bond percolation is a combination of purely site percolation and purely bond percolation. In purely site percolation, one investigates clusters of occupied sites. In purely bond percolation, one investigates clusters of sites connected by occupied bonds. In the site–bond percolation, one investigates clusters of occupied sites connected by occupied bonds. Each site is occupied with probability p_s, and each bond is occupied with probability p_b. In critical point (p_s^*, p_b^*), the correlation length becomes infinite. Yanuka and Engelman [8] proposed an approximate formula for a critical curve in the (p_s, p_b) plane:

$$\log(p_s)/\log(p_s^*) + \log(p_b)/\log(p_b^*) = 1.$$

The two-dimensional site–bond percolation belongs to the same universality class as the two-dimensional purely site percolation. Let us define by n_C the mean number of clusters of size C per lattice site. Then, the probability of a site belonging to the maximum cluster is

$$M = n_{C_{max}} C_{max} \qquad (1)$$

and the mean finite cluster size is

$$\chi = \sum_{C,\, C \neq C_{max}} n_C C^2 / \sum_{C,\, C \neq C_{max}} n_C C. \qquad (2)$$

Near the critical point (p_s^*, p_b^*), these quantities scale as

$$M(p_s, p_b = p_b^*) \sim (p_s - p_s^*)^{+\beta},$$
$$p_s > p_s^*, \quad \beta = 1/18 \qquad (3)$$

and

$$\chi(p_s, p_b = p_b^*) \sim (p_s - p_s^*)^{-\gamma}, \quad \gamma = 43/18. \qquad (4)$$

The scaling index $\xi(p_s, p_b = p_b^*) \sim (p_s - p_s^*)^{-\nu}$ for the correlation length is $\nu = \frac{4}{3}$.

As mentioned above, each bond is occupied with probability p_b and is empty with probability $1 - p_b$; therefore, the total number of occupied bonds on the lattice fluctuates. This method of generating impurity configurations is known as Grand Canonical (GC), by analogy with the Grand Canonical statistical ensemble with a fluctuating number of particles. However, we can fix the number of occupied bonds N_b and then distribute them randomly on the lattice. This method of generating impurity configurations is known as Canonical (C), by analogy with the Canonical statistical ensemble with a fixed number of particles.

3. SELF-AVERAGING CRITERION

Let us explain the HA criterion using simple phenomenological considerations [6]. In this section, we use the temperature T as a parameter of the model, keeping in mind that, in the case of percolation, the role of this parameter is played by the site concentration p_s.

We characterize every sample (impurity realization) ω with a size L by a pseudo-critical temperature $T^*(\omega, L)$. $T^*(\omega, L)$ fluctuates about its mean value and is averaged over all impurity configurations $T^* = [T^*(\omega, L)]$. We introduce the reduced temperature for each sample

$$i_\omega = \frac{T - T^*(\omega, L)}{T^*}. \qquad (5)$$

In the vicinity of the critical point, the quantity X scales as

$$X_\omega(T, L) = L^\rho \tilde{Q}_\omega(i_\omega L^{y_t}). \qquad (6)$$

Here, ρ is the exponent characterizing the behavior of $[X]$ at T^* and the thermal scaling index $y_t = 1/\nu$ is assumed to be universal for all samples. The form of function $\tilde{Q}_\omega$ is assumed to be sample-dependent. We assume that (this relation is numerically checked in the next section)

$$(\delta T^*)^2 \sim (\delta i_\omega)^2 \sim L^{-d}. \qquad (7)$$

Therefore, the variance of the argument of the function $\tilde{Q}_\omega$ scales as

$$(\delta i_\omega L^{y_t})^2 \sim L^{-d+2/\nu}. \qquad (8)$$

We keep in mind that the scaling relation [9] $\alpha = 2 - \nu d$. So, the variance V_x of quantity X at the critical point scales as

$$V_X \sim L^{2\rho}(\delta i_\omega L^{y_t})^2$$
$$\sim L^{2\rho-d+2/\nu} = L^{2\rho+(2-d\nu)/\nu} = L^{2\rho+\alpha/\nu}, \qquad (9)$$

and the relative variance ($[X] \sim L^\rho$) is

$$R_X = \frac{V_X}{[X]^2} = L^{2\rho+\frac{\alpha}{\nu}-2\rho} = L^{\alpha/\nu}. \qquad (10)$$

We thus obtain the Harris–Aharony criterion: *if the scaling index is $\alpha = const < 0$, then the model is self-averaging and the relative variance for quantity X is $R_X \sim L^{\alpha/\nu}$ from simple scaling relations.*

4. NUMERICAL RESULTS

In our computation, the bonds play the role of impurities; therefore, we fix the bond concentration $p_b^* = 0.875$ and consider the site concentration p_s as the parameter of our model.

(1) We generate (by the C and GC methods) the bond configuration ω;

(2) for this bond configuration we generate a set of site configurations (for site we use only the GC method). For each site configuration, we calculate the probability of a site belonging to the maximum cluster and the mean finite cluster size;

(3) we average these quantities over the site realizations and obtain mean values $M(p_s, p_b)$ and $\chi(p_s, p_b)$. We split the set of site configurations into ten series to evaluate the numerical inaccuracy ΔM and $\Delta \chi$;

(4) we perform steps 1–3 for another bond configuration.

The $\chi_\omega(p_s)$ dependence for three different bond realizations ($\omega = 1, 2, 3$) is shown in Fig. 1. Let us calculate the pseudocritical site concentration $p_s^*(\omega)$ for each bond realization ω. We assume that the mean finite-cluster size $\chi_\omega(p_s)$ has a maximum at the pseudocritical point $p_s^*(\omega)$ and, therefore, So we approximate the data for χ_ω near the maximum of χ_ω by the parabola $\chi_\omega(p_s) \simeq a - b(p_s - p_s^*(\omega))^2$ and treat $p_s^*(\omega)$ as the pseudocritical concentration for bond realization ω. The locations of the pseudocritical points for bond realizations $\omega = 1, 2, 3$ is shown in Fig. 1 by vertical lines.

Let us find the critical point p_s^*. We calculate the mean critical site concentration $[p_s^*(L)]$ averaged over 100 bond realizations created by the GC and C methods as a function of lattice size L. These numerical data and the results of approximation

$$\text{C-method: } [p_s^*(L)]_C \qquad (11)$$
$$\simeq 0.6519(5) - 0.34(10)L^{-0.94(9)},$$

$$\text{GC-method: } [p_s^*(L)]_{GC} \qquad (12)$$
$$\simeq 0.6511(4) - 0.39(15)L^{-1.02(11)}$$

are shown in Fig. 2. We take the concentration $p_s^* = 0.6515$ (averaged by the C and GC methods) as critical. The variance of pseudocritical concentration behaves
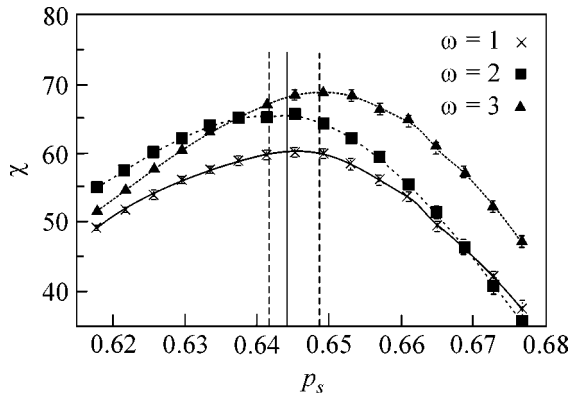

Fig. 1. The mean finite-cluster size $\chi(p)$ for three realizations of impurity configurations. The critical concentration $p_s^*(\omega)$ for each realization ω is shown by vertical lines.
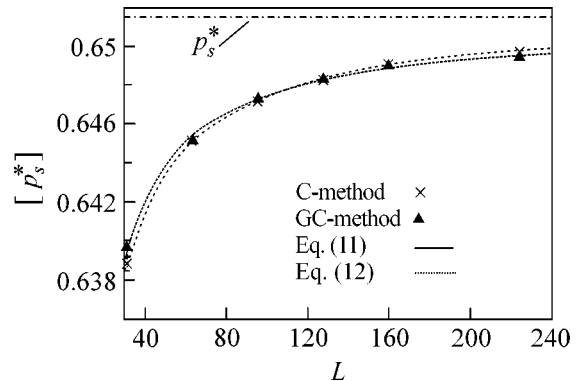

Fig. 2. The mean pseudocritical site concentration $[p_s^*]$ as a function of lattice size L for bond realizations created by the C and GC methods, the results of approximation by a power function of L, and the extrapolated critical concentration $p_s^* = 0.6515$.
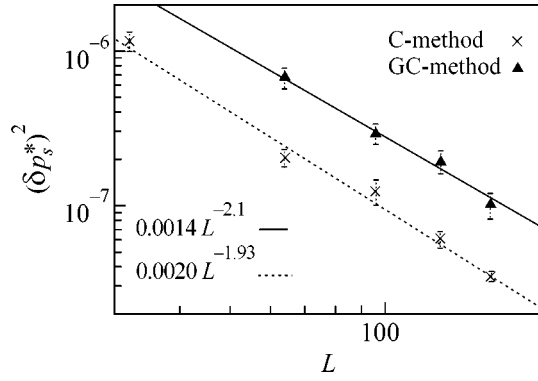
Fig. 3. The variance $(\delta p_s^*)^2$ of critical concentration as a function of lattice size L for microcanonical (crosses) and canonical (triangles) distributions and the results of approximation by function aL^{-b}.

as $(\delta p_s^*)^2 \sim L^{-2}$ (Fig. 3), as we assumed in the previous section.

Let us investigate the self-averaging properties of M and χ at the critical point ($p_b^* = 0.875$, $p_s^* = 0.6515$).

Now we describe the computational procedure that we used to calculate the relative variance. Here, we follow the method described in [5, 6]. First, we note that, for each impurity realization ω, instead of the exact value of quantity χ_ω we get some value $\overline{X}_\omega$ averaged over the site configuration with a numerical error

$$(\delta \overline{X}_\omega)^2 = \frac{\sigma_{p_b, \omega}}{N_s / \tau_\omega}. \qquad (13)$$

Here, N_s is the number of site configurations [the length of Monte-Carlo (MC) run] and τ_ω is the autocorrelation time. To calculate $(\delta \overline{X}_\omega)^2$, we split the MC sequence of

site configurations of length N_s into ten subsequences and treat each subsequence as independent. We define by [...] the averaging over impurity-bond configurations. Thus, the error of $[\overline{X}_\omega]$ averaged over N_b bond configurations is

$$(\delta [\overline{X}_\omega])^2 = \frac{1}{N_b - 1} \sum_{\omega \in \Omega} ([\overline{X}_\omega^2] - [\overline{X}_\omega]^2). \qquad (14)$$

The total error $(\delta [\overline{X}_\omega])^2$ has two contributing terms: from the sample-to-sample fluctuation of exact X_ω about $[X_\omega]$ and from the fluctuations of $\overline{X}_\omega$, averaged over the finite number of spin configurations, about X_ω for each bond realization ω:

$$(\delta [\overline{X}_\omega])^2 = \frac{V_X}{N_b} + \left[\frac{\sigma_{p_b, \omega}}{N_b N_s / \tau_\omega} \right]. \qquad (15)$$

Here, N_b is the number of bond configurations. We can calculate

$$\left[\frac{\sigma_{p_b, \omega}}{N_b N_s / \tau_\omega} \right] = \frac{1}{N_b} [(\delta \overline{X}_\omega)^2]$$

by averaging the error $(\delta \overline{X}_\omega)^2$ over the bond configurations ω. So, we can express the relative variance via $(\delta [\overline{X}_\omega])^2$ and $[(\delta \overline{X}_\omega)^2]$:

$$R_X = \frac{V_X}{[\overline{X}_\omega]^2} = \frac{1}{[\overline{X}_\omega]^2} (N_b (\delta [\overline{X}_\omega])^2 - [(\delta \overline{X}_\omega)^2]). \qquad (16)$$

The numerical data for relative variances R_M and R_χ computed by the C and GC methods in accordance with Eq. (16) are shown in Figs. 4 and 5, respectively. We can see that points lie on the straight lines in the log–log scale. Thus, we approximate the data by the power function aL^b on the interval $L \in [48, 128]$. The results
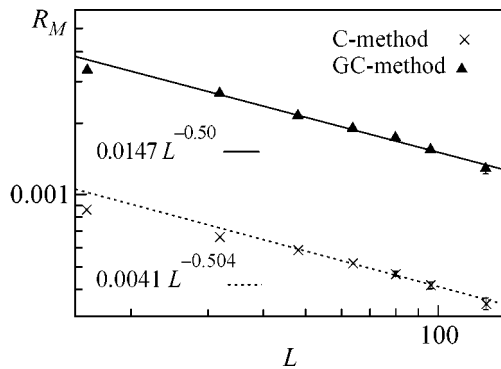

Fig. 4. The relative variance R_M of probability M of a site belonging to the maximum cluster as a function of lattice size L for GC (crosses) and C (triangles) distributions and the results of approximation by function aL^{-b}.
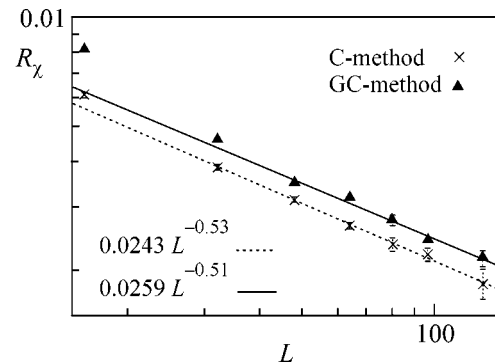

Fig. 5. The relative variance R_χ of the mean finite-cluster size χ as a function of lattice size LC (crosses) and GC (triangles) distributions and the results of approximation by function aL^{-b}.

of approximation are plotted in Figs. 5 and 4 and placed below. As we might expect, for the GC method the relative variance is greater than for the C method because of the fluctuation of the bond number:

$$C: R_M \simeq 0.0041(3)L^{-0.504(19)},$$

$$GC: R_M \simeq 0.0147(15)L^{-0.50(2)},$$

$$C: R_\chi \simeq 0.0243(2)L^{-0.53(2)},$$

$$GC: R_\chi \simeq 0.0259(5)L^{-0.51(5)}.$$

We see that, in excellent agreement with the HA criterion, the relative variance of measured quantities obeys the power-law dependence $R \sim L^{-1/2} = L^{\alpha/\nu}$. As a result, we can state that this model is self-averaging.

5. CONCLUSION

We have shown numerically that the two-dimensional site–bond percolation exhibits self-averaging. In our numerical experiments, bonds play the role of the quenched disorder and sites play the role of the statistical ensemble. We have found that relative variance scales as $R_M \sim L^{-1/2}$, $R_\chi \sim L^{1/2}$, where $-1/2 = \alpha/\nu$. We assume that we can consider the sites as a quenched dis-

order and bonds as a statistical ensemble and the results will be the same.

We can also expect for site percolation that, if we "freeze" the state of some sites and average over other sites, we get the same weakly self-averaging behavior with respect to these "frozen" sites, which play the role of a quenched disorder. Of course, the same is also valid for bond percolation.

REFERENCES

1. A. B. Harris, J. Phys. C **7**, 1671 (1974).
2. R. Brout, Phys. Rev. **115**, 824 (1959).
3. A. Aharony and A. Brooks Harris, Phys. Rev. Lett. **77**, 3700 (1996).
4. A. Aharony, A. Brooks Harris, and S. Wiseman, Phys. Rev. Lett. **81**, 252 (1998).
5. S. Wiseman and E. Domany, cond-mat/9506101.
6. S. Wiseman and E. Domany, cond-mat/9802102; Phys. Rev. E **58**, 2938 (1998).
7. S. Wiseman and E. Domany, cond-mat/9802095; Phys. Rev. Lett. **81**, 22 (1998).
8. M. Yanuka and R. Engelman, J. Phys. A **28**, L339 (1990).
9. R. B. Stinchcombe, in *Phase Transitions and Critical Phenomena*, Ed. by C. Domb and J. L. Lebovitz (Academic, New York, 1983), Vol. 7.